

AIRCRAFT DESIGN FOR REDUCED CLIMATE IMPACT

A DISSERTATION  
SUBMITTED TO THE DEPARTMENT OF AERONAUTICS AND  
ASTRONAUTICS  
AND THE COMMITTEE ON GRADUATE STUDIES  
OF STANFORD UNIVERSITY  
IN PARTIAL FULFILLMENT OF THE REQUIREMENTS  
FOR THE DEGREE OF  
DOCTOR OF PHILOSOPHY

Emily Schwartz Dallara  
February 2011

2011 by Emily Dallara. All Rights Reserved.  
Re-distributed by Stanford University under license with the author.

This dissertation is online at: <http://purl.stanford.edu/yf499mg3300>

I certify that I have read this dissertation and that, in my opinion, it is fully adequate in scope and quality as a dissertation for the degree of Doctor of Philosophy.

**Ilan Kroo, Primary Adviser**

I certify that I have read this dissertation and that, in my opinion, it is fully adequate in scope and quality as a dissertation for the degree of Doctor of Philosophy.

**Juan Alonso**

I certify that I have read this dissertation and that, in my opinion, it is fully adequate in scope and quality as a dissertation for the degree of Doctor of Philosophy.

**Mark Jacobson**

Approved for the Stanford University Committee on Graduate Studies.

**Patricia J. Gumpert, Vice Provost Graduate Education**

*This signature page was generated electronically upon submission of this dissertation in electronic format. An original signed hard copy of the signature page is on file in University Archives.*

# Abstract

Commercial aviation has grown rapidly over the past several decades. Aviation emissions have also grown, despite improvements in fuel efficiency. These emissions affect the radiative balance of the Earth system by changing concentrations of greenhouse gases and their precursors and by altering cloud properties. In 2005, aircraft operations produced about 5% of the worldwide anthropogenic forcing that causes climate change, and this fraction is projected to rise.<sup>[1]</sup> Changes in aircraft operations and design may be necessary to meet goals for limiting future climate change.

A framework is presented for assessing the comparative climate impacts of future aircraft during conceptual design studies. A linear climate model estimates the temperature change caused by emission species with varying lifetimes and accounts for the altitude-varying radiative forcings produced by NO<sub>x</sub> emissions and aviation induced cloudiness. The effects of design cruise altitude on aircraft fuel consumption and NO<sub>x</sub> emission rates are modeled simultaneously by integrating the climate model into an aircraft design and performance analysis tool. The average temperature response metric aggregates the lifetime climate change impacts from operating a fleet of particular aircraft. Lastly, uncertainty quantification studies are performed to determine the level of confidence in estimates of relative climate performance of competing aircraft configurations.

Aircraft climate change mitigation strategies are investigated with this framework. Without applying additional technologies, designing aircraft to fly at Mach 0.77 and 25,000-31,000 ft altitude enables 10-35% reductions in climate impacts (and 1% increases in operating costs) compared with more conventional designs that cruise at Mach 0.84, 39,000-40,000 ft altitude. This research also models the performance of

aircraft that adopt propfan engines, natural laminar flow, biofuels, low NO<sub>x</sub> combustors, and operational contrail avoidance. Aircraft flying below fuel-optimal altitudes incur a fuel burn penalty, but propfan and laminar flow technologies can offset these penalties and produce large fuel savings. These technologies enable collective climate impact reductions of 45-75% simultaneous with total operating cost savings relative to a conventional, baseline technology, minimum cost aircraft. Uncertainty quantification studies demonstrate that significant relative average temperature response savings can be expected with these strategies despite large scientific uncertainties. Design studies illustrate the importance of including non-CO<sub>2</sub> effects in an aircraft climate metric: if aircraft are designed to minimize CO<sub>2</sub> emissions, instead of the temperature change caused by all emissions, then potential savings are halved. Strategies for improving the climate performance of existing aircraft are also explored, revealing potential climate impact savings of 20-40%, traded for a 1-5% increase in total operating costs and reduced maximum range.

# Acknowledgments

This thesis would not have been possible without the guidance and support of many people. I owe my deepest gratitude to my adviser, Professor Ilan Kroo. He embraced and shared my passion for environmentally-friendly aircraft design and allowed me the freedom to drive the direction of my research. His insights and practical guidance over the last several years have helped developed my ability to tackle new challenges and will have a positive impact on me as I move forward in my career.

My sincere thanks go to members of my committee, Professors Juan Alonso and Mark Jacobson, for reading this thesis and providing thoughtful comments. Professor John Weyant contributed significantly, both by serving as a defense examiner and through useful discussions about climate change metrics. Additional thanks go to Professor Margot Gerritsen for serving as my defense committee chairperson. Our work in the area of climate metrics also greatly benefited from the feedback of MIT Professor Ian Waitz. Lastly, I would like to thank Steve Baughcum from the Boeing Company for many helpful conversations, particularly in the area of contrail avoidance strategies.

I feel very fortunate to have been a part of the Aircraft Design Group. Over the past several months, every member of the group has provided me with feedback and support that helped shape this research. I greatly value the experiences I have shared with our formation flight team: Geoff Bower, Jia Xu, Tristan Flanzer, and Andrew Ning. Many other friends on both sides of the Bay have made my years at Stanford among the most enjoyable in my life. Special thanks go to Noël Bakhtian for bringing the perfect amount of levity to our graduate school experiences in England and California.

Finally, I would not be in the position that I am today without the love and support of my entire family. Thanks to my Dad for always believing in me, especially when I didn't believe in myself. Thanks to my Mom for her tireless devotion and sacrifice in taking care of my brothers, sister, and me. Thanks to my husband, Chris, for giving my life balance and meaning (and for proofreading this entire document). This thesis is dedicated to him.

# Contents

|                        |  |          |
|------------------------|--|----------|
| <u>Abstract</u>        | iv                                       |          |
| <u>Acknowledgments</u> | vi                                       |          |
| <b>1</b>               | <b>Introduction</b>                      | <b>1</b> |
| 1.1                    | Global Climate Change . . . . .          | 1        |
| 1.2                    | Aviation and the Environment . . . . .   | 4        |
| 1.3                    | Contributions and Outline . . . . .      | 6        |
| <b>2</b>               | <b>Aircraft Climate Impacts</b>          | <b>7</b> |
| 2.1                    | Introduction . . . . .                   | 7        |
| 2.2                    | Aircraft Emissions and Climate . . . . . | 8        |
| 2.2.1                  | Carbon Dioxide . . . . .                 | 11       |
| 2.2.2                  | Water Vapor . . . . .                    | 12       |
| 2.2.3                  | Nitrogen Oxides . . . . .                | 12       |
| 2.2.4                  | Sulfur Oxides . . . . .                  | 13       |
| 2.2.5                  | Soot Particles . . . . .                 | 14       |
| 2.2.6                  | Aviation Induced Cloudiness . . . . .    | 14       |
| 2.3                    | Aircraft Emissions Regulations . . . . . | 16       |
| 2.4                    | Emissions Modeling . . . . .             | 16       |
| 2.4.1                  | Fuel-Proportional Emissions . . . . .    | 17       |
| 2.4.2                  | NO <sub>x</sub> P3-T3 Method . . . . .   | 17       |
| 2.4.3                  | Fuel Flow Correlation Methods . . . . .  | 18       |
| 2.5                    | Climate Impact Modeling . . . . .        | 18       |

|          |  |           |
|----------|--|-----------|
| 2.5.1    | Global Climate Models . . . . .                          | 19        |
| 2.5.2    | Integrated Assessment Models . . . . .                   | 19        |
| 2.5.3    | Linear Temperature Response Models . . . . .             | 20        |
| <b>3</b> | <b>Climate Change Metrics</b>                            | <b>21</b> |
| 3.1      | Introduction . . . . .                                   | 21        |
| 3.2      | Commonly Used Climate Metrics . . . . .                  | 23        |
| 3.2.1    | Mass of Emissions . . . . .                              | 23        |
| 3.2.2    | Radiative Forcing . . . . .                              | 23        |
| 3.2.3    | Global Warming Potential . . . . .                       | 23        |
| 3.2.4    | Global Temperature Potential . . . . .                   | 24        |
| 3.2.5    | Damages and Other Economic Metrics . . . . .             | 24        |
| 3.3      | Climate Metric for Comparative Aircraft Design . . . . . | 25        |
| 3.3.1    | Desired Metric Properties . . . . .                      | 25        |
| 3.3.2    | Average Temperature Response . . . . .                   | 28        |
| 3.3.3    | Alternative Aircraft Design Metrics . . . . .            | 34        |
| <b>4</b> | <b>Aircraft Design and Analysis Tools</b>                | <b>35</b> |
| 4.1      | Introduction . . . . .                                   | 35        |
| 4.2      | Program for Aircraft Synthesis Studies . . . . .         | 35        |
| 4.3      | Operating Costs . . . . .                                | 36        |
| 4.4      | Variable Bypass Ratio Engine Model . . . . .             | 37        |
| 4.4.1    | Engine Performance . . . . .                             | 41        |
| 4.4.2    | Engine Geometry . . . . .                                | 44        |
| 4.4.3    | Nacelle Parasite Drag . . . . .                          | 46        |
| 4.4.4    | Weight Estimation . . . . .                              | 49        |
| 4.4.5    | Certification Noise . . . . .                            | 52        |
| 4.4.6    | Engine Maintenance and Acquisition Costs . . . . .       | 54        |
| <b>5</b> | <b>Linear Climate Model with Altitude Variation</b>      | <b>55</b> |
| 5.1      | Introduction . . . . .                                   | 55        |
| 5.2      | Emissions . . . . .                                      | 56        |

|          |  |           |
|----------|--|-----------|
| 5.2.1    | Carbon Dioxide, Water Vapor, Soot, and Sulfate Emissions Indices . . . . . | 57        |
| 5.2.2    | Nitrogen Oxide Emissions Index . . . . .                                   | 57        |
| 5.3      | Radiative Forcing . . . . .  | 60        |
| 5.3.1    | Altitude Variation . . . . .   | 61        |
| 5.3.2    | Carbon Dioxide . . . . .   | 64        |
| 5.3.3    | Methane and Long-Lived Ozone . . . . .                                     | 64        |
| 5.3.4    | Short-Lived Species . . . . .  | 65        |
| 5.3.5    | Aviation Induced Cloudiness . . . . .                                      | 67        |
| 5.4      | Temperature Change . . . . .   | 67        |
| 5.5      | Limitations of the Climate Model . . . . .                                 | 69        |
| 5.6      | Uncertainty Quantification . . . . .                                       | 72        |
| 5.7      | Computing Average Temperature Response . . . . .                           | 74        |
| <b>6</b> | <b>Aircraft Design Studies</b>   | <b>78</b> |
| 6.1      | Introduction . . . . .   | 78        |
| 6.2      | Aircraft Optimization Problem . . . . .                                    | 79        |
| 6.3      | Results with Baseline Technology . . . . .                                 | 81        |
| 6.3.1    | Single-Objective Results . . . . .   | 81        |
| 6.3.2    | Cost-Climate Tradeoff . . . . .  | 84        |
| 6.4      | Results with Climate Mitigation Technologies . . . . .                     | 86        |
| 6.4.1    | CO <sub>2</sub> Impact Reduction . . . . .                                 | 86        |
| 6.4.2    | NO <sub>x</sub> Impact Reduction . . . . .                                 | 91        |
| 6.4.3    | AIC Impact Reduction . . . . .   | 97        |
| 6.4.4    | Comparison of Individual Technologies . . . . .                            | 100       |
| 6.4.5    | Combination of Technologies . . . . .                                      | 102       |
| 6.4.6    | Assessment of Climate Impact Uncertainty . . . . .                         | 104       |
| 6.5      | Alternative Metrics . . . . .  | 109       |
| 6.5.1    | Comparison to Results with CO <sub>2</sub> -Based Metric . . . . .         | 109       |
| 6.5.2    | Comparison to Results with Other Metrics . . . . .                         | 110       |
| 6.6      | Additional Studies . . . . .   | 112       |

|       |   |            |
|-------|---|------------|
| 6.6.1 | Effect of Varying Fuel Prices . . . . .               | 112        |
| 6.6.2 | Effect of Varying Mission Range . . . . .             | 113        |
| 6.7   | Mitigation Strategies for Existing Aircraft . . . . . | 114        |
| 7     | <b>Conclusions and Future Work</b>                    | <b>117</b> |
| 7.1   | Conclusions . . . . .                                 | 117        |
| 7.2   | Future Work . . . . .                                 | 119        |
| A     | <b>Turbofan and Propfan Performance Model</b>         | <b>122</b> |
|       | <b>Bibliography</b>                                   | <b>141</b> |

# List of Tables

|     |  |     |
|-----|--|-----|
| 2.1 | Annual emissions from global commercial aviation in 2006.[2] . . . . .   | 9   |
| 4.1 | Bypass ratio, fan pressure ratio, and diameter of engines with 25,000 pounds of sea level static thrust. . . . .   | 42  |
| 5.1 | Emissions indices.[3] . . . . .  | 57  |
| 5.2 | ICAO emissions certification simulated landing and takeoff cycle.[3] .   | 61  |
| 5.3 | CO <sub>2</sub> parameter values and distributions from §2.10.2 of the IPCC Fourth Assessment Report.[4] . . . . .   | 65  |
| 5.4 | Long-term NO <sub>x</sub> parameter values and distributions. . . . .  | 66  |
| 5.5 | H <sub>2</sub> O, O <sub>3</sub> s, SO <sub>4</sub> , soot, and AIC parameter values and distributions. . . . .  | 66  |
| 5.6 | Temperature change model parameter values and distributions. . . . .   | 70  |
| 5.7 | Values of unit ATRs for $H = 30$ years, $t_{max} = 500$ years, and four different values of $r$ calculated with a linear climate model. . . . .                        | 77  |
| 6.1 | List of optimization design variables and their bounds. . . . .  | 80  |
| 6.2 | List of optimization performance constraints. . . . .  | 80  |
| 6.3 | Description of aircraft designed for single-objective economic or environmental performance. . . . .   | 82  |
| 6.4 | Normalized baseline life cycle greenhouse gas emissions for various fuel pathways from Ref. [5]. Multiple values indicate varying land use change assumptions. . . . . | 92  |
| 6.5 | Description of aircraft designed for minimum total operating costs and ATR <sub>r=0</sub> with individual climate impact reduction technologies. . . . .               | 101 |

|  |            |
|--|------------|
| <u>6.6 Description of aircraft designed for minimum total operating costs and ATR<sub>r=0</sub> with multiple climate impact reduction technologies. . . . .</u> | <u>105</u> |
| <u>A.1 Engine design parameters. . . . .</u>   | <u>129</u> |
| <u>A.2 Fan configuration parameters. . . . .</u>   | <u>138</u> |
| <u>A.3 Propfan and turbofan engine parameters. . . . .</u>   | <u>140</u> |

# List of Figures

|     |   |    |
|-----|---|----|
| 1.1 | Observed global average surface temperature rise during the 20th century (black) and global climate model projections of future temperature rise for varying emissions scenarios (other colors), from Ref. [6]. . . . . | 2  |
| 1.2 | Historical and predicted aviation fuel use (top), and aviation and anthropogenic CO <sub>2</sub> emissions (bottom) (reprinted with permission from Elsevier).[1] . . . . .   | 3  |
| 1.3 | Pareto fronts of fuel carried, landing and takeoff NO <sub>x</sub> emissions, and cumulative certification noise, from Ref. [7]. . . . .  | 5  |
| 2.1 | Products of aircraft fuel combustion, adapted from Ref. [8]. . . . .  | 8  |
| 2.2 | Schematic diagram of relationship between aircraft emissions and climate impacts (reprinted with permission from Elsevier).[1] . . . . .  | 10 |
| 2.3 | Radiative forcing in the year 2005 due to all previous aircraft emissions (reprinted with permission from Elsevier).[1] . . . . .   | 11 |
| 3.1 | Cause and effect chain for aircraft climate change.[9] . . . . .  | 22 |
| 3.2 | Graphical representation of the steps for calculating ATR. In this example, $H = 30$ years, $r = 3\%$ , and $t_{\max} = 500$ years. . . . .   | 33 |
| 4.1 | Structure of PASS, adapted from Ref. [7]. . . . .   | 36 |
| 4.2 | Relationship between fan diameter, fan pressure ratio, and bypass ratio for a turbofan engine.[10] . . . . .  | 38 |
| 4.3 | Ideal propulsive efficiency versus fan pressure ratio.[11] . . . . .  | 39 |

|      |  |    |
|------|--|----|
| 4.4  | Effect of changing fan diameter on drag, weight, and propulsive efficiency, adapted from Ref. [10]. . . . .  | 39 |
| 4.5  | Comparison of fan sizes for turboprop, propfan, and turbofan engines (reproduced with permission of the American Institute of Aeronautics and Astronautics).[12] . . . . .   | 40 |
| 4.6  | Maximum available thrust versus Mach number at varying altitude for turbofans and dual and single rotor propfans of varying bypass ratio. . . . .  | 43 |
| 4.7  | Installed specific fuel consumption and overall efficiency versus throttle setting for turbofans and propfans of varying bypass ratio. . . . .   | 44 |
| 4.8  | Comparison of available thrust and specific fuel consumption for high bypass ratio engines, from model predictions and a NASA study.[13] .   | 45 |
| 4.9  | Engine length as a function of sea level static thrust. . . . .  | 47 |
| 4.10 | Nacelle form factor versus fineness ratio. . . . .   | 48 |
| 4.11 | Variation in turbofan weight with sea level static thrust and fan diameter. . . . .  | 50 |
| 4.12 | Turbofan and single and dual rotor propfan dry weight versus fan diameter for 25,000 sea level static thrust engines. . . . .  | 52 |
| 5.1  | Cruise and sea level static $\text{NO}_x$ emissions index for a sea level static overall pressure ratio 41 turbofan engine predicted by equation (5.4). . . . .  | 60 |
| 5.2  | Radiative forcing factor data for $\text{NO}_x$ impacts and aviation induced cloudiness, based on results from Refs. [14] and [15]. . . . .  | 63 |
| 5.3  | Scaled temperature impulse response functions from Hasselmann et al., Joos et al., Shine et al., and Boucher and Reddy.[16, 17, 18, 19] . . . . .  | 69 |
| 5.4  | Forcing factors (lines) with 66% likelihood ranges (shaded areas). Altitudes with forcing factors based on radiative forcing data with independent probability distributions are marked with black points. . . . . | 75 |
| 6.1  | Baseline designs optimized for minimum total operating costs and ATR with two devaluation rates, $r = 0$ and $r = 3\%$ . Black points indicate designs with listed cruise altitudes and Mach numbers. . . . .      | 85 |
| 6.2  | Designs optimized for minimum total operating costs and $\text{ATR}_{r=0}$ , applying propfan engines with varying assumptions. . . . .  | 88 |

|      |   |     |
|------|---|-----|
| 6.3  | A natural laminar flow narrowbody aircraft design from Ref. [20]. . . . .   | 90  |
| 6.4  | Designs optimized for minimum total operating costs and $ATR_{r=0}$ , applying natural laminar flow with varying assumptions. . . . .   | 91  |
| 6.5  | Designs optimized for minimum total operating costs and $ATR_{r=0}$ , applying biojet fuels with varying assumptions. . . . .   | 94  |
| 6.6  | Designs optimized for minimum total operating costs and $ATR_{r=0}$ , applying low $NO_x$ combustor technology with varying assumptions. . . . .                                    | 96  |
| 6.7  | Designs optimized for minimum total operating costs and $ATR_{r=0}$ , applying a contrail avoidance strategy with varying assumptions. . . . .                                      | 99  |
| 6.8  | Pareto front of normalized total operating cost and ATR with separate low contrails, $NO_x$ , and fuel burn technologies (each applied individually). . . . .                       | 100 |
| 6.9  | Pareto front of normalized total operating cost and ATR with combinations of low contrails, $NO_x$ , and fuel burn technologies. . . . .  | 103 |
| 6.10 | Pareto front of normalized total operating cost and ATR, showing 66% confidence intervals for reduction in ATR relative to the reference design. . . . .                            | 106 |
| 6.11 | Pareto front of normalized total operating cost and $CO_2$ emissions with climate impact reduction technologies. Evaluations of $ATR_{r=0}$ and $ATR_{r=3}$ are also shown. . . . . | 111 |
| 6.12 | Pareto front of normalized total operating cost and ATR with mitigation technologies and lower (left) and higher (right) fuel prices. . . . .                                       | 113 |
| 6.13 | Pareto front of normalized total operating cost and ATR with designs optimized over a long range mission. . . . .   | 114 |
| 6.14 | Pareto front of normalized total operating cost and ATR for designs with fixed configuration parameters representing conventional aircraft in the current fleet. . . . .            | 115 |
| A.1  | Diagram of engine station numbering, adapted from Ref. [21]. . . . .  | 124 |
| A.2  | Flow velocities through single and dual rotation propellers. . . . .  | 133 |
| A.3  | Fan polytropic and propulsive efficiencies as functions of fan pressure ratio for dual rotor and rotor-stator fan configurations. . . . .   | 138 |

# Chapter 1

## Introduction

### 1.1 Global Climate Change

A 2007 assessment of global climate change estimates that surface temperatures increased by  $0.76^{\circ}\text{C}$  between the years of approximately 1875 and 2003, with simultaneous increases in ocean temperature, global sea levels, and melting snow and ice.[4] The Intergovernmental Panel on Climate Change (IPCC) concluded that it is very likely (more than 90% probability) that most of the observed temperature rise is due to anthropogenic increases in greenhouse gas concentrations such as carbon dioxide.[4] Depending on future emissions, temperatures are expected to rise an additional  $1.5\text{--}3.4^{\circ}\text{C}$  by the end of the century, as shown in Figure 1.1. The IPCC describes the increasing likelihood of significant impacts on water availability, food production, coastal flooding, and ecosystems as higher temperatures are reached.[6] Examples of predicted consequences from temperature increases of more than  $2^{\circ}\text{C}$  include the exposure of millions of people to annual coastal flooding and increased risk of extinction of up to 30% of species.

A small but growing portion of global climate change is attributed to the aviation industry. In 2005, aircraft operations produced about 5% of the worldwide anthropogenic forcing that causes climate change.[1] Many predict that commercial aviation growth will continue to outpace improvements in efficiency, causing greater forcings over the next several decades.[1, 3, 22] Figure 1.2 depicts historical aviation

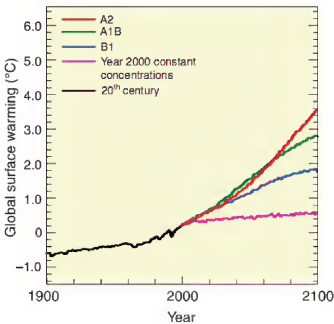


Figure 1.1: Observed global average surface temperature rise during the 20th century (black) and global climate model projections of future temperature rise for varying emissions scenarios (other colors), from Ref. [6].

fuel use and airline traffic and indicates strong growth since the beginning of the jet age despite numerous disruptive events, including the September 11, 2001 terrorist attacks.[1] Aviation fuel use growth has exceeded that of other industries, as illustrated by the increasing aviation carbon dioxide emissions fraction in Figure 1.2.

Aviation induced climate change results not only from the release of carbon dioxide, but also from emissions of nitrogen oxides, water vapor, and particles and from the effects of altered cloudiness. Of the climate forcing caused by aviation in 2005, carbon dioxide emissions produced forcing of  $0.028 \text{ W/m}^2$  (with a 90% likelihood range of 0.015-0.041), while other emissions caused forcing of  $0.049 \text{ W/m}^2$  (0.013-0.110).[1] Non-carbon dioxide forcing is caused almost entirely by nitrogen oxide emissions and cloud effects; crucially, these impacts vary significantly depending on an aircraft's cruise altitude. These sensitivities must be considered when assessing aircraft climate impacts.

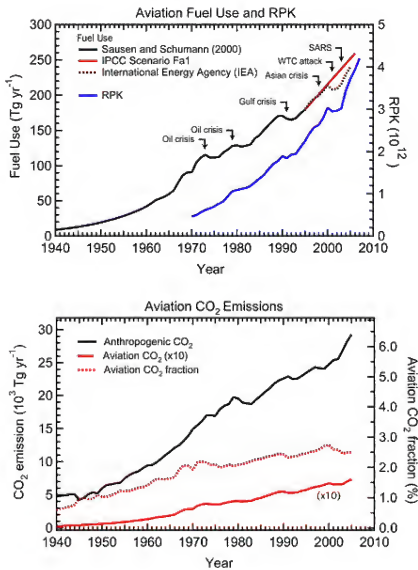


Figure 1.2: Historical and predicted aviation fuel use (top), and aviation and anthropogenic CO<sub>2</sub> emissions (bottom) (reprinted with permission from Elsevier).[1]

## 1.2 Aviation and the Environment

As the aviation industry continues to grow, so too have concerns over the environmental impacts of aircraft. Among these impacts are community noise exposure, degraded air quality in the vicinity of airports, and climate change from aviation greenhouse gas emissions and the alteration of cloud properties. The public has expressed objections to noise exposure since the industry's beginnings, but recent attention has shifted toward limiting aviation's effects on the global climate. The combination of greater public awareness, a rising number of individual airport regulations, and increasingly stringent international standards has created important environmental constraints in the design and operation of aircraft.

All aircraft certified since the 1980s have been required to meet environmental standards set by the International Civil Aviation Organization (ICAO) for community noise and emissions near airports.[23] The design relationships between aircraft operating costs, fuel consumption, community noise, and local airport emissions were investigated by Antoine.[7] Figure 1.3 compares the relative performance of aircraft designed to minimize a combination of operating costs and environmental objectives. Each point on the figure represents a unique aircraft design. Wing, engine, and mission design parameters were varied in these studies to achieve improved environmental performance relative to a minimum operating cost aircraft configuration. This research quantified both the potential improvements in environmental performance and associated penalties in terms of increased operating costs. In the figure, noise margin and landing and takeoff nitrogen oxide emissions (LTO NO<sub>x</sub>) metrics quantify environmental impacts in terms of ICAO regulatory measurements. Certification noise and emissions reductions of up to 15 decibels and 50%, respectively, were predicted alongside 10-25% increases in operating costs. These results also demonstrate the tradeoff between competing environmental constraints: for instance, designing exclusively for minimal LTO NO<sub>x</sub> emissions leads to aircraft configurations with increased fuel consumption and noise levels.

Antoine's research explored opportunities for improved environmental performance, focusing on regulated impacts from noise and local emissions. At present, there are no

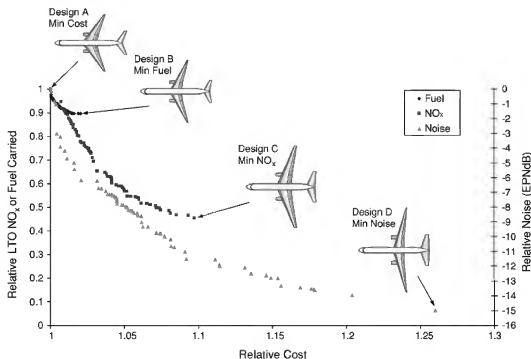


Figure 1.3: Pareto fronts of fuel carried, landing and takeoff NOx emissions, and cumulative certification noise, from Ref. [7].

certification standards aimed at controlling the climate impacts of aircraft emissions, although ICAO has expressed a commitment to develop a carbon dioxide emissions standard within the next two years.[23] A portion of aircraft climate impacts result from emissions of the greenhouse gas carbon dioxide and are directly proportional to fuel consumption. However, other impacts depend more complexly on ambient and engine operating conditions. Thus, the design of aircraft for reduced climate impacts is distinct from low fuel burn design. A number of studies have suggested technologies and operational strategies for reducing aircraft fuel consumption and/or climate impacts (e.g., Refs. [24, 25, 26, 22]). The effectiveness of each mitigation strategy depends on its combined effects on greenhouse gas and particle concentrations and on cloud radiative properties. To determine the feasibility of aircraft designed for reduced climate impacts, the tradeoffs between economic competitiveness and climate performance can be evaluated.

### 1.3 Contributions and Outline

In order to limit damages from climate change, improvements may be necessary in aircraft environmental performance. Extending the work of Antoine, this research develops a framework for quantifying and comparing the climate performance of future aircraft configurations using a conceptual design tool. Methods are presented for aggregating the time-varying climate effects of aircraft fleets into a single, meaningful metric. An integrated approach is taken, assessing how design changes influence operating costs, fuel consumption, emissions rates, induced climate change, and basic aircraft performance. The effects of climate impact reduction technologies are investigated, revealing several design and operation strategies for drastically reducing the climate impacts of future aircraft.

A brief thesis outline is as follows. Chapter 2 describes the effects of aircraft emissions on global climate and approaches to modeling emissions and climate impacts. Chapter 3 discusses climate metrics and proposes the average temperature response metric for aircraft design studies. Chapter 4 considers aircraft performance analysis methods, including a new variable bypass ratio turbofan and propfan engine model. Chapter 5 presents a linear, altitude-varying climate model that can be integrated with an aircraft conceptual design tool. Chapter 6 discusses aircraft design studies and explores the benefits of aircraft climate mitigation strategies. Finally, Chapter 7 summarizes key conclusions and contributions of this research. A number of opportunities for future research are also mentioned.

## Chapter 2

# Aircraft Climate Impacts

### 2.1 Introduction

Concern regarding aviation's environmental impacts has grown during the last several decades, leading to the development of international regulations on noise and emissions in the vicinity of airports. More recently, the impacts of aircraft emissions on global climate have attracted attention. Commercial aircraft operations affect the atmosphere and climate through emissions of greenhouse gases and their precursors and through the formation of contrails and cirrus clouds. Since the majority of emissions are released at high altitudes, these effects are not currently regulated. Assessments of aviation's climate impacts began in the late 1990s, culminating with the IPCC Special Report, *Aviation and the Global Atmosphere*.<sup>[27, 3]</sup> Knowledge of aircraft climate impacts improved following numerous research programs, and in 2009, the qualitative and quantitative conclusions of the IPCC report were comprehensively updated.<sup>[1, 22]</sup> Aviation emissions in 2005, including the highly uncertain effects of induced cirrus cloudiness, were responsible for about 5% of all anthropogenic radiative forcing,<sup>[1]</sup> which measures the net radiation imbalance at the top of the atmosphere due to a perturbation. Based on the industry's current trajectory, aviation radiative forcing is predicted to grow by a factor of 3.0-4.0 between 2000 and 2050.<sup>[1]</sup> To determine the effects of future aircraft operations on climate, methods are needed to estimate total aircraft emissions and to model resulting climate impacts. This chapter first discusses

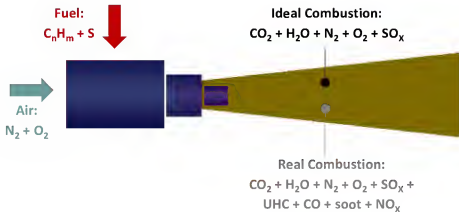


Figure 2.1: Products of aircraft fuel combustion, adapted from Ref. [8].

the effects of aircraft operations on climate and next describes emissions and climate models of varying complexity and accuracy.

## 2.2 Aircraft Emissions and Climate

Commercial aircraft engines are powered by the combustion of a hydrocarbon fuel, the byproducts of which affect global climate. Jet A-1 fuel has an average carbon-hydrogen ratio of  $C_{12}H_{23}$  and contains approximately 400 parts per million by mass of sulfur.[22, 28] The fuel is combusted to ideally produce carbon dioxide ( $CO_2$ ), water vapor ( $H_2O$ ), and sulfur oxides ( $SO_x$ ). The mass of  $CO_2$ ,  $H_2O$ , and  $SO_x$  emitted per kilogram of burned fuel depends on the exact fuel composition. Total annual emissions from the global commercial fleet in 2006 are listed in Table 2.1.[2] In real combustion, trace amounts of unburned hydrocarbons (UHC), carbon monoxide (CO), soot, and nitrogen oxides ( $NO_x$ ) are also released, as given in Figure 2.1.[3] Emission rates for these species are small compared with  $CO_2$  and  $H_2O$  rates, as indicated in Table 2.1. Of these combustion products,  $CO_2$ ,  $H_2O$ ,  $NO_x$ ,  $SO_x$ , and soot each directly or indirectly alter the radiative balance of the Earth system over different timescales.

The IPCC and other groups have published extensive reviews of aviation's climate impacts.[27, 3, 29, 1, 22] Figures 2.2 and 2.3 provide overviews of aviation induced

| Species  | Emission Quantity |
|--|-------------------|
| CO <sub>2</sub> emissions (Tg C)                 | 162.25            |
| H <sub>2</sub> O emissions (Tg H <sub>2</sub> O) | 232.80            |
| NO <sub>x</sub> emissions (Tg NO <sub>2</sub> )  | 2.656             |
| CO emissions (Tg CO)                             | 0.679             |
| SO <sub>x</sub> emissions (Tg S)                 | 0.111             |
| HC emissions (Tg CH <sub>4</sub> )               | 0.098             |
| Organic particulate matter emissions (Tg)        | 0.0030            |
| Sulfur particulate matter emissions (Tg)         | 0.0023            |
| Black carbon particulate matter emissions (Tg)   | 0.0068            |

Table 2.1: Annual emissions from global commercial aviation in 2006.[2]

climate change. Figure 2.2 shows the relationship between aircraft emissions, atmospheric composition, radiative forcing, climate change, and impacts.[1] When concentrations of greenhouse gases and particles are perturbed, the balance of incoming solar and outgoing infrared radiation is altered, causing radiative forcing. Forcing influences climate properties, such as temperature, precipitation, and extreme weather events. These changes in climate affect many systems, including availability of food, water, and energy. Finally, impacts can be translated into damages to social welfare. The relative importance of each aircraft emission species depends on the chosen climate metric, but radiative forcing is often used by the IPCC. Figure 2.3 shows the instantaneous radiative forcing experienced in 2005 due to aircraft emissions since the beginning of the jet age in the 1940s.[1] The current, consensus scientific understanding of radiative forcing sources listed in Figure 2.3 are described in the following sections. It should be noted that in the future, as knowledge is gained, conclusions about the magnitudes and types of radiative forcing caused by aircraft emissions are likely to change.

Climate impacts from aviation emissions differ from those of ground source emissions in two key ways. First, the ratio of non-CO<sub>2</sub> to CO<sub>2</sub> impacts for aviation emissions is significantly greater than the same ratio for ground source emissions. For instance, using instantaneous forcing in 2005 shown in Figure 2.3, non-CO<sub>2</sub> emissions extend CO<sub>2</sub> radiative forcing by a factor of 2.8; by comparison, for all global

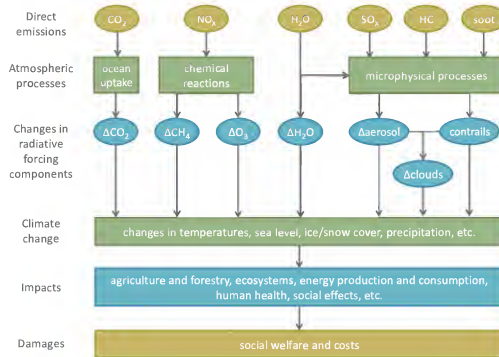


Figure 2.2: Schematic diagram of relationship between aircraft emissions and climate impacts (reprinted with permission from Elsevier). [1]

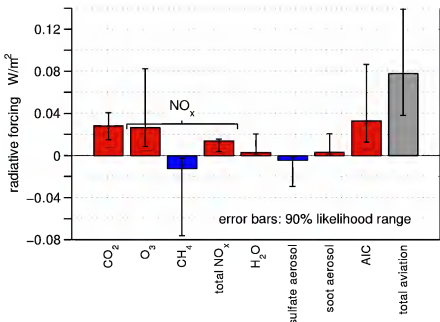


Figure 2.3: Radiative forcing in the year 2005 due to all previous aircraft emissions (reprinted with permission from Elsevier).[1]

anthropogenic forcing, this scaling factor is approximately 0.96, representing a small net cooling effect from non- $\text{CO}_2$  emissions.[1] High ratios of aviation non- $\text{CO}_2$  to  $\text{CO}_2$  impacts are also measured with many other metrics.[22] Secondly, aircraft emissions are deposited directly into the upper troposphere and lower stratosphere, leading to more effective ozone production and the formation of contrail and cirrus clouds.

### 2.2.1 Carbon Dioxide

$\text{CO}_2$  is a direct product of fossil fuel combustion and a greenhouse gas. Anthropogenic increases in greenhouse gas concentrations affect climate by absorbing outgoing infrared radiation from the Earth system, thereby warming and causing increased surface temperatures.  $\text{CO}_2$  has a long atmospheric lifetime associated with the timescales of ocean and biosphere uptake. Following a pulse of  $\text{CO}_2$  emissions, approximately 50% of emissions remain in the atmosphere after 30 years and 30% remain after 200

years according to an IPCC model.[4] Because CO<sub>2</sub> lifetime is longer than atmospheric circulation timescales, the gas becomes well-mixed in the atmosphere and impacts from aircraft CO<sub>2</sub> emissions are indistinguishable from impacts of CO<sub>2</sub> emissions from other sources. Figure 2.3 shows radiative forcing in 2005 caused by all past aviation CO<sub>2</sub> emissions. A portion of this forcing is caused by recent emissions, but because CO<sub>2</sub> has a long atmospheric lifetime, the remaining forcing is attributable to CO<sub>2</sub> released many years earlier and remaining in the atmosphere in 2005. CO<sub>2</sub> emissions are a significant cause of aviation climate change in combination with NO<sub>x</sub> emissions and aircraft induced cloudiness.

### 2.2.2 Water Vapor

Water vapor is also a direct fuel combustion product and a potent greenhouse gas. However, unlike CO<sub>2</sub> emissions, H<sub>2</sub>O emissions within the troposphere and lowermost stratosphere have a very short atmospheric lifetime controlled by the hydrological cycle. At altitudes of 30,000 to 40,000 ft, typical H<sub>2</sub>O perturbation lifetimes range from a week to a month, and are even shorter at lower altitudes.[22] Because of their short residence time, subsonic aircraft H<sub>2</sub>O emissions do not have strong climate impacts, as shown in Figure 2.3. Water vapor emissions at higher altitudes, including those deposited by a potential future supersonic fleet, have longer residence times and would likely produce significant climate impacts.[3] Although the direct impacts from H<sub>2</sub>O emissions are small, water vapor plays a key role in the formation of aerosol particles and clouds, as shown in Figure 2.2.

### 2.2.3 Nitrogen Oxides

NO<sub>x</sub> refers collectively to NO and NO<sub>2</sub> and is the third most abundant engine emission species after CO<sub>2</sub> and H<sub>2</sub>O. These gases initially form in the hottest regions of the engine combustor through the oxidation of atmospheric nitrogen.[3, 30] NO<sub>x</sub> emissions indirectly impact climate via chemical reactions that alter concentrations of the greenhouse gases ozone (O<sub>3</sub>) and methane (CH<sub>4</sub>).[22] Increases in levels of either of these gases cause positive radiative forcing, while losses cause negative forcing. NO<sub>x</sub>

emissions also affect climate through the formation of particulate nitrate;[31, 4] however, the associated negative radiative forcing is very uncertain and is not modeled in this research.

First,  $\text{NO}_x$  emissions produce positive forcing by increasing concentrations of  $\text{O}_3$ , which has a chemical lifetime on the order of several weeks.[22] The cause of this  $\text{O}_3$  perturbation is twofold. Ozone production rate is enhanced as  $\text{NO}$  emissions convert to  $\text{NO}_2$ , which photolyses to produce atomic oxygen, then reacts with molecular oxygen to produce  $\text{O}_3$ . Additionally, the  $\text{O}_3$  loss rate decreases due to lower abundance of the peroxy radical, which is consumed in the conversion of  $\text{NO}$  to  $\text{NO}_2$ .[22]  $\text{NO}_x$  emissions in the mid-latitude upper troposphere and lower stratosphere produce  $\text{O}_3$  more efficiently in terms of molecules of  $\text{O}_3$  per molecule of  $\text{NO}$  than anywhere in the atmosphere.[3] Assessments of these short-lived effects indicate increased  $\text{NO}_x$  and  $\text{O}_3$  concentrations of 30-40% and 3%, respectively, near flight corridors.[22] It should be noted that  $\text{NO}_x$  emissions in the stratosphere, for instance from supersonic aircraft, cause net  $\text{O}_3$  destruction. The crossover altitude where  $\text{NO}_x$  emissions convert from net  $\text{O}_3$  production to destruction is estimated to be near 16 km, or 52,000 ft.[22]

Secondly,  $\text{NO}_x$  emissions accelerate the rate of destruction of ambient  $\text{CH}_4$  over longer timescales on the order of 12 years. Associated with this process is low magnitude, long-term ozone destruction. Because these cooling impacts occur over decades, their forcings become mixed on a hemispheric scale, in contrast with short-term ozone production forcing that remains concentrated near flight routes. The warming, cooling, and net impacts of  $\text{NO}_x$  emissions in the year 2005 from all past aviation emissions are illustrated in Figure 2.3.[1] As noted previously, short-term impacts shown in this chart result only from recent emissions, while long-term forcing includes forcing from all remaining past perturbations.

#### 2.2.4 Sulfur Oxides

Aviation fuel contains a small percentage of sulfur, most of which is oxidized to sulfur dioxide ( $\text{SO}_2$ ) in the combustor. A fraction of this  $\text{SO}_2$  is further oxidized via gas phase chemical reactions inside the engine and plume to sulfur trioxide ( $\text{SO}_3$ ) and sulfuric

acid ( $\text{H}_2\text{SO}_4$ ). Liquid particles of  $\text{H}_2\text{O}$  and  $\text{H}_2\text{SO}_4$  form via homogeneous nucleation, and they grow in size by coagulation and condensation processes. The result is an increase in sulfate aerosol number and area density near flight routes. Sulfate particles scatter incoming solar radiation and absorb very little outgoing infrared radiation, leading to a net cooling impact. Sulfate aerosol production from aircraft is small relative to surface and volcanic sources, and these particles have very short lifetimes of approximately four days.[3, 32] Figure 2.3 illustrates the small direct impact from sulfate aerosol emissions, but sulfate particles also play a role in the formation of contrail and cirrus clouds.[1]

### 2.2.5 Soot Particles

Carbon soot particles containing graphite carbon and organic compounds form in aircraft engine combustors. Emission rates vary in a complex manner with combustor operating conditions and design but generally increase with engine throttle setting.[33] The development of engine emissions regulations has lowered soot emission rates, demonstrated by modern engine emission rates that are 40 times lower than those of 1960s engines.[1] Total annual commercial aviation emission rates for organic and black soot particulate matter in the year 2006 are listed in Table 2.1. Soot absorbs solar radiation very effectively, producing the small warming effect shown in Figure 2.3. Like sulfate particles, the atmospheric lifetimes of soot particles are very short, on the order of approximately one week.[32] On average, the direct impacts of soot particles are small, but these particles can also serve as nucleation sites for contrail particles. A recent global climate model assessment concluded that direct impacts from aviation soot emissions could be greater than previously expected, particularly in the Arctic circle.[34]

### 2.2.6 Aviation Induced Cloudiness

Aviation induced cloudiness (AIC) includes the formation of linear contrails, aged contrail-cirrus, and soot cirrus clouds. These clouds reflect incoming solar radiation and trap outgoing infrared radiation, producing a net positive radiative forcing

on average. The magnitude of forcing caused by individual clouds varies diurnally, with nighttime contrails causing considerably greater warming effects than daytime contrails.[35] The impacts of these phenomena are very uncertain, particularly for contrail-cirrus and soot cirrus.

Linear condensation trails, or contrails, form when hot, moist air in the engine exhaust mixes with sufficiently cool ambient air. The threshold temperature for contrail formation is determined by the Schmidt-Appleman criterion, which describes whether liquid saturation is reached within the young aircraft plume in terms of ambient and exhaust temperatures and water content. If temperature conditions are met, water vapor condenses onto exhaust particles, and these liquid droplets freeze. The radiative impacts of contrails are negligible unless the ambient air is supersaturated with respect to ice, causing the contrail to persist for as long as the air remains ice-supersaturated, often several hours.[36] Conditions for persistent contrail formation can exist between the altitudes of 20,000 and 45,000 ft, with a peak frequency of about 15% at 30,000 ft altitude.[15] Approximately one-third of the AIC forcing shown in Figure 2.3 is attributed to linear contrails. However, there is significant uncertainty in quantifying net contrail impacts, which depend on accurate models of contrail coverage and optical depth.[1]

Aviation cirrus can be formed either from the spreading of linear contrails, known as contrail-cirrus, or from the increase in the number of particles near cruise altitudes that can act as cloud condensation nuclei, known as soot cirrus. Contrail-cirrus are estimated to increase contrail coverage by a factor of 1.8, although estimates of its addition to forcing are highly uncertain. Uncertainties in quantifying forcing due to soot cirrus are even greater. Soot cirrus includes the alteration of ambient cloud properties and the formation of new cirrus clouds. It is currently not known whether net soot cirrus forcing is positive or negative. Aviation cirrus impacts are sometimes excluded from overall aviation forcing estimates due to their high uncertainty; however, these impacts and their uncertainties are included in this research. Figure 2.3 estimates the net total forcing due to all three components of aviation cloudiness, and this value is derived from correlation analyses of cloud coverage and air traffic by assuming cloud properties similar to thin cirrus.[1]

## 2.3 Aircraft Emissions Regulations

Industry-wide environmental standards are developed for commercial aviation by the International Civil Aviation Organization (ICAO) through its Committee on Aviation Environmental Protection (CAEP). For an aircraft engine to be certified, it must meet landing and takeoff emissions standards designed to protect air quality near airports. These regulations apply to engine certification and do not account for total aircraft emissions; thus, within this regulatory framework, aircraft with greater sea level static thrust can have higher overall emissions rates, irrespective of differences in payload or range. At present, there are no ICAO regulations limiting cruise emissions, but future policies to limit climate impacts are under consideration.[23]

Landing and takeoff (LTO) emissions standards exist for NO<sub>x</sub>, CO, UHC, and soot (as measured by smoke number). Of these pollutants, only NO<sub>x</sub> emissions produce significant climate impacts. Regulations for NO<sub>x</sub> emissions have been made increasingly stringent over the past three decades and CAEP6 limits are currently in effect.[23] These regulations limit the total mass of emissions released per unit thrust during a landing-takeoff cycle, representing emissions below 3,000 ft. Emissions are measured for simulated taxi, takeoff, climb out, and approach conditions. Standards vary with engine pressure ratio, allowing engines with higher combustor pressures and temperatures to emit more NO<sub>x</sub>. Emissions and fuel burn measurements for all certified engines are published in the ICAO Emissions Databank.[37] Although only landing and takeoff emissions are regulated, it is generally assumed that reductions in LTO emissions are accompanied by reductions in cruise NO<sub>x</sub>.[22]

## 2.4 Emissions Modeling

Current emissions regulations target pollution during landing and takeoff only, but, the majority of emissions are released above 3,000 ft altitude and these emission rates are not included in ICAO Databank measurements. To determine the climate impacts of a future aircraft fleet, emissions must be modeled over the entire mission. Different methods of varying complexity exist for estimating emissions, but for conceptual

design, computationally efficient methods are needed. Following ICAO measurement procedures, emission rates are described by the emissions index or the mass ratio of emitted species to consumed fuel.

### 2.4.1 Fuel-Proportional Emissions

For many radiatively important species, total emissions are simply proportional to fuel consumption. The mass of  $\text{CO}_2$ ,  $\text{H}_2\text{O}$ , and  $\text{SO}_x$  released per fuel burned is determined from the composition of the fuel. These species have emissions indices that are constant between different designs and over all operating conditions.

### 2.4.2 $\text{NO}_x$ P3-T3 Method

$\text{NO}_x$  emissions index, on the other hand, varies significantly with both engine design characteristics and operating conditions. The formation of  $\text{NO}_x$  in an aircraft engine combustor involves unsteady physical processes and non-equilibrium chemical reactions and is complex to model analytically.[38, 30, 3, 39] Empirical methods have been developed based on experimental data to more simply relate emission rate to relevant combustor parameters. These correlations estimate  $\text{NO}_x$  emissions index based on models of combustor residence time, chemical reaction rates, and mixing rates.[40] For a fixed combustor design, emissions index can be estimated to a high degree of accuracy (better than 5%) from combustor inlet temperature and pressure based on experimental data.[3] Such models, referred to as P3-T3 methods, exist for numerous conventional and advanced combustor configurations. An example of a P3-T3 model is described in more detail in Chapter 5. These approximate methods greatly simplify the estimation of  $\text{NO}_x$  emission rate and do not capture all variations in emission rates with changing conditions. Moreover, P3-T3 models are only accurate for the specific combustor configuration for which the correlation is derived.

### 2.4.3 Fuel Flow Correlation Methods

NO<sub>x</sub> P3-T3 correlation methods rely on knowledge of combustor inlet temperature and pressure for emissions index estimation. Information about the variation of these parameters with operating condition requires proprietary information or detailed engine models that may not be available for conceptual design studies or development of emissions inventories. For this reason, more simple fuel flow correlation methods have been developed. These methods compute NO<sub>x</sub> emissions index at any operating condition based on ambient conditions, fuel flow rate, and publicly available ICAO landing and takeoff certification data. Fuel flow correlations are less accurate than P3-T3 methods but require less knowledge of detailed combustion parameters. Two common methods, the Boeing Method 2 and DLR fuel flow correlations,[41, 42] have been applied in numerous studies of aviation emissions.[43, 44, 8, 45, 46] These models replicate cruise emissions index measurements and P3-T3 predictions to within approximately  $\pm 10\%.$ [8]

Fuel flow correlation methods also exist for estimating cruise soot emissions index;[42] however, direct soot climate impacts are small compared with aircraft CO<sub>2</sub>, NO<sub>x</sub>, and aviation induced cloudiness. Therefore, soot emissions index is assumed to be constant over all operating conditions without significant loss in accuracy for total climate impact estimation. For detailed combustor technology studies, a more accurate model for soot emissions would be necessary.

## 2.5 Climate Impact Modeling

A variety of model types are used to predict the impacts of past and future anthropogenic activities on global climate. The IPCC recognizes the need for a spectrum of models, each with a level of complexity and simulation quality appropriate for different study applications.[4] This section describes three categories of climate models.

### 2.5.1 Global Climate Models

Global climate models (GCMs) are complicated mathematical representations of the fluid dynamics and chemistry associated with the atmosphere, ocean, and land surface. These programs vary in complexity and are used to predict the impacts of anthropogenic emissions on climate. The most complex models are three-dimensional coupled atmosphere-ocean general circulation models (AOGCMs), and 23 such models were applied in the recent IPCC Fourth Assessment Report.[4] Climate modeling has advanced substantially over the last several decades: the IPCC stated that “there is considerable confidence that climate models provide credible quantitative estimates of future climate change, particularly at continental scales and above.”[4] This confidence arises from the fundamental principles upon which models are based and their ability to reproduce observations of past and present climate change.[4] However, global climate models are computationally expensive, taking weeks or months to evaluate.[47] As a result, global climate models are not well-suited for applications requiring multiple calculations, such as uncertainty evaluations or conceptual design studies.[48]

### 2.5.2 Integrated Assessment Models

Integrated assessment models (IAMs) are tools developed to assess the environmental and economic system responses of prescribed anthropogenic activity scenarios. These methods do not model the physical and chemical processes of climate change as accurately as global climate models, but instead quantify global and regional economic impacts.[49] Three commonly applied IAMs include the FUND, DICE, and PAGE models. Each model converts emissions into concentration change, temperature change, and finally social costs. Damage functions translate warming into economic costs and rely on the climate modeling community’s best judgments, but these representations are incomplete and highly uncertain.[50] IAMs are useful tools, designed to inform climate change policy decisions.

### 2.5.3 Linear Temperature Response Models

Linear temperature response (LTR) models are simplified representations of the climate system based on results from global climate models. Instead of computing concentrations, radiative forcing, and temperature change on a time-varying, three-dimensional global grid, most LTRs estimate globally- and annually-averaged conditions. LTRs are less accurate than GCMs but are expected to capture first order effects from emissions and have the useful properties of computational efficiency, transparency, and flexibility to incorporate new knowledge.[51, 52] As a result, LTRs are valuable for aviation studies, and especially conceptual design optimization studies where many emissions scenarios must be considered. Because of their low computational costs, uncertainty analysis can be performed with LTRs to determine the degree of confidence in result estimates.

LTRs have been developed for numerous past aviation studies.[51] Sausen and Schumann applied a linear model based on the response functions of Hasselmann et al. to compare the effects of CO<sub>2</sub> and NO<sub>x</sub> emissions.[53, 54] More recently, Marais et al. developed the Aviation Environmental Portfolio Management Tool, which estimates not only temperature change, but also damages based on linear response functions.[55] Lim et al. apply the LinClim tool, which is similar to the model of Sausen and Schumann, but includes the effects of more emissions species.[47] Finally, the LTR AirClim, developed by Grewe and Stenke, computes impacts based on effects over a coarse global grid with varying impact intensities.[56] A linear temperature response model with similar elements to many of these methods and designed for use in conceptual design studies is described in Chapter 5.

# Chapter 3

## Climate Change Metrics

### 3.1 Introduction

Given the significance of aviation climate change, it is important for the aircraft design community to have a meaningful method for measuring the climate impacts of various aircraft configurations and technologies. This estimation must account for the multiple radiatively active species that aircraft emit. Emissions of CO<sub>2</sub>, NO<sub>x</sub>, H<sub>2</sub>O, SO<sub>x</sub>, and soot from fuel combustion alter both atmospheric composition and cloud properties. The causal sequence of emissions to the impacts and damages caused by climate change is shown in Figure 3.1. Atmospheric processes convert direct aircraft emissions into chemicals and form clouds that change the balance of incoming and outgoing energy in the Earth-atmosphere system, producing radiative forcing. Radiative forcing components then cause climate change, manifested as changes to global mean temperature, precipitation, sea level, etc. Next, climate change influences agriculture, coastal geography, and other systems. The likelihood of significant impacts on these systems as a function of temperature rise is explored by the IPCC.[6] Finally, climate change impacts can be quantified monetarily as damages or costs to society.

Along each step of the path shown in Figure 3.1, variables can be identified which could serve as climate change metrics. Metrics based on lower steps in the figure are increasingly relevant in quantifying the potential effects of climate change sought to be avoided. However, these quantities are also increasingly uncertain and difficult to

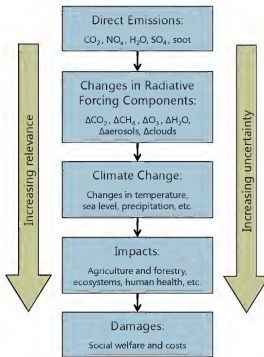


Figure 3.1: Cause and effect chain for aircraft climate change.[9]

predict. When selecting a metric for measuring climate change, one must balance the relevance of the metric against the uncertainty its use leads to in making decisions. In this chapter, first, metrics generally applied for different climate applications are described. Next, the suitability of metrics for aircraft conceptual design are considered, and a methodology for estimating aircraft climate performance with a single candidate metric is presented. The candidate metric, average temperature response, can be combined with a simple climate model to provide a framework for assessing relative performance of competing aircraft designs.

## 3.2 Commonly Used Climate Metrics

Several different metrics have been developed to quantify impacts from climate change. Five of the most commonly used metrics are briefly described in this section: mass of emissions, radiative forcing, global warming potential, global temperature potential, and damages. Applications for these metrics range from IPCC global scenario assessments to individual sector studies to international policy analyses.

### 3.2.1 Mass of Emissions

One very simple metric quantifies climate effects in terms of the total mass of emissions, usually CO<sub>2</sub>. Because CO<sub>2</sub> has a long atmospheric lifetime and its impacts are comparatively well understood, metrics based on mass of CO<sub>2</sub> emissions can be meaningful. However, for applications with numerous emission species of varying atmospheric lifetimes, mass-based metrics are less useful.

### 3.2.2 Radiative Forcing

As previously noted, radiative forcing (RF) measures the net imbalance of incoming and outgoing energy in the Earth-atmosphere system caused by a perturbation. RF does not directly measure a change in climate behavior, but instead quantifies the change in energy that produces changes in climate properties including temperature and precipitation. However, under certain restrictive assumptions, RF is directly related to changes in equilibrium surface temperature.[3] While RF is usually reported as a snapshot at a single time, RF can also be used as a time-varying climate metric. RF metrics have been applied extensively in climate change research, including studies by the IPCC.[3]

### 3.2.3 Global Warming Potential

Global warming potential (GWP) is defined as the time-integrated RF caused by a pulse emission of a particular forcing agent over a specified time period, normalized by the time-integrated RF due to a pulse emission of CO<sub>2</sub> over the same specified period.

Alternatively, sustained GWPs may also be defined based on continuous emissions over a specified time horizon. Different time periods may be considered, but 100 years is commonly used and was adopted by the United Nations Framework Convention on Climate Change for the Kyoto Protocol. GWPs have been widely reported for long-lived gases including CO<sub>2</sub>. More recently, GWPs for short-term perturbations from NO<sub>x</sub> emissions and AIC effects have been published, although these potentials are more difficult to quantify.[32]

### 3.2.4 Global Temperature Potential

Global temperature potential (GTP) quantifies the ratio of global mean temperature changes resulting from equal mass emissions of CO<sub>2</sub> and another species.[18, 28, 57] GTP is a snapshot metric that evaluates temperature change at a single point at the end of a time horizon, rather than evaluating time-integrated impacts. Similar to GWPs, GTP emissions scenarios may be based on either pulse or sustained emissions. Lastly, GTPs can be calculated with any climate model, but simplified linear climate models are often used.[28]

### 3.2.5 Damages and Other Economic Metrics

Economic metrics evaluate the damages and abatement costs of different emissions scenarios. Integrated assessment model studies, described in Chapter 2, usually quantify impacts in economic terms (e.g., Refs. [58, 59, 60, 55]). These metrics are particularly useful for aggregating impacts of varying type and location to inform policy decisions. Still, there are no approaches to estimating climate change impacts in economic terms that are widely accepted by the climate change community.[51]

### 3.3 Climate Metric for Comparative Aircraft Design

Researchers have adopted numerous climate metrics to quantify the impacts of aviation emissions, including those discussed in the previous section. The strengths and weaknesses of these metrics are reviewed in Refs. [61, 18, 62, 63, 51, 52, 32, 28]. Many of these metrics have been applied extensively to the comparison of impacts from different sectors, the prediction of impacts based on future emission scenarios, and the assessment of various technology and policy mitigation strategies. In order to compare the climate impacts of different aircraft designs, a metric is needed that appropriately characterizes the net global climate effect of operation of a fleet of particular aircraft. To narrow the set of possible aircraft design climate metrics, discussion will focus on the appropriate properties of a metric for this purpose. Then, a candidate metric for comparative aircraft design is presented.

#### 3.3.1 Desired Metric Properties

**Measured Quantity** A climate metric could measure many different physical or economic values, ranging from mass of emissions to radiative forcing to temperature change to impacts and damages, as shown in Figure 3.1. For estimating the impacts of aircraft operations, the mass of radiatively active emissions is not a meaningful metric because of the wide variety of aircraft emissions that affect climate. For example, the timescales and intensity of climate impacts due to emissions of one kilogram of CO<sub>2</sub> are very different from those of one kilogram of NO<sub>x</sub>; furthermore, AIC impacts are not simply related to a single emissions quantity. Because of this, emissions quantity metrics are less useful for aircraft design studies.

Economic metrics evaluate the damages and abatement costs of different emissions scenarios. These economic metrics use damage functions that estimate the effects of climate change in terms of the consumption-equivalent value of both market and non-market goods.[50] Such models are highly uncertain: Nordhaus describes the damage function in his model as “extremely conjectural given the thin base of

empirical studies on which it rests.” [64] Uncertainty in estimating damages is more challenging to quantify and greater in magnitude than that of physical metrics such as radiative forcing and temperature change. Furthermore, temperature change is a tangible measure of climate change that is more accessible than damage metrics, and many policies focus on the objective of temperature rather than social damages. For comparative studies, under certain restrictive assumptions described in Ref. [63], conclusions drawn using global cost potential and global temperature potential metrics coincide. Additionally, because the purpose of this metric is for use in aircraft design, and not policy decisions, economic metrics are not necessarily preferred. To inform future policy decisions, it is important to measure each environmental impact (noise, local emissions, and climate change) and understand how environmental and economic performance can be changed in design. For these reasons, economic-based metrics will not be used herein for comparative aircraft design study.

Other climate properties include radiative forcing and temperature change. Both are physical quantities often noted in climate change studies. Unlike forcing, temperature change is a direct measure of a change in global climate behavior. RF is therefore a less direct measure of the level of impact of aircraft emissions. RF has the advantage of lower scientific uncertainty compared with temperature change. The primary limitation of RF is that it is an instantaneous metric which captures impacts from emissions at a single point in time; however, time-integrated RF metrics can be used to quantify lifetime impacts. Both radiative forcing and temperature change are identified as potential candidates for the basis of an aircraft design climate metric.

**Emissions Case** Most climate metrics are computed based on a specified, general emissions case. For instance, sustained 100 year GWPs are calculated assuming constant emissions for 100 years while pulse 100 year GWPs are calculated assuming emissions for only one year and zero emissions thereafter. GWPs are used broadly for many applications and are also referenced for 20 year and 500 year horizons. For the application of aircraft design, a more specific emissions case is appropriate. To compare the impacts of different aircraft designs, climate impacts can be computed with an emissions case representative of the likely operation of these designs. Based

on typical commercial aircraft operation today, an appropriate emissions case might be constant operation for 30 years followed by aircraft retirement and zero emissions (other operating lifetimes could be considered for different aircraft design applications). The scenario of constant emissions during the operational lifetime and zero emissions thereafter is a simplistic representation of the emissions from a new aircraft design – in reality, new aircraft are adopted gradually and the net emissions rates from the new design change annually. However, this simple emissions case is sufficient to capture the differences in lifetime climate impacts in a comparative design study.

**Snapshot vs. Integrated Impact** A climate metric can be based on the evaluation of a property at a single point in time or the integration of that property over a period of time. Common snapshot metrics include single year RF and GTP, and common integrated metrics include GWP and integrated temperature change.[55, 32, 28] For aircraft design, a snapshot metric can be applied at the end of the operating lifetime, quantifying the value of a climate property near its peak value. Snapshot metrics could also be applied within or after the operating lifetime if considering a climate goal, for instance a temperature change target in the year 2050. It should be noted that even for a comparative study, snapshot metrics are very sensitive to timing, and a study with a lifetime of 10 years could give a different result than that with a lifetime of 50 years. Time-integrated climate metrics are less sensitive to lifetime and quantify mean impacts over an integration period. Because components of RF and temperature change are accumulative and vary annually, lifetime-averaged metrics are preferred for aircraft design studies.

**Temporal Weighting** Given an integrated impact metric based on the emissions case described above, the relative importance of short-lived and long-lived impacts can be altered by applying temporal weighting. Common methods for weighting include discounting and windowing, but other weighting functions can also be used. Discounting is frequently used in economic studies to express future value in present

monetary terms and has been applied in climate change studies.[65, 66, 55] In a similar manner as discounting, weighting factors can be applied to a physical impact to specify the relative importance of immediate and far future impacts. Integration window also affects this balance by setting the maximum time horizon for inclusion of impacts. Short-lived impacts decay quickly (10-30 years) after aircraft operations terminate but long-lived impacts decay slowly (hundreds of years for CO<sub>2</sub>). Therefore, an integration window that is long compared with the aircraft operating lifetime favors long-lived impacts, while a short window biases toward short-lived impacts. A weighting function can combine weighting factors and an integration window. Because choices of weighting represent judgments on the value of immediate and far future impacts, an aircraft design climate metric should be flexible and allow of user specification of the associated function.

**Treatment of Uncertainty** Considerable uncertainty exists in the quantification of climate impacts from aircraft emissions and other sources. The relevant uncertainty may be categorized as described in Ref. [67]. Scientific uncertainty is associated with limits in scientific knowledge and inexact modeling approaches for estimating impacts from an emissions scenario. Valuation uncertainty exists because value judgments are required to temporally weight impacts. Scenario uncertainty refers to unknowns surrounding the projections of future anthropogenic activities and system responses that are required to estimate aircraft climate impacts. For an aircraft design climate metric to be practical, scientific uncertainty must be quantifiable. The effects of scientific uncertainties on design results can be quantified using the approach described in Chapter 5. Scenario and valuation uncertainty should also be addressed by allowing user specification of trajectory and temporal weight assumptions.

### 3.3.2 Average Temperature Response

Based on the discussion of the desired properties of an aircraft design climate metric, several metrics could be conceived. One such metric, average temperature response, is presented here. This metric is based on temperature change for several reasons. First, temperature change is commonly used within the climate modeling community

but is also understood by non-experts. Secondly, it measures a physical change in climate behavior that could be controlled in order to limit climate change damages. The purpose of the candidate metric is to quantify for a particular aircraft the climate impacts realized from emissions during operation and also climate impacts that result from perturbations remaining in the Earth-atmosphere system after the aircraft's operating lifetime has ended.

The metric presented in this study is the average temperature response (ATR) over an aircraft's operating lifetime. ATR combines integrated temperature change with the concept of temporal weighting and follows the general emissions metric formulation given in Refs. [4, 60]. Average temperature response is defined in equation (3.1).

$$ATR_H = \frac{1}{H} \int_0^{\infty} \Delta T_{\text{sust},H}(t) w_r(t) dt \quad (3.1)$$

ATR is measured in units of temperature. The first step in computing ATR is calculating the global mean temperature change. In the above equation,  $\Delta T_{\text{sust},H}$  refers to the time-varying global mean temperature change caused by  $H$  years of sustained operation of a particular aircraft configuration. The function  $\Delta T_{\text{sust},H}(t)$  is determined based on constant annual emissions rates for the first  $H$  years of CO<sub>2</sub>, NO<sub>x</sub>, H<sub>2</sub>O, soot, and sulfate, and constant stage length, and zero emissions thereafter. Aircraft operating lifetimes typically range between 25 and 35 years [3]. All studies herein assume an operating lifetime ( $H$ ) of 30 years.

Temperature change can be quickly calculated using a linear temperature response model for aircraft conceptual design studies, or more sophisticated climate models can be used. Linear methods calculate the time-varying temperature change from a set of emissions using simplified expressions derived from the results of complex global climate models. Linear models of varying complexity for aviation studies are applied in Refs. [53, 47, 68, 56, 55, 1, 32].

Weighted temperature change per year is integrated and divided by  $H$  to yield an average temperature response. Any unitless weighting function may be used, and multiple functions could be appropriate for this purpose, including simple windowing

and discounting.[65, 61, 18, 62, 4, 63, 51, 52, 32, 28] Window weighting functions include only impacts occurring within a specified timeframe, and an example of their application is the integrated radiative forcing metric GWP. Discounted metrics weight future impacts with an exponentially decaying function using either a constant or time-varying discount rate. Discount weighting functions are often applied in net present value economic metrics but can also be applied to physical metrics for many studies.[69] Conventional temporal weighting methods of windowing and discounting can be applied to an aircraft design climate metric, but other functions can also be used. To demonstrate this, the weighting function defined in equation (3.2) is presented.

$$w_r(t) = \begin{cases} 1 & t \leq H \\ \frac{1}{(1+r)^{t-H}} & H < t \leq t_{\max} \\ 0 & t > t_{\max} \end{cases} \quad (3.2)$$

This function assigns unity weighting to temperature change during the operating lifetime of the aircraft. An exponential devaluation rate is applied to temperature change occurring after the aircraft has ceased operation ( $t \geq H$ ). A rate of zero means that post-operation impacts are equally important compared with impacts during operating years; a rate of infinity means that post-operation impacts have no importance; a positive, finite rate means that temperature change each post-operation year is less important than the temperature change experienced the previous year. A maximum integration window defined by  $t_{\max}$  is also applied.

The function  $w_r(t)$  is designed so that long-term effects are included but do not dominate ATR. As described by the IPCC, the design of a reduced climate impact next generation commercial aircraft and other short-term climate abatement decisions involve “balancing the economic risks of rapid abatement now and the reshaping of the capital stock that could later be proven unnecessary, against the corresponding risks of delay.”[70] Designing an aircraft based on its climate impacts in 100 years is higher risk than designing an aircraft based on its impacts in the next 30 years because there is greater confidence that avoided climate change in the near-term will be highly valued. The relative importance of a unit of temperature change in

the far future is uncertain and unpredictable, and depends on future trajectories of technological growth, realized physical impacts, and mitigation and adaptation. In contrast, the value of short-term impacts are more certain. Short-term impacts are defined here by the window of approximately 30 years, which coincides with the operating lifetime of typical commercial aircraft. In equation (3.2), short-term impacts are weighted at unity, and long-term effects are weighted with importance that decays exponentially. Decaying weighting factors are delayed 30 years for two reasons. First, as previously mentioned, scenario uncertainty is more moderate during this period: emissions, technological change, and policy scenarios are more certain for the next generation. Secondly, scientific uncertainty is lower during this period: results in Ref. [4] indicate that during a 30 year window, predictions of temperature change reasonably agree not only within and across models, but also between emissions scenarios.

This weighting function and other monotonically decreasing functions are consistent with approaching climate change abatement as a task of sequential decision making under uncertainty.[70] The task is to design the next generation of commercial aircraft with cost effective climate impact reduction solutions so that in 30 years, climate change has not reached such high levels as to limit future options.[71] In the meantime, technology advancement and learning will continue. For the design of the following generation of aircraft, decisions will be better informed and aircraft climate mitigation will be reevaluated.

Selection of the weighting function involves a value judgment of the relative importance of short-lived and long-lived impacts. For the presented weighting function,  $w_r(t)$ , the devaluation rate is provided as a user-specified value judgment. Temperature change caused by short-lived impacts decays quickly after operation stops while long-lived species such as CO<sub>2</sub> cause a residual temperature change for many years post-operation. In aircraft design studies presented in Chapter 6, devaluation rates of 0% and 3% are considered. The integration window is taken to be very large compared with operating lifetime (if desired, shorter windows could also be used). A finite window is required for very low rates because a fraction of CO<sub>2</sub> emissions remain in the atmosphere for many thousands of years and therefore most models for CO<sub>2</sub>-induced temperature change do not decay to zero;[72] thus, for the case of

a zero devaluation rate, ATR converges to a constant times  $t_{\max}$ . With larger rates an infinite window is possible. For all examples herein,  $t_{\max}$  is taken to be 500 years, following the longest time horizon adopted by the IPCC for GWP calculations.[4] Average temperature responses calculated using this weighting function are denoted  $ATR_r$ , where  $r$  indicates the devaluation rate value, and operating lifetime is 30 years. Other devaluation rates, integration windows, and operating lifetimes can be applied; however, the same rates, windows, and lifetimes should be used when comparing two different design options.

The relationship between temperature change and ATR with the presented weighting function is shown graphically in Figure 3.2 based on the commercial aircraft fleet's emission rates in the year 2005, an operating lifetime of 30 years, and a devaluation rate of 3%. [1] Calculation of ATR for this emissions scenario represents the climate impacts that would result if every aircraft in the commercial fleet in 2005 was operated continuously until 2035 without fleet replacements or additions. This notional scenario illustrates the magnitudes and timescales of impacts of various aircraft emission components at current emissions rates. However, the ATR metric is designed for calculation of impacts for individual future aircraft configurations where the assumption of continuous emissions for 30 years is more realistic.

First, global mean temperature change is calculated assuming constant emission rates for the first 30 years and zero emissions thereafter, shown in Figure 3.2(a). Temperature change is computed using the linear climate model described in Chapter 5. Next, the weighting function is multiplied with temperature change, reducing impacts occurring after 30 years, shown in Figure 3.2(b). Then, the weighted temperature change is integrated to find the total lifetime impact in units of  $K \cdot yr$ , represented by the shaded area in Figure 3.2(c). Finally, this quantity is divided by the operating lifetime to find the average temperature response, represented by the bar height in Figure 3.2(d). The shaded regions in Figures 3.2(c) and 3.2(d) have equal area,  $H \cdot ATR$ . The notional year 2005 fleet  $ATR_{r=3\%}$  is approximately 35 mK.

To summarize, the average temperature response metric is proposed as a tool to condense the lifetime impacts of an aircraft into a single, meaningful quantity. The metric is designed for comparison of lifetime temperature change of different aircraft

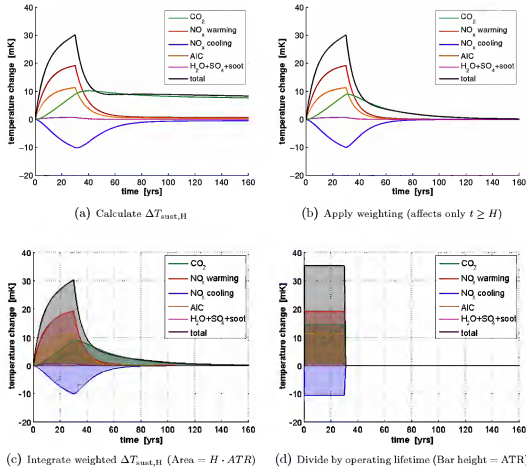


Figure 3.2: Graphical representation of the steps for calculating ATR. In this example,  $H = 30$  years,  $r = 3\%$ , and  $t_{\max} = 500$  years.

design and technology options and is not intended for use in aviation policy decisions. By using a linear climate model, ATR can be calculated simply and quickly. Parameters and expressions in the linear climate model can be continuously updated to reflect best available scientific knowledge of the effects of aircraft emissions. Additionally, by assessing the scientific uncertainty in the climate model, confidence in ATR calculations can be estimated, as discussed in Chapter 5.

### 3.3.3 Alternative Aircraft Design Metrics

Average temperature response is proposed as a climate metric for the application of aircraft design. However, other metrics could be developed to serve the same purpose. Each of the considered alternative metrics is based on the same aircraft emissions scenario of  $H$  years of constant emissions followed by zero emissions. The first is an integrated normalized radiative forcing metric, similar to global warming potential.[32] This metric, referred to as average radiative forcing response, is defined as in equation (3.1), where  $RF$  replaces  $\Delta T$ . The weighting function given in equation (3.2) is applied. The second alternative is an endpoint metric:  $\Delta T_{\text{sust}}(t = H)$  is the temperature change after  $H$  years of sustained emissions and is similar to global temperature potential.[32] Aircraft design study results in Ref. [73] demonstrate that comparisons of climate performance are essentially insensitive to choice of metric between the options of integrated  $\Delta T$ , integrated  $RF$ , and endpoint  $\Delta T$  for the specified emissions scenario. The differences in results with each of these metrics lies primarily in the weighting of short-lived and long-lived effects which can be adjusted within the ATR framework using weighting function parameters  $r$  and  $t_{\text{max}}$ .

# Chapter 4

## Aircraft Design and Analysis Tools

### 4.1 Introduction

To explore the design of future aircraft for reduced climate impacts, methods are needed to assess aircraft performance. Takeoff, climb, cruise, and landing performance are determined using the conceptual design software PASS, a flexible tool that enables the integration of new and updated methods. This chapter describes the cost methods used for economic performance estimation and an updated engine model.

### 4.2 Program for Aircraft Synthesis Studies

The design of new aircraft encompasses many disciplines including aerodynamics, structural design, stability and control, and economics. While the final, detailed design of a new commercial aircraft typically requires several years of work by thousands of engineers, an initial or conceptual design can be generated quickly using approximate methods and computational tools. The Program for Aircraft Synthesis Studies (PASS) is a conceptual design and performance estimation tool containing methods for each discipline as shown in Figure 4.1.[74] These methods rely on McDonnell Douglas empirical models and newly developed analyses that are described in detail in Ref. [75]. PASS has been validated and applied in many past aircraft design studies (e.g., Ref. [7]). When combined with an optimizer, PASS allows for rapid exploration

of the design space, including the tradeoffs between economic and environmental performance. A new climate impact module is developed for environmental analysis and is described in Chapter 5.



Figure 4.1: Structure of PASS, adapted from Ref. [7].

### 4.3 Operating Costs

For an aircraft to be economically competitive, its operating costs must be as low as possible. Total operating costs include both direct and indirect operating costs (DOC and IOC). Cost effectiveness is often measured by DOC, which includes fuel, crew, depreciation, insurance, and maintenance costs. The Air Transport Association of America (ATA) developed a set of equations for computing comparative DOC, and these methods are applied in PASS.[76] Crew costs are a function of aircraft weight and flight speed, with larger and slower aircraft having greater crew expenses. Fuel costs depend not only on mission fuel consumption, but also on the relative price

of fuel. Historically, fuel costs comprised approximately 20-25% of DOC, but during recent fuel price peaks, fuel cost fraction exceeded 50%. [75] Comparative depreciation and insurance costs scale primarily with airframe and engine purchase prices. Finally, maintenance costs are difficult to estimate and depend on configuration weight, flight hours, and purchase costs. IOC, on the other hand, includes other airline expenses such as ground and passenger handling, landing fees, cabin attendants, advertising, and administrative costs. IOC is estimated as an approximate function of aircraft weight, passenger capacity, and load factor based on McDonnel Douglas methods. [75] All expenses, such as fuel, labor, and airframe and engine purchase costs, are estimated in year 2010 US dollars.

## 4.4 Variable Bypass Ratio Engine Model

Most modern commercial aircraft use turbofan engines, which produce thrust by accelerating air through a ducted fan. A fraction of this air is also passed through the engine core, where fuel is combusted to drive the fan and compressor, and the remaining air bypasses the core. The ratio of fan bypass to core mass flows is known as bypass ratio. High bypass ratio engines produce thrust by applying a small acceleration to a large mass of air, and low bypass ratio engines apply a large acceleration to a small mass flow. Recently certified large commercial turbofan engines have bypass ratios of approximately 10, and higher bypass ratio engines are likely to be designed in the future. [77, 78] Bypass ratio and the related parameter fan pressure ratio are key engine design variables that impact fuel efficiency, weight, and drag.

Fan diameter is affected by both bypass ratio and fan pressure ratio. Fan pressure ratio is an engine design parameter related to the magnitude of the acceleration applied to air passing through the fan, with higher fan pressure ratios indicating larger accelerations. At fixed thrust, as bypass ratio is increased, fan diameter increases and fan pressure ratio decreases. The relationship between fan diameter, bypass ratio, and fan pressure ratio is illustrated in Figure 4.2 for an engine with approximately 100,000 pounds of static thrust from Ref. [10].

Increases in bypass ratio and reductions in fan pressure ratio lead to improvements

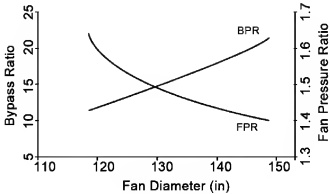


Figure 4.2: Relationship between fan diameter, fan pressure ratio, and bypass ratio for a turbofan engine.[10]

in propulsive efficiency, or the ratio of useful thrust power to the increment of kinetic power applied to the flow. Simple axial momentum theory by Froude shows that propulsive efficiency is inversely related to the magnitude of the acceleration through the fan.[79] This relationship is defined in equation (4.1), where  $V_0$  and  $V_e$  represent the incoming freestream and far field exhaust velocities, respectively.

$$\eta_p = \frac{2V_0}{V_0 + V_e} \quad (4.1)$$

The dependency of ideal propulsive efficiency on fan pressure ratio is shown in Figure 4.3.[11] These ideal propulsive efficiencies are based on axial induced momentum losses and do not account for viscous or swirl losses. As indicated by equation (4.1) and Figure 4.3, bypass ratio and fan pressure ratio have a powerful impact on the maximum efficiency of the fan system.

While higher bypass ratio engines benefit from improved propulsive efficiency, they are also penalized by greater weight and drag due to the large fan and nacelle.[10, 80] As fan diameter increases, a gearbox may be required to limit fan tip speeds and maintain efficient engine core performance, further increasing weight and mechanical complexity. Additionally, thrust lapse increases with bypass ratio.[81] This means that of two engines sized for the same sea level static thrust, the higher bypass ratio engine has less thrust available at high speed cruise conditions. As a result, a higher

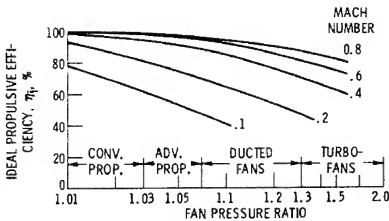


Figure 4.3: Ideal propulsive efficiency versus fan pressure ratio.[11]

bypass ratio engine may need to be oversized to meet cruise thrust requirements. On the other hand, jet exhaust noise decreases with increasing bypass ratio. Trends in drag, weight, efficiency, jet noise, and thrust lapse with varying engine fan diameter are shown in Figure 4.4.[10] Based on these competing performance trends, the optimal engine bypass ratio for a given application is a compromise of the needs for high efficiency and low weight and drag.

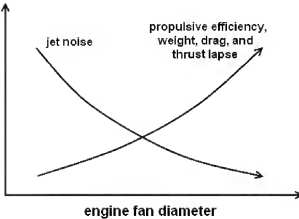


Figure 4.4: Effect of changing fan diameter on drag, weight, and propulsive efficiency, adapted from Ref. [10].

To achieve high propulsive efficiency without extreme weight and drag penalties,

unducted high bypass ratio propfan engines have been considered for application on large commercial aircraft. NASA funded the Advanced Turboprop Project in the 1980s to explore the benefits of unducted, highspeed aircraft engines.[82, 83, 84] This project included analyses, wind tunnel testing, and flight tests to demonstrate propfan performance. Traditional unducted turboprop engines are limited to maximum cruise speeds of Mach 0.65, with significant efficiency losses at higher speeds due to compressibility. Propfans, on the other hand, employ highly swept, very thin, small diameter propeller blades designed to operate at speeds of up to Mach 0.8 without significant compressibility losses.[82] A comparison of the relative fan diameters of traditional turboprops, propfans, and high bypass ratio turbofans is shown in Figure 4.5.[12]

#### 0.80 MACH NUMBER WIDE BODY AIRCRAFT

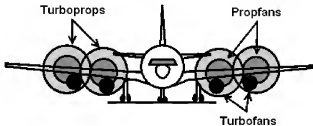


Figure 4.5: Comparison of fan sizes for turboprop, propfan, and turbofan engines (reproduced with permission of the American Institute of Aeronautics and Astronautics).[12]

The combination of high speeds and high efficiencies could enable significant fuel savings for aircraft driven by propfans. Configuration studies have predicted fuel burn savings of on the order of 15-30% relative to aircraft with comparable turbofan technology.[12, 85, 86, 87, 11] However, the Advanced Turboprop Project identified a number of propfan technical design challenges including noise, aerodynamic and structural installation issues, blade aeroelastic design, and gearbox design.[85, 86] For example, without a duct, the cabin interior and propfan blades must be designed carefully to limit interior and exterior noise to acceptable levels.[88] Recently, there

has been renewed interest by the engine manufacturers in propfan technology owing to volatile, high fuel prices, and work to resolve these issues continues (e.g., Ref. [89]).

To determine the optimal engine configuration for a particular aircraft application, engine performance, drag, weight, noise, and cost must be modeled as a function of bypass ratio. This section describes turbofan and propfan models appropriate for aircraft conceptual design.

#### 4.4.1 Engine Performance

Engine performance is characterized by specific fuel consumption and maximum available thrust at varying operating conditions. Performance is modeled by combining an engine cycle analysis with simple propeller theory. Cycle analysis computes the thermodynamic properties of the flow at each station in the engine based on user-specified design variables and component efficiencies following the methods presented in Refs. [21, 90]. This approach allows users to quantify the overall performance effects of changing design parameters such as bypass ratio. The result is a “rubber engine” that may be scaled up or down in size by adjusting engine mass flow. The same cycle analysis is applied for both turbofan and propfan engines, and differences between these configurations are modeled through engine design parameters and efficiencies.

Similar engine cores can be designed to drive ducted or unducted fans with different pressure ratios and numbers of rotors. Efficiency depends on these fan configuration design variables. Unducted fans employ either a single rotor or two counter-rotating propellers. Single rotor propfans benefit from reduced mechanical complexity, but these propellers leave rotational momentum in the propeller wake, leading to reduced efficiencies. Dual rotor propfans are designed for reduced swirl losses. Lastly, ducted turbofans are often designed with a rotor and stator to limit swirl losses and noise. Simple propeller theory is applied to estimate the efficiencies of different fan configurations, including ducted rotor-stators and unducted single and dual rotor fans, based on losses from drag and energy left in the wake. The combined cycle analysis and propeller theory model for turbofan and propfan performance is described in Appendix A.

This model is applied to estimate the overall performance of several engines with comparable levels of technology. Turbofans and propfans with different bypass ratios are examined. Each engine is driven by the same core with fixed high pressure compressor, burner, and turbine efficiencies based on 2010 technology levels; associated efficiencies are listed in Appendix A. Six engines in total are analyzed: three turbofans, two dual rotor propfans, and one single rotor propfan. The bypass ratios and fan pressure ratios of each of these engines are listed in Table 4.1. The bypass ratio 60 counter-rotating propfan has a maximum cruise power loading of approximately 50 shaft horsepower per square ft, representative of the highest NASA Advanced Turboprop Program power loadings.[91]. This bypass ratio provides a lower bound for propfan configurations in Chapter 6. Maximum available thrust at sea level and 35,000 ft is plotted versus Mach number in Figure 4.6. Higher bypass ratio engines experience greater thrust lapse, with less available thrust at high speed compared with lower bypass ratio engines. Figure 4.7 shows specific fuel consumption and overall efficiency versus throttle setting, illustrating the opportunity for improvements in fuel efficiency with high bypass ratio turbofans and propfans. Fuel efficiency benefits diminish with single rotor propfans partly due to swirl efficiency losses – however, these losses can be mitigated with optimized propulsion-airframe integration (e.g., Ref. [92]).

| Configuration        | Bypass Ratio | Fan Pressure Ratio | Fan Diameter [ft] |
|----------------------|--------------|--------------------|-------------------|
| Turbofan             | 8            | 1.79               | 5.5               |
| Turbofan             | 12           | 1.53               | 6.2               |
| Turbofan             | 20           | 1.31               | 7.6               |
| Dual Rotor Propfan   | 60           | 1.10               | 11.0              |
| Dual Rotor Propfan   | 85           | 1.08               | 12.8              |
| Single Rotor Propfan | 150          | 1.05               | 14.0              |

Table 4.1: Bypass ratio, fan pressure ratio, and diameter of engines with 25,000 pounds of sea level static thrust.

Predictions of available thrust and fuel consumption are compared with published values to determine engine model accuracy. Detailed engine performance information is commercially sensitive and often not openly available, limiting the amount of data

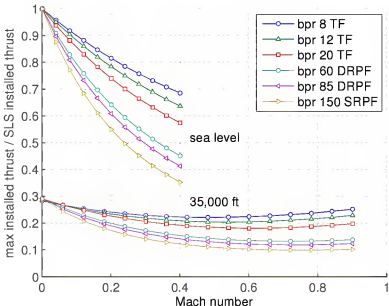


Figure 4.6: Maximum available thrust versus Mach number at varying altitude for turbofans and dual and single rotor propfans of varying bypass ratio.

available to validate this model. Figure 4.8 compares model predictions of available thrust and specific fuel consumption with performance estimates for a NASA study high bypass ratio geared turbofan.[13] Predictions of maximum available thrust and specific fuel consumption agree over a wide range of speeds and altitudes.

Fuel consumption estimates also concur with performance data published by NASA for a bypass ratio 7 turbofan and a highly loaded propfan at Mach 0.7 and 30,000 ft altitude.[87] Both the described model and the NASA reference predict specific fuel consumptions of  $0.43$  and  $0.55 \text{ hr}^{-1}$  at maximum throttle. These model results also correspond well to NASA estimates for specific fuel consumption of a bypass ratio 8 turbofan of approximately  $0.57 \text{ hr}^{-1}$  at Mach 0.8 and 30,000 ft altitude.[93] Furthermore, results generally follow predictions by engine manufacturers of fuel consumption savings on the order of 15% by propfans relative to advanced turbofans.[89]

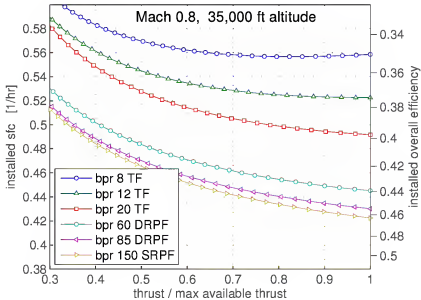


Figure 4.7: Installed specific fuel consumption and overall efficiency versus throttle setting for turbofans and propfans of varying bypass ratio.

#### 4.4.2 Engine Geometry

To estimate engine weight and drag, dimensions must be known. Section 4.4.1 and Appendix A describe a model for a rubberized, dimensionless engine. Once thrust is specified at a given operating condition, the engine can be sized, including determination of fan diameter and engine length.

Turbofan diffusers and fans are designed to achieve a specified fan capacity. The diffuser decelerates incoming air, and modern turbofan engines are generally designed with fan capacities corresponding to maximum fan face Mach numbers of approximately 0.66 at top of climb.[94] The top of climb condition for engines in this study is Mach 0.80, 35,000 ft altitude. Based on the specified fan face Mach number, the fan area and diameter,  $A_{fan}$  and  $D_{fan}$ , can be estimated from equations (4.2) and (4.3). In these equations, the subscript *toc* refers to top of climb conditions,  $T_{T2}$  and  $P_{T2}$  are fan face stagnation temperature and pressure,  $M_{fan}$  is the maximum fan face Mach number, and  $\xi$  is the fan hub-to-tip ratio. The function  $MFP$  is the mass flow

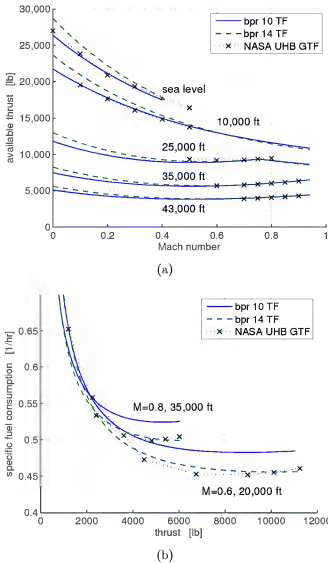


Figure 4.8: Comparison of available thrust and specific fuel consumption for high bypass ratio engines, from model predictions and a NASA study.[13]

function defined in Ref. [21].

$$A_{fan} = \frac{\dot{m}_{0,loc} \sqrt{T_{T2,loc}}}{P_{T2,loc} MFP(M_{fan})} \quad (4.2)$$

$$D_{fan} = 2 \sqrt{\frac{A_{fan}}{\pi (1 - \xi^2)}} \quad (4.3)$$

Unducted fans are sized similarly. Neglecting the effects of wake contraction, half of the total propeller velocity increment is experienced at the fan face,  $V_{fan} = 0.5(V_0 + V_e)$ .[79] Applying this relationship, the fan area and diameter may be found via equations (4.2) and (4.3). Estimates of fan diameters for engines with 25,000 pounds of sea level static thrust are listed in Table 4.1.

This analysis approximates shroud length for turbofans as 60% of total engine length and core nacelle diameter as 65% of the fan diameter.[75] Propfan core nacelle diameter is taken to be 35% of fan diameter based on Hamilton Standard methods for highly loaded propfans.[95] Engine length depends primarily on the thrust and power delivered to the fan and is independent of bypass ratio to first order. Assuming engine length,  $L_{eng}$ , scales with a power of sea level static thrust,  $T_{sls}$ , data from 36 high bypass ratio turbofan engines is used to derive equation (4.4) via a least squares data fit.[96, 97]

$$\frac{L_{eng}}{L_{ref}} = \left( \frac{T_{sls}}{T_{ref}} \right)^{0.337} \quad (4.4)$$

In equation (4.4), reference engine length,  $L_{ref}$ , is 121.2 inches and reference sea level static thrust,  $T_{ref}$ , is 25,000 pounds. A comparison of this engine length fit and turbofan data is shown in Figure 4.9. In this model, propfans and turbofans are driven by the same engine cores; therefore, equation (4.4) is also applied to propfans.

#### 4.4.3 Nacelle Parasite Drag

The total drag of a propulsion system installation can vary significantly with engine configuration. This section describes a conceptual design method for modeling this variation.[81, 75]

Parasite drag includes both skin friction and pressure drag. Skin friction drag is a function of the Reynolds number of the flow, wetted area, and the portions of the surface that have laminar or turbulent boundary layers. As bypass ratio rises, wetted area and hence skin friction drag increase. One method for reducing high bypass

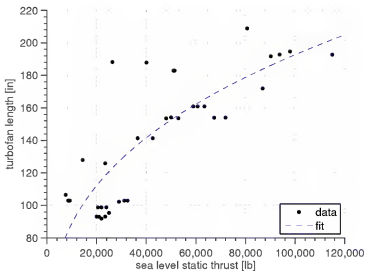


Figure 4.9: Engine length as a function of sea level static thrust.

ratio engine skin friction drag is to design the nacelles for natural laminar flow as seen on the Boeing 787.[98] Pressure drag exists because thicker boundary layers on the aft section of the nacelle prevent the cancellation of surface pressures. Pressure drag depends strongly on the shape of the nacelle and drops as the ratio of length to diameter, or fineness ratio, increases. As a result, high bypass ratio engines with larger fan diameters have higher pressure drag than low bypass ratio engines. Total parasite drag for the nacelle,  $D_{p,eng}$ , is computed by equation (4.5).

$$D_{p,eng} = q k c_f S_{wet,eng} \quad (4.5)$$

In this equation,  $q$  is the dynamic pressure,  $k$  is the body form factor,  $c_f$  is the skin friction coefficient, and  $S_{wet,eng}$  is the nacelle wetted area. The form factor adds an increment to skin friction drag to account for pressure drag and increased velocities on the surface. To compute  $k$ , the nacelle is modeled as a body of revolution with fineness ratio,  $FR$ , given by equation (4.6).[75] Recently designed bypass ratio 10-11

Trent 1000 and GEnx engines have fineness ratios of approximately 2.5.

$$FR \approx \frac{L_{eng} + D_{inlet}}{0.9 D_{inlet}} \quad (4.6)$$

Inlet diameter,  $D_{inlet}$ , is taken to be  $1.1D_{fan}$  for turbofans and  $0.35D_{fan}$  for propfans. Form factor is determined from fineness ratio using Figure 4.10. Data in the figure for fineness ratios of 4 to 10 is based on Ref. [81]. Form factors for lower fineness ratios are computed following Ref. [75] by relating drag to surface velocity increases on ellipsoids of varying fineness.

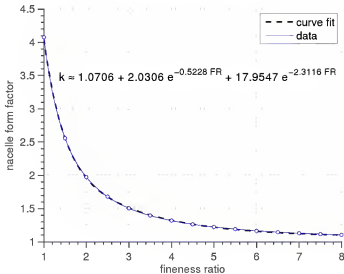


Figure 4.10: Nacelle form factor versus fineness ratio.

The skin friction coefficient is computed for the freestream Mach number and flow Reynolds number based on nacelle length and specified boundary layer transition location. Wetted area is computed based on nacelle dimensions in equation (4.7). For turbofans, the forward nacelle diameter is  $1.1D_{fan}$  and the aft diameter is  $0.65D_{fan}$ . For propfans, the nacelle diameter is a constant  $0.35D_{fan}$ .

$$S_{wet,eng} = \begin{cases} [0.6 \pi (1.1 D_{fan}) + 0.4 \pi (0.65 D_{fan})] L_{eng} & \text{for turbofans} \\ \pi (0.35 D_{fan}) L_{eng} & \text{for propfans} \end{cases} \quad (4.7)$$

Finally, total nacelle parasite drag may be computed for any operating condition via equation (4.5).

#### 4.4.4 Weight Estimation

An engine weight model is developed to capture the variation in propulsion system weight with changes to bypass ratio and thrust. Separate weight models are presented for ducted turbofan and unducted single and dual rotor propfan engines.

First, the dry engine weight of a ducted turbofan engine is considered. It is assumed that dry turbofan weight can be separated into contributions from the engine core and fan. The weight of the engine core is expected to depend primarily on thrust. In this model, core weight is a linear function of sea level static thrust and is independent of bypass ratio. Fan weight, on the other hand, depends on bypass ratio. If the fan was a solid disk, then based on volume considerations fan weight would scale with diameter squared. If the fan was a constant-chord propeller, then fan weight would scale linearly with diameter. In reality, the total volume of a typical engine fan is somewhere between a solid disk and a constant-chord propeller; therefore, fan weight is expected to scale with fan diameter to a power between one and two.

Data from 36 modern high bypass turbofans is used to fit equation (4.8) for dry turbofan weight,  $W_{tf,dry}$ .<sup>[96, 97]</sup> By minimizing the root-mean-square weight error, values for the constants are found. Reference engine weight,  $W_{ref}$ , is 10,000 pounds and reference engine diameter,  $D_{ref}$ , is 8 ft. A comparison of predicted and actual weight for the 36 current engines is shown in Figure 4.11. Two plots are shown because two independent parameters, sea level static thrust and fan diameter, are used in the engine weight fit. (Note: Several separate engines use fans with equal diameters, as indicated in Figure 4.11(b).)

$$\frac{W_{tf,dry}}{W_{ref}} = 0.098 \frac{T_{sls}}{W_{ref}} + 0.452 \left( \frac{D_{fan}}{D_{ref}} \right)^{1.68} \quad (4.8)$$

The propfan weight model is divided into core, fan, and gearbox weight elements, as given by equation (4.9). In this model, identical cores drive turbofans and propfans,

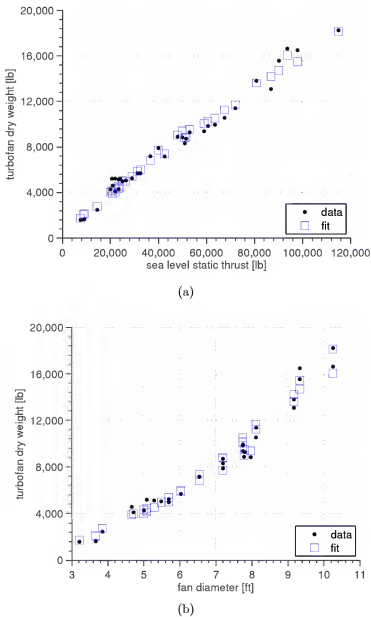


Figure 4.11: Variation in turbofan weight with sea level static thrust and fan diameter.

so the same core weight model is applied to both engine types. The fan weight model depends on fan diameter and disk loading and is based on a Hamilton Standard method.[99] Their method developed for single rotor configurations with 800 ft/sec

tip speed and includes the weight of the fan blades, pitch change mechanism, hub, deicing, and spinner. It is assumed that this method can be extended to dual rotation propellers by scaling the model by the number of rotors,  $N_{rot}$ . Lastly, gearbox weight is also based on a Hamilton Standard method.[95] Gearbox weight is proportional to maximum output torque, which for fans with fixed tip speed is directly related to the product of fan diameter and power to the fan,  $P_{sls}$ . In this equation, reference fan power,  $P_{ref}$ , is 5,000 horsepower, and  $D_{ref}$  and  $W_{ref}$  are defined as in equation (4.8). Gearbox weight also scales with the square root of gear ratio,  $GR$ , defined as the ratio of fan and low pressure turbine rotational rates. Gear ratio is computed assuming a maximum propfan tip speed of 800 ft/sec and a design low pressure turbine rotational rate of 800 rad/sec.[21]

$$W_{pf,dry} = W_{pf,core} + W_{pf,fan} + W_{pf,gearbox}$$

$$\frac{W_{pf,dry}}{W_{ref}} = 0.098 \frac{T_{sls}}{W_{ref}} + 0.059N_{rot} \left( \frac{P_{sls}}{P_{ref}} \right)^{0.3} \left( \frac{D_{fan}}{D_{ref}} \right)^{1.836} + 0.021 \frac{P_{sls}}{P_{ref}} \frac{D_{fan}}{D_{ref}} \sqrt{\frac{GR}{8}}$$
(4.9)

Turbofan and propfan weights are compared in Figure 4.12 for engines sized to produce 25,000 pounds of sea level static thrust. In the figure, turbofan bypass ratios range from 5 to 20, dual rotor propfans from 60 to 110, and single rotor propfans from 90 to 200. Dual rotor propfans are heavier than moderate bypass ratio turbofans due to their larger rotor diameters and the presence of a gearbox. However, propfans do offer a lighter weight alternative to very high bypass ratio turbofans. Because the turbofan weight model is based on existing conventional engines, there is no explicit modeling of the gearbox and/or the additional low pressure turbine stages that would be necessary for very large fans. Allowable fan tip speeds for turbofans are almost double those of propfans, and thus turbofans do not require as large of a gearbox as a propfans with equal rotor diameters. Nonetheless, weight is underestimated for turbofans with very large diameter rotors.

Finally, equations (4.8) and (4.9) estimate dry engine weight. Total propulsion system weight includes the nacelle and pylon, controls, lubrication, and fuel systems.

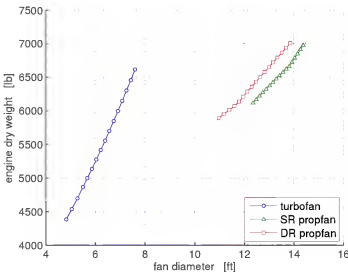


Figure 4.12: Turbofan and single and dual rotor propfan dry weight versus fan diameter for 25,000 sea level static thrust engines.

Turbofan propulsion system weight is approximately 60% greater than dry weight alone.[75] Propfan propulsion system weight is approximately 30% greater than dry weight alone.[95] The turbofan model is based on data for engines designed and certified over the last several decades, and the propfan model is based on late 1980s technology. For engines with entry-into-service of 2010 or later, lighter weight materials and improved design may enable weight reductions.

#### 4.4.5 Certification Noise

Newly certified aircraft are required to meet standards for maximum community noise during takeoff and landing. In addition, a growing number of airports have established individual noise restrictions, curfews, and charges.[100] To allow for operational flexibility and economic competitiveness, future aircraft will likely need to be quieter than today's aircraft. A large fraction of total noise during both takeoff and approach is produced by the engines.[7] This noise varies depending on bypass ratio and whether the fan is ducted or unducted. This section describes a model for estimating the certification noise of different engine configurations.

Current ICAO Chapter 4 regulations restrict noise measured at approach, flyover, and sideline conditions. Certification noise is computed using the methodology described in Ref. [75]. In this model, total noise at each condition is estimated based on measured noise at a specified distance from a bypass ratio 6 reference turbofan engine. This noise is scaled for an individual aircraft configuration based on the size and number of engines, engine throttle setting, and the distance between the aircraft and the regulated noise measurement location. At approach conditions, an estimate of airframe noise is added.[75] Increases in bypass ratio affect takeoff engine noise, resulting in lower jet noise but greater fan noise. Moderately high bypass ratio turbofans are expected to be quieter than current engines, and a number of studies predict noise savings for engines with bypass ratios of up to 15.[7, 101, 102] Analysis of ICAO certification data reveals an approximate reduction of 1.5 dB at sideline and 0.5 dB at flyover per unit increase in bypass ratio.[103] However, also included in this trend are improved acoustic technologies, including advanced duct liners. Following results published by Antoine, turbofan sideline and flyover noise are assumed to reduce by 0.7 dB and 0.5 dB, respectively, per unit increase in bypass ratio.[7] Additionally, the reference engine noise is reduced by 5 dB at all conditions to account for improved technology.[75]

Propfan engines lack a shroud to protect surroundings from fan noise. Meeting current Chapter 4 and future, more restrictive regulations poses a challenge for propfan aircraft. A recent workshop cites the general expectation from industry that propfan aircraft can meet Chapter 4 targets with a margin, but steeper climb and approach paths may be required to reduce noise exposure.[104, 105] In this research, the reference turbofan noise is shifted to match certification noise predictions based on scale model tests by Hoff et al.[106] Based on this data, counter-rotating propfan engines are approximately 0.5 dB quieter than the reference engine at each condition. Counter-rotating propfans are noisier than single rotor propfans due to rear rotor wake aerodynamic interactions and out-of-phase acoustic interactions.[107, 108] Single rotor engines are modeled to be 2.5 dB quieter than counter-rotating propfans

at each noise measurement condition. This estimate is based on single and dual rotor porpfan comparative noise measurements, demonstrating that single rotors are at least 2.5 dB quieter at each blade harmonic frequency.[108]

#### 4.4.6 Engine Maintenance and Acquisition Costs

Engine costs are incurred both initially for the purchase of the aircraft and during operation for maintenance. The availability of engine acquisition cost data is very limited, particularly for advanced high bypass ratio turbofans and propfans. Turbofan acquisition costs are estimated using the data in Ref. [109]. An empirical method relates cost to sea level static thrust per engine based on engines certified and produced prior to 1975. Because very high bypass ratio turbofans have large, heavy fans, this method is expected to underpredict acquisition costs for high bypass ratio engines. Pratt and Whitney and Hamilton Standard estimate the acquisition costs of a turbofan and propfan designed for the same application to be within 1% of one another.[93] Based on this finding, it is assumed that propfan acquisition costs can be computed with the turbofan cost model.

Turbofan maintenance costs are computed with the ATA direct operating costs method.[76] Maintenance costs include both labor and parts costs and are a function of flight time and sea level static thrust. Similar to acquisition costs, preliminary estimates of propfan maintenance costs yield rates that are within  $\pm 8\%$  of turbofan rates. This result is supported by a NASA study presenting comparable maintenance costs for advanced turbofan and propfan engines.[110] Therefore, propfan maintenance costs are assumed to scale similarly to turbofan costs.

# Chapter 5

## Linear Climate Model with Altitude Variation

### 5.1 Introduction

Climate impacts from aircraft operations can be estimated based on the quantity and location of released emissions and knowledge about the climate system. Emissions of CO<sub>2</sub>, H<sub>2</sub>O, NO<sub>x</sub>, soot, and sulfate particles each affect the climate system as described in Chapter 2. The first section of this chapter describes methods for quantifying an aircraft's total emissions based on estimate of aircraft and engine performance. The second part of this chapter presents a climate model that translates aircraft emissions into radiative forcing and temperature change. The limitations of this climate model and a method for quantifying uncertainty in impact estimates are also discussed.

Climate models range in sophistication from simple linear temperature response models to complex three-dimensional global climate models. Although linear models are less accurate than more complex models, they enable quick estimation of impacts and have been applied to several aviation emissions studies.[53, 47, 68, 56, 55, 1, 32] Linear climate models developed for aviation studies compute the impacts from emissions deposited directly into the upper troposphere and lower stratosphere, which can lead to different climate impacts compared with ground-based emissions from other sectors. These climate models greatly simplify the physics and chemistry of

aircraft induced climate change, and the analysis generated by these models captures only first order effects; however, their speed makes linear models appropriately suited for quantifying the various tradeoffs in aircraft conceptual design. The climate model developed for this study distinguishes itself from many other linear climate models through its inclusion of altitude variation for NO<sub>x</sub> and AIC radiative forcings.

## 5.2 Emissions

The first step in assessing the climate impacts of a particular aircraft is to construct a scenario of future emissions produced by that aircraft. This emissions trajectory is computed by assuming the aircraft flies its typical mission a specified number of times per year. Utilization rate,  $U(t)$ , refers to the number of missions flown in year, and emissions per flight,  $e_i$ , refers to the total quantity of species  $i$  released during the typical mission. Annual emissions of each species,  $E_i(t)$ , may be estimated with equation (5.1).

$$E_i(t) = e_i U(t) \quad (5.1)$$

Emissions per flight are related to fuel consumption through the emissions index (EI), or the mass ratio of emitted species to fuel burned, as shown in equation (5.2). The emissions index for each species  $i$  is assumed to be piecewise constant, with a value of  $EI_{i,j}$  during the  $j^{th}$  mission segment.

$$e_i = \sum_{mission} EI_{i,j} W_{fuel,j} \quad (5.2)$$

Thus, for a given aircraft utilization rate, overall emissions savings can be achieved via reductions in either fuel burn or emissions index. Mission fuel consumption during the  $j^{th}$  flight segment,  $W_{fuel,j}$ , is calculated using the aircraft and engine performance tools described in Chapter 4. Emissions index,  $EI_i$ , is a key parameter determining the overall mass of emissions. For many species, EI is a property of the fuel and cannot be changed; however,  $EI_{NO_x}$  is a performance parameter that can be adjusted via design.

### 5.2.1 Carbon Dioxide, Water Vapor, Soot, and Sulfate Emissions Indices

The EIs of  $\text{CO}_2$ ,  $\text{H}_2\text{O}$ , and  $\text{SO}_4$  are solely dependent on the composition of the fuel and taken to be constants.[3] Sulfate emissions index is derived from average fuel sulfur content and a 50% conversion factor of fuel sulfur into optically active sulfate, following the IPCC.[3] As noted in Chapter 2, soot emissions index can vary with engine operating condition, but because soot comprises a small fraction of total climate impacts (on the order of less than 5%, e.g., Ref. [29]), this factor can also be assumed constant without significant loss in accuracy for many studies of interest. These EIs are listed in Table 5.1. Because these emissions indices are constant, the summation given in equation (5.2) is simply the product of  $\text{EI}_i$  and total mission fuel consumption.

| Species              | Emissions Index                                     |
|----------------------|---|
| $\text{CO}_2$        | 3.16 $\frac{\text{kg CO}_2}{\text{kg fuel}}$        |
| $\text{H}_2\text{O}$ | 1.26 $\frac{\text{kg H}_2\text{O}}{\text{kg fuel}}$ |
| $\text{SO}_4$        | 2.0e-4 $\frac{\text{kg S}}{\text{kg fuel}}$         |
| soot                 | 4.0e-5 $\frac{\text{kg soot}}{\text{kg fuel}}$      |

Table 5.1: Emissions indices.[3]

### 5.2.2 Nitrogen Oxide Emissions Index

Unlike emissions indices for  $\text{CO}_2$  and other species,  $\text{NO}_x$  emissions index is not constant and varies with engine throttle setting, flight speed, and altitude. The variation in emissions index with operating condition and combustor design is complex to model analytically, but different empirical correlation methods exist to approximately describe the relationship between combustor parameters and  $\text{EI}_{\text{NO}_x}$ . P3-T3 methods model emissions index as a function of combustor inlet temperature and pressure, ambient conditions, and sometimes other combustor design parameters. The P3-T3 method is the industry standard for computing  $\text{NO}_x$  emissions and is very accurate:

applying a P3-T3 correlation to the combustor for which it was derived enables emissions index prediction at flight conditions to within 5-10%. [40, 46, 45, 3] However, P3-T3 correlations lose accuracy when applied more generally and are not appropriate for studying changes to combustor design. [39]

Fuel flow correlation methods are also used to model  $\text{NO}_x$  cruise emissions index based on ICAO landing and takeoff certification emissions measurements. [42, 41] These methods are less accurate than P3-T3 correlations but are useful in studies where combustor inlet temperature and pressure data is unavailable (e.g., Refs. [43, 44, 8, 45, 46]). In this research, combustor temperature and pressure are modeled directly as described in Chapter 4 and Appendix A, hence P3-T3 methods are preferred.

Lefebvre developed a  $\text{NO}_x$  emissions P3-T3 correlation based on the assumption that emissions index is proportional to the product of mean residence time in the combustion zone, chemical reaction rate, and mixing rate. [40] Residence time depends on combustor length and flow velocity,  $L$  and  $V$ . Reaction rate is a function of combustor temperature and pressure,  $T$  and  $P$ , with higher  $\text{NO}_x$  formation rates at higher temperatures and pressures. Mixing rate is assumed to be a function of the pressure drop through the combustor,  $\Delta P$ , but this emissions index dependence is often found to be very weak. [40] Lefebvre's model for emissions index is given in equation (5.3).

$$EI_{\text{NO}_x} \propto \text{residence time} \cdot \text{reaction rate} \cdot \text{mixing rate}$$

$$= A \cdot \frac{L}{V} \cdot P^m \exp(zT) \cdot \left(\frac{\Delta P}{P}\right)^n \quad (5.3)$$

Correlations of this form have been derived for several different combustors. [39, 111, 30, 112, 113] Values of constants  $A$ ,  $z$ ,  $m$ , and  $n$  are found through regression analysis of emissions data from extensive combustor rig or full scale engine tests and consideration of chemical timescales. [111] Most combustors demonstrate dependence on combustor inlet pressure to a power,  $m$ , between 0.4 to 0.6. [111] In many fixed design correlations, dependence on varying flow velocity and liner pressure drop are neglected, leaving dependence on combustor pressure and temperature only.

This research applies the  $EI_{NO_x}$  correlation shown in equation (5.4), developed for the dual annular combustor studied during NASA's Experimental Clean Combustor Program.[113] This correlation is expected to approximately model the performance of the GE90-85B dual annular combustor, which is representative of modern high bypass ratio, high overall pressure ratio turbofan performance.[111]

$$EI_{NO_x} = 0.0986 \left( \frac{P_{T3}}{101325} \right)^{0.4} \exp \left( \frac{T_{T3}}{194.4} - \frac{H_0}{53.2} \right) \quad (5.4)$$

In the above equation, pressure is measured in Pascals, temperature in Kelvin, and specific humidity,  $H_0$ , in grams of water per kilogram of dry air. Following Baughcum et al., specific humidity is calculated as a function of altitude assuming 60% relative humidity.[43] This emissions correlation is also consistent with the IPCC P3-T3 method, which suggests relating sea level static and cruise emissions indices at the same  $T_{T3}$  by scaling with  $P_{T3}^{0.4}$  and correcting for differences in humidity.[8, 45, 3]

It should be noted that the correlation in equation (5.4) was derived for a dual annular combustor with lower core temperatures and pressures than those observed on newly certified engines with overall pressure ratios of 50 and higher.[96] This reduces the accuracy of emissions index predictions; however, correlations for newer engines are proprietary and not publicly available. Emission rates of more advanced low  $NO_x$  combustors are modeled by applying a scaling factor to equation (5.4), which will be described in technology studies in Chapter 6.

Figure 5.1 shows emissions index predictions for a bypass ratio 8 turbofan with a sea level static overall pressure ratio of 41. Emissions index is plotted versus throttle setting for both sea level static and cruise conditions. This engine meets ICAO CAEP6 landing and takeoff emissions standards due to its relatively low fuel consumption despite having very high full throttle emissions indices. At cruise, engine core temperatures and therefore emissions index decrease with reduced thrust setting and cruise speed. Emissions index is primarily a function of engine core design, and therefore engines with different bypass ratios but the similar cores exhibit nearly identical variation in EI with throttle.

The total mass of  $NO_x$  emissions for a single mission is computed via equation (5.2)

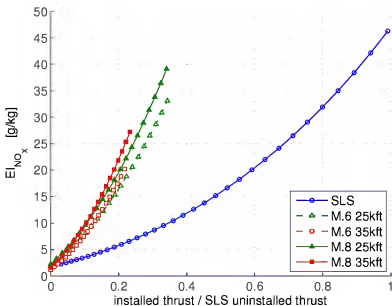


Figure 5.1: Cruise and sea level static  $\text{NO}_x$  emissions index for a sea level static overall pressure ratio 41 turbofan engine predicted by equation (5.4).

as the sum of emissions during taxi, takeoff, climb, cruise, and approach. Performance and emissions index for flight phases below 3,000 ft are based on the simulated landing and takeoff cycle applied by ICAO for emissions certification. Table 5.2 lists the ICAO-specified throttle settings and mode times for takeoff, climb out, approach and taxi and idle. Fuel burn and emissions index for these flight phases are calculated with the engine model and equation (5.4). Enroute climb emissions are approximated as the product of climb fuel and the emissions index at 15,000 ft altitude, Mach 0.5, and 85% throttle setting. Finally, cruise emissions index is taken as the average of EI<sub>s</sub> at the beginning and end of cruise based on altitude, speed, and required thrust setting.

### 5.3 Radiative Forcing

As previously noted, radiative forcing (RF) quantifies the change in net irradiance at the tropopause due to a perturbation, for instance aircraft emissions. This forcing

| Mode          | Time in Mode [mins] | Thrust Setting |
|---------------|---------------------|----------------|
| Takeoff       | 0.7                 | 100%           |
| Climb out     | 2.2                 | 85%            |
| Approach      | 4.0                 | 30%            |
| Taxi and Idle | 26.0                | 7%             |

Table 5.2: ICAO emissions certification simulated landing and takeoff cycle.[3]

measures the magnitude of a climate impact and is linearly related to the change in global mean equilibrium surface temperature. Radiative forcing causes a climate system response, which may include changes in surface temperature, precipitation, extreme weather events, and other climate properties.[6] Positive radiative forcing induces warming, and negative forcing causes cooling.

This section provides methods for computing time-varying radiative forcing as a function of altitude and mass of aircraft emissions. Different models are required for long-lived gases, short-lived pollutants, and aviation induced cloudiness. The parameters used in this model are based on current best estimates, and many of these parameters are associated with large uncertainty. Probability distributions for each parameter are listed, and a method for aggregating climate model uncertainty is discussed later in this chapter.

### 5.3.1 Altitude Variation

Radiatively active aircraft emissions differ from ground source emissions because they are deposited directly into the upper troposphere and lower stratosphere. In particular, the magnitude of effects from  $\text{NO}_x$  emissions and aviation induced cloudiness vary significantly depending on emissions altitude. To account for this variation, altitude-dependent forcing factors are developed.  $\text{NO}_x$  forcing factors are unitless parameters that represent the radiative forcing per emission at a particular altitude,  $h$ , normalized by fleetwide average radiative forcing per  $\text{NO}_x$  emissions. Similarly, AIC forcing factors are defined as the RF per distance flown at an altitude,  $h$ , normalized by fleetwide average AIC forcing per distance flown. These functions,  $s_i(h)$ , are based on data from perturbational aircraft emissions studies by Kohler et al. and Radel and

Shine for NO<sub>x</sub> forcing per emission and AIC forcing per distance flown as function of altitude.[14, 15] This data is normalized by the distance-weighted average RF per emission to define  $s_i(h)$ , shown in equations (5.5) and (5.6).

$$s_i(h) = \frac{\frac{RF_i}{E_{NO_x}}(h)}{\int_0^\infty \frac{RF_i}{E_{NO_x}}(h) l(h) dh} \quad \text{for } i = \text{CH}_4, \text{O}_{3L}, \text{O}_{3S} \quad (5.5)$$

$$s_{\text{AIC}}(h) = \frac{\frac{RF_{\text{cont}}}{L}(h)}{\int_0^\infty \frac{RF_{\text{cont}}}{L}(h) l(h) dh} \quad (5.6)$$

Because NO<sub>x</sub> impacts include both cooling effects from methane and long-lived ozone (O<sub>3L</sub>) and warming effects from short-lived ozone (O<sub>3S</sub>), multiple forcing functions are specified. Also, cloud impact altitude sensitivity data was published for contrails only.[15] However, contrail-cirrus clouds form from aging contrails (although soot cirrus clouds do not), and the radiative properties of contrail-cirrus are currently estimated to be similar to those of linear contrails.[22] Therefore, contrail forcing factors are extended to AIC radiative forcing, which includes effects from both contrails and cirrus clouds. The function  $l(h)$  is the ratio of the distance flown by the commercial fleet at altitude  $h$  to the total distance flown, based on the AERO2k inventory.[44, 14, 15] It should be noted that  $\frac{RF_i}{E_{NO_x}}(h)$  data is not available for  $h < 16,500$  ft and  $l(h)$  is nonzero in this range. To compute the denominator of equation (5.5),  $\frac{RF_i}{E_{NO_x}}(h < 16,500 \text{ ft})$  is assumed constant and equal to  $\frac{RF_i}{E_{NO_x}}(h = 16,500 \text{ ft})$ . This assumption has a small effect on the magnitude of forcing factors – a shift of 10% in  $\frac{RF_{O_{3S}}}{E_{NO_x}}(h < 16,500 \text{ ft})$  causes a change in  $s_{O_{3S}}$  of less than 1%. This is because forcing factors are comparatively low at these altitudes and a small fraction of distance is flown below 16,500 ft. Forcing factors for AIC and NO<sub>x</sub>-induced methane, long-lived ozone, and short-lived ozone are plotted versus altitude in Figure 5.2.

In addition to NO<sub>x</sub> and AIC impacts, direct water vapor effects also vary with

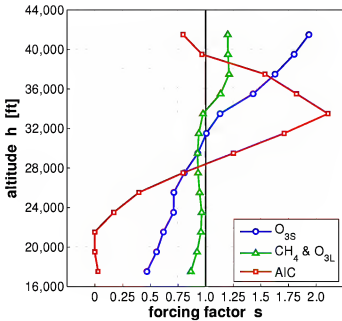


Figure 5.2: Radiative forcing factor data for  $NO_x$  impacts and aviation induced cloudiness, based on results from Refs. [14] and [15].

emission altitude. In the range of altitudes subsonic aircraft typically cruise (30,000-40,000 ft), nearly all water vapor is emitted into the troposphere or lowermost stratosphere where it has a very short residence time determined by the hydrological cycle and a weak impact on climate.[3] However, at higher altitudes, a greater quantity of emissions are released into the dry stratosphere, where water vapor has a longer residence time and therefore a more significant impact. At altitudes of approximately 60,000 ft, water vapor emissions have potent climate impacts, causing concern for a future supersonic aircraft fleet.[3] A study of subsonic aircraft altitude shifts ranging from -6000 ft to +2000 ft shows trend of increasing  $H_2O$  forcing with increasing altitude.[114] However, because the net impacts of  $H_2O$  are small over the range of subsonic altitudes compared with  $CO_2$ ,  $NO_x$ , and AIC impacts, this variation can be neglected.

### 5.3.2 Carbon Dioxide

Carbon dioxide is a well-mixed greenhouse gas with a long lifetime relative to chemical processes in the atmosphere. Because of this, aviation CO<sub>2</sub> impacts do not vary with altitude can be treated in the same manner as all other anthropogenic CO<sub>2</sub> sources. The IPCC estimates the radiative forcing caused by small perturbational emissions of CO<sub>2</sub> with equations (5.7) and (5.8).<sup>[4]</sup> This linear model is based on the assumption of constant background CO<sub>2</sub> concentrations of 378 parts per million by volume (ppmv). This is an unlikely trajectory in the near-term, and the impact of this scenario uncertainty is addressed later.

$$RF_{CO_2}(t) = \int_0^t G_{CO_2}(t-\tau) E_{CO_2}(\tau) d\tau \quad (5.7)$$

$$G_{CO_2}(t) = A_{CO_2} \left[ 1 + \sum_{j=1}^3 \alpha_{cj} \left( \exp \left( \frac{-t}{\tau_{cj}} \right) - 1 \right) \right] \quad (5.8)$$

In these equations, the expression  $G_{CO_2}(t)$  represents the decay of radiative forcing caused by a pulse emission of CO<sub>2</sub>, measured in W/m<sup>2</sup> per kg CO<sub>2</sub>. The bracketed portion of equation (5.8) describes the fraction of CO<sub>2</sub> emitted at  $t = 0$  that remains in the atmosphere at time  $t$ .<sup>[19]</sup> Best estimates for the values of the parameters  $A_{CO_2}$ ,  $\alpha_{cj}$ , and  $\tau_{cj}$  are listed in Table 5.3. Each parameter has a normal probability distribution with a 90% likelihood that the value is within 15% of its best estimate. This assumption is derived from the IPCC statement that calculation of integrated RF using this CO<sub>2</sub> model yields a total uncertainty of 15%. Thus, the uncertainty of individual parameters is overestimated.

### 5.3.3 Methane and Long-Lived Ozone

NO<sub>x</sub> emissions affect climate through ozone production and destruction and methane destruction. Ozone modeling must account for both short-term production (O<sub>3S</sub>) and long-term destruction (O<sub>3L</sub>) processes. First, the long-term, cooling forcings caused by methane destruction and ozone destruction are modeled. Response functions,  $G_i$ , are derived for the radiative forcing from methane and long-term ozone destruction

| CO <sub>2</sub> Parameter | Best Estimate  | Distribution | 90% Likelihood Range                             |
|---------------------------|--|--------------|--|
| $A_{\text{CO}_2}$         | $1.80 \times 10^{-15} \frac{\text{W/m}^2}{\text{kg CO}_2}$ | normal       | $\{1.53 \times 10^{-15}, 2.07 \times 10^{-15}\}$ |
| $\alpha_{c1}$             | 0.259  | normal       | {0.220, 0.298}                                   |
| $\alpha_{c2}$             | 0.338  | normal       | {0.287, 0.389}                                   |
| $\alpha_{c3}$             | 0.186  | normal       | {0.158, 0.214}                                   |
| $\tau_{c1}$               | 172.9 yrs  | lognormal    | {150, 199}                                       |
| $\tau_{c2}$               | 18.51 yrs  | lognormal    | {16.1, 21.3}                                     |
| $\tau_{c3}$               | 1.186 yrs  | lognormal    | {1.03, 1.36}                                     |

Table 5.3: CO<sub>2</sub> parameter values and distributions from §2.10.2 of the IPCC Fourth Assessment Report.[4]

caused by a pulse emission of NO<sub>x</sub>. These response functions are shown in equation (5.9).

$$G_i(t) = A_i \exp\left(\frac{-t}{\tau_{\text{CH}_4}}\right) \quad \text{for } i = \text{CH}_4, \text{O}_{3\text{L}} \quad (5.9)$$

Following the method of Marais et al., values for the methane and long-term ozone radiative efficiencies,  $A_{\text{CH}_4}$  and  $A_{\text{O}_{3\text{L}}}$ , are calculated.[55] Integrated long-term forcing is based on averaged results of Stevenson, Wild, and Derwent in Table 4 of Ref. [115]. Best estimates and probability distributions for the values of  $A_{\text{CH}_4}$ ,  $A_{\text{O}_{3\text{L}}}$ , and the adjustment time of methane,  $\tau_{\text{CH}_4}$ , are given in Table 5.4.

The time-varying radiative forcing due to arbitrary emissions functions can then be computed using the response functions,  $G_i$ . These response functions are derived from fleetwide emissions and altitudes. By applying height-dependent forcing factors described in section 5.3.1, radiative forcings are computed as altitude-specific values with equation (5.10).

$$RF_i(t, h) = s_i(h) \int_0^t G_i(t - \tau) E_{\text{NO}_x}(\tau) d\tau \quad \text{for } i = \text{CH}_4, \text{O}_{3\text{L}} \quad (5.10)$$

### 5.3.4 Short-Lived Species

Several aviation emissions have lifetimes much shorter than a year. Short-lived species include water vapor, short-lived ozone, soot, and sulfate aerosols. These species cause

| NO <sub>x</sub> Parameter  | Best Estimate  | Distribution | 90% Likelihood Range                                   |
|----------------------------|--|--------------|--|
| $A_{\text{CH}_4}$          | $-5.16 \times 10^{-13} \frac{\text{W/m}^2}{\text{kg NO}_x}$ [55] | lognormal    | $\{-8.60 \times 10^{-14}, -3.10 \times 10^{-12}\}$ [1] |
| $A_{\text{O}_{3\text{L}}}$ | $-1.21 \times 10^{-13} \frac{\text{W/m}^2}{\text{kg NO}_x}$ [55] | lognormal    | $\{-3.86 \times 10^{-14}, -3.78 \times 10^{-13}\}$ [1] |
| $\tau_{\text{CH}_4}$       | 12.0 yrs [4] <sup>a</sup>  | normal       | {10.2, 13.8} [4] <sup>a</sup>                          |

a IPCC 2007, WG1, §7.4.5.2.1

Table 5.4: Long-term NO<sub>x</sub> parameter values and distributions.

radiative forcing only for a short time after emissions. For these species, radiative forcing is assumed to be directly proportional to the radiative forcing per emission for a reference year based on IPCC and subsequent studies.[3, 29]

$$RF_i(t, h) = s_i(h) \left( \frac{RF_{\text{ref}}}{E_{\text{ref}}} \right)_i E_i(t) \quad \text{for } i = \text{H}_2\text{O}, \text{NO}_x\text{-O}_{3\text{S}}, \text{soot}, \text{SO}_4 \quad (5.11)$$

Forcing factors are unity for all short-lived species except short-term ozone, whose forcing factors are shown in Figure 5.2. Probability distributions for reference forcing per emissions are listed in Table 5.5. Following Lee et al., NO<sub>x</sub>-induced radiative forcing coefficients ( $A_{\text{CH}_4}$ ,  $A_{\text{O}_{3\text{L}}}$ , and  $\left( \frac{RF_{\text{ref}}}{E_{\text{ref}}} \right)_{\text{O}_{3\text{S}}}$ ) are 50% correlated.[1] All other uncertain climate model parameters are independent.

| Short Lifetime Parameter   | Best Estimate  | Distribution | 90% Likelihood Range                                   |
|--|--|--------------|--|
| $\left( \frac{RF_{\text{ref}}}{E_{\text{ref}}} \right)_{\text{H}_2\text{O}}$   | $7.43 \times 10^{-15} \frac{\text{W/m}^2}{\text{kg H}_2\text{O}}$ [3, 1] | lognormal    | $\{1.03 \times 10^{-15}, 5.38 \times 10^{-14}\}$ [1]   |
| $\left( \frac{RF_{\text{ref}}}{E_{\text{ref}}} \right)_{\text{O}_{3\text{S}}}$ | $1.01 \times 10^{-11} \frac{\text{W/m}^2}{\text{kg NO}_x}$ [29]          | lognormal    | $\{3.24 \times 10^{-12}, 3.17 \times 10^{-11}\}$ [1]   |
| $\left( \frac{RF_{\text{ref}}}{E_{\text{ref}}} \right)_{\text{SO}_4}$          | $-1.0 \times 10^{-10} \frac{\text{W/m}^2}{\text{kg SO}_4}$ [3, 1]        | lognormal    | $\{-1.65 \times 10^{-11}, -6.10 \times 10^{-10}\}$ [1] |
| $\left( \frac{RF_{\text{ref}}}{E_{\text{ref}}} \right)_{\text{soot}}$          | $5.0 \times 10^{-10} \frac{\text{W/m}^2}{\text{kg soot}}$ [3, 1]         | lognormal    | $\{8.23 \times 10^{-11}, 3.04 \times 10^{-9}\}$ [1]    |
| $\left( \frac{RF_{\text{ref}}}{E_{\text{ref}}} \right)_{\text{AIC}}$           | $2.21 \times 10^{-12} \frac{\text{W/m}^2}{\text{nm}}$ [116]              | lognormal    | $\{8.39 \times 10^{-13}, 5.82 \times 10^{-12}\}$ [1]   |

Table 5.5: H<sub>2</sub>O, O<sub>3S</sub>, SO<sub>4</sub>, soot, and AIC parameter values and distributions.

### 5.3.5 Aviation Induced Cloudiness

Aviation induced cloudiness (AIC) refers to the combination of contrails and aviation induced cirrus clouds, which are also short-lived effects. The linear model of radiative forcing due to contrails and cirrus relies on the basic assumption by Stordal et al. that a change in the cloud cover over an area is proportional to a change in aircraft flight distance and the further assumption that forcing scales linearly with cloud coverage.[116] Thus, AIC radiative forcing is assumed to be directly proportional to a reference forcing per distance traveled. Forcing factors are applied to yield altitude-specific forcing based on fleetwide average data.

$$RF_{\text{AIC}}(t, h) = s_{\text{AIC}}(h) \left( \frac{RF_{\text{ref}}}{L_{\text{ref}}} \right)_{\text{AIC}} L(t) \quad (5.12)$$

In equation (5.12),  $L$  is the distance flown per year and  $RF_{\text{ref}}$  and  $L_{\text{ref}}$  are the radiative forcing and total distance flown for a reference year, listed in Table 5.5.[116] AIC forcing factors,  $s_{\text{AIC}}$ , are plotted in Figure 5.2. This model does not account for the variation in cloud impacts with aircraft size or water vapor and particle emission rates, leading to large uncertainty ranges for individual configurations. AIC radiative forcing also varies with time of day, season, and latitude. Improved understanding and incorporation of these sensitivities is the subject of future work.

## 5.4 Temperature Change

Before computing temperature change, radiative forcing for each species is normalized. Normalized radiative forcing,  $RF^*$ , is adjusted based on species' efficacy,  $f_i$ , and is divided by the RF that would result from a doubling of  $\text{CO}_2$ , shown in equation (5.13).

$$RF_i^*(t, h) = f_i \frac{RF_i(t, h)}{RF_{2x\text{CO}_2}} \quad (5.13)$$

for  $i = \text{CO}_2, \text{CH}_4, \text{O}_{3L}, \text{O}_{3S}, \text{H}_2\text{O}, \text{soot}, \text{SO}_4, \text{AIC}$

Efficacy is a unitless parameter that compares the change in surface temperature from equal forcings of species  $i$  and  $\text{CO}_2$ .[4] By definition, the efficacy of  $\text{CO}_2$  is one. Values for  $RF_{2\text{CO}_2}$  and efficacies are listed in Table 5.6. Uncertainty bounds given by Grewe and Stenke for  $f_{\text{H}_2\text{O}}$ ,  $f_{\text{AIC}}$   $f_{\text{CH}_4}$  and  $f_{\text{O}_3}$  are assumed to correspond to 66% likelihood ranges.[56] Additionally, the IPCC Fourth Assessment Report states that there is not a consensus on the best estimate or distribution of  $f_{\text{soot}}$ . Based on studies discussed in §2.8.5.6 of that reference, a best estimate of 0.7 is assumed with a 66% likelihood that the parameter is within a factor of 2 of this estimate.[4] Once normalized radiative forcings have been computed for each species, they are summed and applied to a climate impulse response function to find a time-varying global mean temperature change via equation (5.14).

$$\Delta T(t) = \int_0^t G_T(t - \tau) \left( \sum_i RF_i^*(\tau) \right) d\tau \quad (5.14)$$

for  $i = \text{CO}_2, \text{CH}_4, \text{O}_{3\text{L}}, \text{O}_{3\text{S}}, \text{H}_2\text{O}, \text{soot}, \text{SO}_4, \text{AIC}$

Several climate impulse response functions,  $G_T$ , have been developed for this purpose by fitting results from global climate models (GCMs).[16, 17, 18, 19] The response functions described by Boucher and Reddy and Joos et al. are similar, each with short and long time constants of approximately 10 and 400 years.[17, 19] The short time constant can be crudely interpreted as the response of the ocean-mixed layer, and the long time constant as the response of the deep ocean, although this interpretation is tentative since the model is purely based on a data fit of GCM calculations.[32] The response model presented by Shine et al. adopts a single time constant of 10.7 years corresponding to the thermal inertia of the mixed ocean layer. The least recently developed impulse response function, given by Hasselmann et al., has a single time constant of 36.8 years, and differs significantly from the other three functions in its more pronounced thermal inertia.[16] A comparison of these four functions, each scaled to yield a temperature response of 1 K after 100 years of sustained unity  $RF^*$ , is plotted in Figure 5.3.

The two-mode impulse response function developed by Boucher and Reddy and

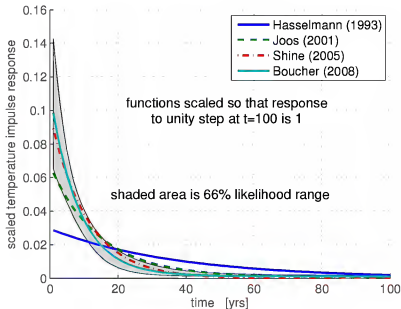


Figure 5.3: Scaled temperature impulse response functions from Hasselmann et al., Joos et al., Shine et al., and Boucher and Reddy.[16, 17, 18, 19]

given in equation (5.15) is applied in this model.[19] The climate sensitivity parameter,  $S$ , is the steady-state temperature change that would result from a constant annual forcing of  $RF_{2xCO_2}$ . Probability distributions of the parameters  $\alpha_t$ ,  $\tau_{t1}$ , and  $\tau_{t2}$  are approximated based on the four impulse response functions plotted in Figure 5.3, with emphasis on the more recent models of Joos et al., Shine et al., and Boucher and Reddy. The estimated two-thirds likelihood range for  $G_T(t)$  is shown in Figure 5.3, and parameter distributions are listed in Table 5.6.

$$G_T(t) = S \left[ \frac{\alpha_t}{\tau_{t1}} \exp \left( \frac{-t}{\tau_{t1}} \right) + \frac{1 - \alpha_t}{\tau_{t2}} \exp \left( \frac{-t}{\tau_{t2}} \right) \right] \quad (5.15)$$

## 5.5 Limitations of the Climate Model

Linear climate models offer many advantages compared with more complex models, including lower computational costs and increased transparency. The IPCC has noted

| Temperature Model Parameter | Best Estimate                        | Distribution | 90% Likelihood Range           |
|-----------------------------|--------------------------------------|--------------|--------------------------------|
| $f_{\text{CH}_4}$           | 1.18 [68]                            | normal       | {0.977, 1.38} [56]             |
| $f_{\text{H}_2\text{O}}$    | 1.14 [68]                            | normal       | {0.550, 1.73} [56]             |
| $f_{\text{O}_3}$            | 1.37 [68]                            | normal       | {0.662, 2.08} [56]             |
| $f_{\text{SO}_4}$           | 0.9 [4] <sup>a</sup>                 | normal       | {0.412, 1.39} [4] <sup>a</sup> |
| $f_{\text{soot}}$           | 0.7 [4] <sup>a</sup>                 | lognormal    | {0.212, 2.31} [4] <sup>a</sup> |
| $f_{\text{AIC}}$            | 0.59 [68]                            | normal       | {0.488, 0.692} [56]            |
| $RF_{2x\text{CO}_2}$        | 3.70 $\text{W/m}^2$ [4] <sup>b</sup> | normal       | {3.33, 4.07} [4] <sup>b</sup>  |
| $S$                         | 3.0 K [4] <sup>c</sup>               | lognormal    | {1.49, 6.03} [4] <sup>c</sup>  |
| $\alpha_t$                  | 0.595 [19]                           | lognormal    | {0.397, 0.893} [see text]      |
| $\tau_{t1}$                 | 8.4 yrs [19]                         | lognormal    | {4.2, 16.8} [see text]         |
| $\tau_{t2}$                 | 409.5 yrs [19]                       | lognormal    | {205, 819} [see text]          |

a IPCC 2007, WG1, §2.8.5.5 and §2.8.5.6

b IPCC 2007, WG1, §2.3.1

c IPCC 2007, WG1, Box 10.2

Table 5.6: Temperature change model parameter values and distributions.

these benefits and applies rapid, low cost climate response calculations based on parameterizations of global climate models.[4, 1] However, accompanying these benefits are several limitations.

The temperature change computed in this model is based on a global mean response to radiative forcings that can be produced either globally or regionally.  $\text{CO}_2$  has a long lifetime, allowing the gas to mix throughout the atmosphere so that radiative forcing is independent from emission location. Shorter-lived perturbations, such as ozone production from  $\text{NO}_x$  emissions, cause radiative forcing only near flight routes. Thus, radiative forcings due to  $\text{O}_3$  production and aviation induced cloudiness are greatest in the northern mid-latitudes where aircraft traffic is most dense.[3] As a result, a scenario of net zero forcing may induce strong regional positive and negative temperature responses.[22] This study does not consider varying regional

impacts from aircraft emissions and instead focuses on the climate response averaged over the Earth's surface.

As noted above, models for radiative forcing from all emissions except CO<sub>2</sub>, which has a very long atmospheric lifetime, are dependent on the assumed temporal and geographical distribution of emissions. The RF computed in this model is not the forcing of one single aircraft, on a single mission, at a single time and location; rather it is the forcing caused by a fleet of many aircraft of a single type, operated continuously and globally. The models used here are based on average impacts from fleetwide routing in a single year within the last decade. This routing is concentrated largely in the northern hemisphere mid-latitudes. These models therefore quantify the average forcing caused by emissions spatially and temporally distributed according to routing similar to current traffic. Assumptions about flight timing are particularly important for contrail impacts, which can vary both seasonally and diurnally.[35] If the route distribution for a particular aircraft fleet differs significantly from current routing, then estimates of model parameter values become less accurate.

This linear climate model does not capture many of the sensitivities that are included in comprehensive assessments by global climate models. For instance, emissions from non-aviation sources may alter climate parameters.[1] Also, the effects of some aviation emissions are chemically coupled but are assumed to be independent in this model, such as NO<sub>x</sub> and SO<sub>x</sub>, which are interdependent through OH chemistry.[22] And as noted by Wuebbles et al., the quality of a simple parameterization is limited by the accuracy of the global model upon which it is based.[51] This model adopts the most recent, established methods of this type for computing radiative forcing and temperature change. However, as climate knowledge is refined in the future, this model can be updated to incorporate best available information.

CO<sub>2</sub> radiative forcing is calculated with the carbon cycle model of Boucher and Reddy which was applied by the IPCC for computing global warming potentials. This model assumes constant background CO<sub>2</sub> concentrations of 378 ppmv, a likely underestimate of actual near-term concentrations. As a result, the impacts of CO<sub>2</sub> emissions are overvalued by an amount that varies depending on the chosen metric.

The impact of background CO<sub>2</sub> concentration scenario assumptions is addressed in uncertainty discussions in Chapter 6.

NO<sub>x</sub> and AIC models average and greatly simplify the effects of the complex processes associated with forcing from ozone production and cloud formation, leading to large uncertainty. Models of ozone formation are complicated by nonlinear production rates that are sensitive to background composition and meteorological conditions. Moreover, the temperature response to equal ozone production forcings can vary with latitude and altitude due to strong dependence on local feedbacks.[52, 22] The short-lived ozone model presented here only attempts to capture the effects of varying altitude. However, on a globally-averaged scale, several studies have demonstrated a linear relationship between ozone production forcing and aircraft NO<sub>x</sub> emissions.[1]

Furthermore, the AIC forcing model scales simply with flight distance and does not reflect variation in impact with changing particle and water vapor emissions or exhaust temperature. The assumption that AIC forcing is proportional to flight distance may lead to an upper bound estimate of AIC impacts because it is likely that cloud cover will saturate in high density air traffic regions.[1] The forcing models applied here are based on results from global climate models; however, the level of scientific understanding of AIC impact estimation is still poor, particularly for induced cirrus cloudiness. It is expected that AIC models will be refined in the future as the climate modeling community achieves a better understanding of AIC impacts.

## 5.6 Uncertainty Quantification

Because of their low computational costs, linear climate models enable users to explore the climate responses of many scenarios and sensitivities to uncertain model parameters.[4] This section describes methods for quantifying the overall uncertainty in temperature change estimates produced with this climate model.

A number of sources of uncertainty exist in estimating the relative climate impacts of different aircraft.[67] Scientific uncertainty is the focus of this study and is associated with limits in scientific knowledge and inexact modeling approaches for quantifying impacts from an emissions scenario. Other sources include valuation and

scenario uncertainty. The selection of a climate metric, with explicit or implicit temporal weighting of impacts, affects the relative importance of short-term and long-term impacts and therefore involves valuation uncertainty. The climate metric adopted for studies in this research, ATR, is described in Chapter 3. Valuation uncertainty is not addressed directly, and these judgments are instead presented as user-specified inputs in the ATR framework. Scenario uncertainty refers to unknowns surrounding the projections of future anthropogenic activities and system responses that are required to estimate aircraft climate impacts. Scenario assumptions are implicit in the linear climate model presented in this chapter. The linear CO<sub>2</sub> radiative forcing model assumes constant background concentrations. The impact of this assumption is investigated by comparing results to a model with varying background concentrations. The climate model also assumes that physical climate responses will not change in the future, or in other words, that climate feedback mechanisms and all species' radiative efficiencies remain constant. This uncertainty is not quantified in this study and relates to future scenarios that are difficult to predict.

Scientific uncertainty is assessed by analyzing the uncertainty in each component of the climate model to construct information about the uncertainty of model outputs. Exact values of parameters used in the linear climate model are not known; instead, parameters can be more appropriately described by probability distributions over a range of possible parameter values. Distribution information for each model parameter is listed in Table 5.3, 5.4, 5.5, or 5.6. It should be noted that climate sensitivity,  $S$ , is a scaling value applied to all temperature calculations. This research is concerned with the relative impacts of competing aircraft designs, and this parameter's uncertainty is excluded because it has no effect on relative climate impact. Following Lee et al., the uncertainties in NO<sub>x</sub>-induced radiative forcing parameters ( $A_{\text{CH}_4}$ ,  $A_{\text{O}_{\text{SL}}}$ , and  $(\frac{RF_{\text{ref}}}{E_{\text{ref}}})_{\text{O}_{\text{3s}}}$ ) are likely to be coupled. Correlation coefficients of 0.5 are assumed between these three parameters.[1] All other uncertain parameters are assumed to be independent.

Uncertainties in forcing factor functions are based on uncertainty in data for  $\frac{RF_i}{E_{\text{NO}_x}}(h)$  and  $\frac{RF_{\text{AIC}}}{L}(h)$ .[14, 15] This information is used to calculate  $s_i(h)$  via equations (5.5) and (5.6). Probability distributions for  $\frac{RF_{\text{CH}_4}}{E_{\text{NO}_x}}(h)$  and  $\frac{RF_{\text{O}_{\text{3s}}}}{E_{\text{NO}_x}}(h)$  are assumed to

be normal, with 66% likelihood each parameter is within  $\pm 15\%$  of the published value. These distributions are inferred from results of the TRADEOFF project, where the change in  $\text{NO}_x$  impacts for altitude shifts of +2,000 and -6,000 ft were assessed by multiple climate models.[117] The altitude-dependent component of  $\frac{RF_{\text{AIC}}}{L}(h)$  is assumed to be normally distributed with 90% likelihood that the value is within  $\pm 70\%$  of the published result.[118]

While there is uncertainty in, for example,  $\frac{RF_{\text{O}_3S}}{E_{\text{NO}_x}}(h)$  at each altitude  $h$ , it is likely that uncertainty at a particular altitude is linked to uncertainty at nearby altitudes. That is to say, it is unlikely that the actual value of  $\frac{RF_{\text{O}_3S}}{E_{\text{NO}_x}}$  at 25,000 ft is 15% lower and at 27,000 ft is 15% higher than the data published by Radel and Shine.[15] To account for this, uncertainties in  $\frac{RF_L}{E_{\text{NO}_x}}(h)$  and  $\frac{RF_{\text{AIC}}}{L}(h)$  are assumed to be independent in 8,000 ft intervals. Specifically, the uncertainties of these parameters at 17,500, 25,500, 33,500, and 41,500 ft are independent, and the uncertainty at altitudes between these levels is based on a linear variation between the nodes. To calculate forcing factors  $s_i(h)$  based on uncertain values of  $\frac{RF_L}{E_{\text{NO}_x}}(h)$  and  $\frac{RF_{\text{AIC}}}{L}(h)$ , this information is renormalized via equations (5.5) and (5.6) so that the distance-weighted integral of  $s_i$  remains unity. Figure 5.4 shows the 66% likelihood ranges based on this method for  $s_{\text{O}_3S}$ ,  $s_{\text{CH}_4}$ , and  $s_{\text{AIC}}$ .

With known probability distributions for model parameters, output distributions are computed via Monte Carlo analysis with Latin hypercube sampling using software package DAKOTA.[119] This analysis relies on a large number of trials of calculating the climate impact metric, ATR, with random values from each parameter's probability distribution. A sufficient number of trials are computed so that the output distribution converges. Paired Monte Carlo analysis, described in Ref. [67], is used to estimate only the uncertainty that is relevant for comparative study.

## 5.7 Computing Average Temperature Response

With the linear climate model, time-varying temperature change can be calculated for an arbitrary aircraft emissions scenario. Determination of ATR requires calculation of temperature change for a scenario of constant emissions during the first  $H$  years of

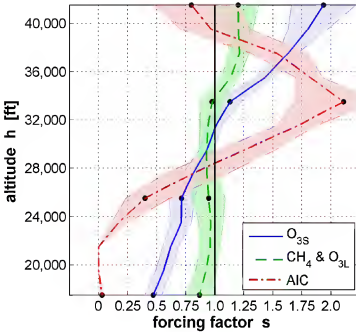


Figure 5.4: Forcing factors (lines) with 66% likelihood ranges (shaded areas). Altitudes with forcing factors based on radiative forcing data with independent probability distributions are marked with black points.

operation and zero emissions thereafter. This yields the quantity  $\Delta T_{sust,H}(t)$ , defined in equation (5.16).

$$\Delta T_{sust,H}(t) = \Delta T(t) \Big|_{s_i = \bar{s}_i, E_i(t) = e_i U_{sust} \sigma_H(t)} \quad (5.16)$$

$$\sigma_H(t) = \begin{cases} 1 & t \leq H \\ 0 & H < t \leq t_{max} \end{cases}$$

In equation (5.16), the index  $i$  includes all radiatively active emissions and effects ( $\text{CO}_2$ ,  $\text{NO}_x$ ,  $\text{H}_2\text{O}$ ,  $\text{SO}_4$ , soot, and AIC). Emissions rates are based on the performance of a particular aircraft on a specified mission. Sustained utilization rate,  $U_{sust}$ , is constant between configurations and years, and its value does not matter for comparative studies. The function  $\sigma_H(t)$  is a unity backward step, which characterizes the input

emissions scenario.  $\Delta T_{sust,H}(t)$  is calculated with mission-averaged forcing factors,  $\bar{s}_i$ , computed with equations (5.17) and (5.18).

$$\bar{s}_i = \frac{E_{\text{NO}_x, \text{cruise}}}{E_{\text{NO}_x}} \left( \frac{1}{h_f - h_0} \int_{h_0}^{h_f} s_i(h) dh \right) + \left( 1 - \frac{E_{\text{NO}_x, \text{cruise}}}{E_{\text{NO}_x}} \right) s_{i, \text{low}} \quad (5.17)$$

for  $i = \text{CH}_4, \text{O}_{3\text{L}}, \text{O}_{3\text{S}}$

$$\bar{s}_{\text{AIC}} = \frac{L_{\text{cruise}}}{L} \left( \frac{1}{h_f - h_0} \int_{h_0}^{h_f} s_{\text{AIC}}(h) dh \right) \quad (5.18)$$

These quantities,  $\bar{s}_i$ , are weighted averages of the forcing factors during the cruise, takeoff-landing, and climb-descent phases of the mission. Weighted averages for  $\text{NO}_x$  and AIC forcing factors are based on the proportion of emissions and flight distance, respectively, during each flight segment. The cruise segment forcing factor is calculated assuming a continuous cruise-climb with initial and final cruise altitudes  $h_0$  and  $h_f$ .  $\text{NO}_x$  forcing factors during takeoff, climb, descent, and landing are denoted  $s_{i, \text{low}}$  and based on forcing factors at  $h_{\text{low}} = 16,500$  ft. AIC forcing factors outside of cruise are taken to be zero. For current commercial aircraft on typical missions, a total distance of approximately 250 nautical miles is flown during climb and descent.[120]

Once  $\Delta T_{sust,H}$  is known and metric parameters (devaluation rate and operating lifetime) are specified, ATR can be computed with equation (3.1). However, because the climate model described herein is linear,  $ATR_r$  can be computed for multiple designs more quickly by defining a new quantity: unit ATR of species  $i$ .  $uATR_r(i)$  is defined as the ATR resulting from  $H$  years of unit emissions (1 kg per year or 1 nmi per year) of only species  $i$  and excluding altitude effects, shown in equation (5.19).

$$uATR_r(i) = ATR_r \Big|_{s_i=1, E_j(t)=\sigma_H(t) \text{ if } i=j \text{ and } 0 \text{ otherwise}} \quad (5.19)$$

With these unit ATRs precomputed,  $ATR_r$  becomes a simple summation for given utilization rate, cruise altitudes, and emissions per flight, as in equation (5.20).

$$ATR_r = U_{\text{sust}} \sum_i \bar{s}_i e_i uATR_r(i) \quad (5.20)$$

| Species, $i$     | $uATR_{r=0}(i)$         | $uATR_{r=1\%}(i)$       | $uATR_{r=3\%}(i)$       | $uATR_{r=\infty}(i)$    |                           |
|------------------|-------------------------|-------------------------|-------------------------|-------------------------|---------------------------|
| CO <sub>2</sub>  | 1.66 x10 <sup>-13</sup> | 4.36x10 <sup>-14</sup>  | 1.96x10 <sup>-14</sup>  | 5.59x10 <sup>-15</sup>  | K per kg CO <sub>2</sub>  |
| CH <sub>4</sub>  | -4.76x10 <sup>-12</sup> | -3.40x10 <sup>-12</sup> | -2.78x10 <sup>-12</sup> | -1.44x10 <sup>-12</sup> | K per kg NO <sub>x</sub>  |
| O <sub>3S</sub>  | 9.46x10 <sup>-12</sup>  | 7.19x10 <sup>-12</sup>  | 6.46x10 <sup>-12</sup>  | 4.85x10 <sup>-12</sup>  | K per kg NO <sub>x</sub>  |
| O <sub>3L</sub>  | -1.29x10 <sup>-12</sup> | -9.25x10 <sup>-13</sup> | -7.57x10 <sup>-13</sup> | -3.91x10 <sup>-13</sup> | K per kg NO <sub>x</sub>  |
| H <sub>2</sub> O | 5.77x10 <sup>-15</sup>  | 4.38x10 <sup>-15</sup>  | 3.94x10 <sup>-15</sup>  | 2.96x10 <sup>-15</sup>  | K per kg H <sub>2</sub> O |
| SO <sub>4</sub>  | -6.13x10 <sup>-11</sup> | -4.66x10 <sup>-11</sup> | -4.18x10 <sup>-11</sup> | -3.14x10 <sup>-11</sup> | K per kg SO <sub>4</sub>  |
| soot             | 2.38x10 <sup>-10</sup>  | 1.81x10 <sup>-10</sup>  | 1.63x10 <sup>-10</sup>  | 1.22x10 <sup>-10</sup>  | K per kg soot             |
| AIC              | 8.90x10 <sup>-13</sup>  | 6.76x10 <sup>-13</sup>  | 6.07x10 <sup>-13</sup>  | 4.56x10 <sup>-13</sup>  | K per nmi                 |

Table 5.7: Values of unit ATRs for  $H = 30$  years,  $t_{max} = 500$  years, and four different values of  $r$  calculated with a linear climate model.

Unit ATRs are calculated for several devaluation rates, an operating lifetime of 30 years, and a maximum integration period of 500 years in Table 5.7. These parameters are computed using the climate model described in this chapter. As more knowledge is gained, this climate model can be refined, and updated values for  $uATR$  should be applied.

# Chapter 6

## Aircraft Design Studies

### 6.1 Introduction

Commercial aviation emissions have grown over the past several decades despite improvements in fuel efficiency. A portion of these emissions affect the radiative balance of the Earth system, causing radiative forcing and climate change. The fraction of anthropogenic radiative forcing attributed to aviation is projected to rise,[1] and changes in aircraft operations and design may be necessary to meet goals for limiting climate change. This chapter investigates methods for reducing the climate impacts of future aircraft and quantifies the effects of these mitigation strategies on aircraft performance and operating costs. Several methods are explored, although policy options are not considered. First, because the magnitude of impacts from NO<sub>x</sub> emissions and AIC effects vary with altitude, one mitigation strategy involves designing aircraft to fly at altitudes with lower climate impact sensitivities. Past studies have investigated the climate impacts of shifting fleet altitudes, each generally demonstrating potential climate savings for flight at lower altitudes (e.g., Refs. [121, 117, 122, 123, 15, 14]). Secondly, the effects of technologies aimed at reducing aircraft climate impacts are assessed. This research focuses on near-term technologies and conventional aircraft configurations, although significant climate impact savings may be possible with non-hydrocarbon energy sources and less conventional aircraft such as blended wing bodies. Some of the technologies investigated, including drop-in alternative fuels and

operational contrail avoidance, can also be applied to the existing fleet in addition to future aircraft. In this chapter, narrowbody aircraft are assessed and the same conclusions are expected to apply to larger aircraft.[124]

## 6.2 Aircraft Optimization Problem

Aircraft analysis is performed using the conceptual design tool PASS (Program for Aircraft Synthesis Studies), described in Chapter 4. This tool integrates a set of industry design methods to compute aircraft performance based on aircraft design variables.[74] Aircraft climate impacts are computed with the climate model discussed in Chapter 5 and measured using the average temperature response (ATR) metric defined in Chapter 3 with two devaluation rates: 0% and 3%. These tools are combined with an optimizer to find the aircraft design parameter values that minimize a specified performance objective such as cost or average temperature response.

The set of aircraft studied carry 162 passengers and have payload, range, and performance requirements similar to those of a 737-800. Technology levels assumed for these aircraft are consistent with an entry-into-service year of 2010. Cost calculations are based on constant 2010 labor rates and a constant jet-A fuel price of \$2.25 per gallon, unless otherwise noted. The distances flown during most commercial airline missions are considerably shorter in length than the aircraft's maximum design range (3,000 nautical miles). For this reason, aircraft are optimized for performance on a "typical mission" while at the same time constrained to meet maximum design range requirements. A typical mission is defined as a flight with the design payload and a stage length of 1,000 nautical miles, based on the average narrowbody stage length for US carriers.[125] Each aircraft is designed with identical fuselage geometry but varying wing, engine, and mission design parameters. All configurations must meet the same takeoff, climb, cruise, and landing requirements. Optimization design variables and imposed constraints are listed in Tables 6.1 and 6.2.

Aircraft are designed to minimize a combination of operating costs, emissions, and ATR. A gradient-based method is used to solve this constrained optimization

| Design variable                                    | Upper bound | Lower bound |
|--|-------------|-------------|
| Maximum takeoff weight (TOW) (lbs)                 | 100,000     | 200,000     |
| Typical mission takeoff weight (lbs)               | 100,000     | 200,000     |
| Wing area (ft <sup>2</sup> )                       | 1,000       | 2,000       |
| Wing aspect ratio                                  | 7           | 24          |
| Wing sweep (degrees)                               | 0           | 34          |
| Average wing thickness-to-chord ratio              | 0.05        | 0.2         |
| Wing fuselage location                             | 0.2         | 0.6         |
| Sea-level static thrust (lbs)                      | 15,000      | 35,000      |
| Turbofan bypass ratio                              | 5           | 20          |
| Horizontal tail area / wing area                   | 0.2         | 0.5         |
| Cruise Mach number                                 | 0.45        | 0.9         |
| Design mission initial and final cruise altitudes  | 17,000      | 43,000      |
| Typical mission initial and final cruise altitudes | 17,000      | 43,000      |
| Maximum zero fuel weight / maximum takeoff weight  | 0.6         | 0.95        |
| Takeoff Mach number                                | 0.05        | 0.25        |
| Landing Mach number                                | 0.05        | 0.25        |

Table 6.1: List of optimization design variables and their bounds.

| Constraint                              |        | Value               |
|---|--------|---------------------|
| Design mission range                    | $\geq$ | 3000 nmi            |
| Typical mission range                   | $\geq$ | 1000 nmi            |
| Takeoff field length                    | $\leq$ | 7500 ft             |
| Landing field length                    | $\leq$ | 5500 ft             |
| Second segment climb gradient           | $\geq$ | 2.4%                |
| Minimum stability margin                | $\geq$ | 0.1                 |
| Cruise drag-to-thrust ratio             | $\leq$ | 0.88                |
| Wing lift coefficient margin            | $\geq$ | 0.01                |
| Horizontal tail lift coefficient margin | $\geq$ | 0.01                |
| Chordwise main landing gear position    | $\leq$ | 0.85                |
| ICAO certification noise                | $\leq$ | Chapter 4 standards |

Table 6.2: List of optimization performance constraints.

problem. Economic and environmental performance is compared for a variety of technology scenarios in the following sections.

## 6.3 Results with Baseline Technology

First, optimization results are presented for designs using conventional technologies likely to be applied on an airliner entering service in 2010. These baseline technologies include a lightweight composite structure and advanced, high bypass ratio turbofan engines. Combustor performance is comparable to recently certified engines with a NO<sub>x</sub> emissions index model based on the GE90-85B dual annular combustor, see Chapter 5. In this section, instead of applying technologies aimed at reduced climate impacts, the effects of varied wing and engine design variables, cruise speed, and altitudes are considered. First, single-objective optimization results for minimum cost, emissions, and climate impact aircraft are discussed. Then, multi-objective results are presented, featuring designs with concurrently optimal cost and climate performance.

### 6.3.1 Single-Objective Results

Aviation induced cloudiness and emissions of CO<sub>2</sub> and NO<sub>x</sub> combine to produce the majority of commercial aviation's climate impacts. One method to reduce the net climate impacts of future aircraft is to design for reduced emissions. Table 6.3 compares aircraft designed to minimize five different objective functions: total operating costs, total fuel burn (directly proportional to CO<sub>2</sub> emissions), total NO<sub>x</sub> emissions, ATR<sub>r=0</sub>, and ATR<sub>r=3</sub>.

The minimum cost aircraft represents the most economically competitive design that also meets current safety and environmental regulations. This configuration is generally similar to current aircraft operating in the single aisle, medium range market, but has improved performance, reflecting 2010 technology levels. The aircraft cruises near Mach 0.84 and features a moderate aspect ratio, highly swept wing and



|   | min cost | min fuel | min NO <sub>x</sub> | min ATR <sub>r=0</sub> | min ATR <sub>r=3</sub> |
|---|----------|----------|---------------------|------------------------|------------------------|
| Maximum TOW [lbs]   | 161,600  | 163,400  | 184,500             | 165,000                | 166,400                |
| Typical mission TOW [lbs]   | 140,600  | 146,200  | 162,000             | 146,700                | 147,300                |
| Wing area [ft <sup>2</sup> ]  | 1520     | 1640     | 1620                | 1470                   | 1470                   |
| Wing aspect ratio   | 8.9      | 19.3     | 20.2                | 20.3                   | 20.6                   |
| Wing sweep [degrees]  | 34.0     | 8.6      | 8.0                 | 5.8                    | 5.5                    |
| Cruise Mach number  | 0.835    | 0.573    | 0.475               | 0.493                  | 0.469                  |
| Initial cruise altitude [ft]  | 38,600   | 32,400   | 30,000              | 21,500                 | 17,000                 |
| Final cruise altitude [ft]  | 39,800   | 36,200   | 31,500              | 21,500                 | 20,100                 |
| SLS thrust [lbs]  | 23,200   | 19,600   | 32,300              | 20,400                 | 20,600                 |
| Engine bypass ratio   | 8.4      | 17.9     | 10.4                | 17.3                   | 17.0                   |
| Avg. cruise velocity [kts]  | 478      | 331      | 279                 | 301                    | 290                    |
| Normalized TOC  | 1.0000   | 1.060    | 1.196               | 1.101                  | 1.117                  |
| Normalized W <sub>fuel</sub>  | 1.000    | 0.868    | 1.076               | 0.966                  | 0.993                  |
| Normalized E <sub>NO<sub>x</sub></sub>  | 1.000    | 0.722    | 0.520               | 0.691                  | 0.678                  |
| Cruise EI <sub>NO<sub>x</sub></sub> [g/kg]                                    | 19.8     | 15.7     | 6.5                 | 13.1                   | 12.4                   |
| O <sub>3</sub> forcing factor   | 1.48     | 1.08     | 0.74                | 0.59                   | 0.51                   |
| CH <sub>4</sub> forcing factor  | 1.13     | 1.01     | 0.90                | 0.94                   | 0.89                   |
| AIC forcing factor  | 0.80     | 1.46     | 1.16                | 0.0                    | 0.01                   |
| Normalized ATR <sub>r=0</sub>   | 1.000    | 0.948    | 0.970               | 0.636                  | 0.648                  |
| Fraction of ATR <sub>r=0</sub> from CO <sub>2</sub> /NO <sub>x</sub> /AIC [%] | 65/17/17 | 60/8/32  | 73/2/25             | 99/0/0                 | 100/-1/0               |
| Normalized ATR <sub>r=3</sub>   | 1.000    | 1.022    | 0.824               | 0.263                  | 0.256                  |
| Fraction of ATR <sub>r=3</sub> from CO <sub>2</sub> /NO <sub>x</sub> /AIC [%] | 24/41/34 | 20/18/61 | 31/7/61             | 86/9/0                 | 91/2/2                 |

Table 6.3: Description of aircraft designed for single-objective economic or environmental performance.

moderate bypass ratio, wing-mounted turbofan engines. Its ATR<sub>r=3</sub> has approximately equal contributions from CO<sub>2</sub>, NO<sub>x</sub> and AIC effects. Since long-lived emissions are weighted more heavily with lower climate devaluation rates, CO<sub>2</sub> impacts constitute two-thirds of this configuration's ATR<sub>r=0</sub>.

The minimum fuel burn, or minimum CO<sub>2</sub>, configuration saves approximately 13%

in fuel consumption relative to the minimum cost design. Since the aircraft cruises at a much slower Mach 0.57, the wings are designed with a high aspect ratio and low sweep, leading to lower induced drag. Reduced drag allows the aircraft to meet climb requirements with smaller engines. This configuration also uses higher bypass ratio turbofan engines with decreased thrust specific fuel consumption. Despite savings in fuel costs, this low speed design has 6% higher total operating costs, owing to lower per-unit utilization rates and increased crew and maintenance costs associated with long flight times. The minimum fuel aircraft flies approximately 5,000 ft lower than the minimum cost aircraft in a region where contrail formation is more likely; even though fuel burn is 13% lower, only 5.2% savings in  $ATR_{r=0}$  and a 2.2% penalty in  $ATR_{r=3}$  are realized compared with the reference aircraft.

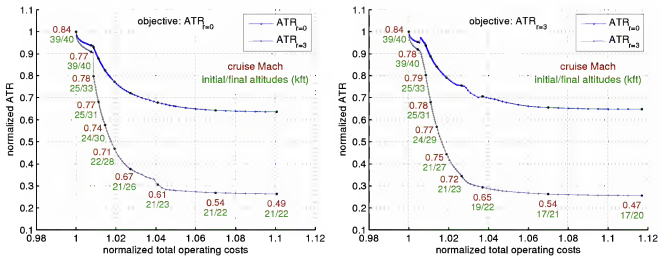
The minimum  $NO_x$  aircraft emits nearly 50% less  $NO_x$  compared with the minimum cost design. This configuration has very high thrust engines so that during cruise the engines can be throttled back, yielding an extremely low emissions index. However, the resulting heavy airframe and low flight speed cause this design's operating costs to escalate relative to the other four configurations. As with the low fuel aircraft, the low  $NO_x$  aircraft cruises at lower altitudes where contrail impacts are more severe. A greater AIC forcing factor and higher fuel burn cancels out the benefit of lower  $NO_x$  emissions, as measured by  $ATR_{r=0}$ . On the other hand,  $ATR_{r=3}$ , which is more sensitive to short-lived effects from  $NO_x$  emissions, is reduced by 18%.

Lastly, two aircraft are designed to minimize climate impacts as measured by  $ATR$ . These designs differ from the minimum emissions designs in their very low design cruise altitudes. By cruising at Mach 0.5 and 20,000 ft, atmospheric impacts from  $NO_x$ , contrails, and cirrus are essentially eliminated and climate impacts are almost entirely due to  $CO_2$  emissions. The minimum  $ATR_{r=3}$  configuration cruises at slightly lower altitudes to reduce short-lived impacts at the expense of 3% higher fuel burn and  $CO_2$  emissions. At this altitude, the cooling impacts from methane and long-term ozone destruction exceed warming impacts from short-term ozone production, and the net  $ATR_{r=0}$  due to  $NO_x$  is negative. The resulting designs exhibit 35% lower  $ATR_{r=0}$  and 74% lower  $ATR_{r=3}$  than the reference minimum cost aircraft. Operating costs are penalized approximately 10-12%, primarily due to longer mission times.

These results draw attention to the difference in design characteristics and performance between aircraft optimized for different environmental metrics. The minimum NO<sub>x</sub> design has higher fuel burn than even the minimum cost design, even though total emissions quantity depends directly on fuel consumption, see equation 5.2. The minimum fuel burn design has little or no climate savings, measured by ATR<sub>r=0</sub> and ATR<sub>r=3</sub> (5.2% or -2.2% compared with minimum cost value), despite large fuel savings (13%). Thus, designing an aircraft to be green by one environmental standard does not ensure that the aircraft will be green in other environmental metrics, even if all metrics are related to emissions and atmospheric impacts. In particular, design cruise altitude has a powerful effect on the net climate impacts of a configuration.

### 6.3.2 Cost-Climate Tradeoff

For a low climate impact aircraft to be viable in the airline industry, it must also perform competitively economically. This section assesses the relationship between operating costs and climate impacts with conventional 2010 aircraft technology. By optimizing designs for minimum ATR and varying constraints on cost, or vice versa, a pareto front is generated. Figure 6.1 shows this tradeoff between cost and both ATR<sub>r=0</sub> and ATR<sub>r=3</sub> for narrowbody configurations. Each point on the figure represents a separate design, optimized to minimize a different balance of economic and climate performance. Details for the three extrema on the pareto fronts are provided in Table 6.3. Reducing design cruise altitude and Mach number has a dramatic effect on climate impacts measured by ATR, regardless of the devaluation rate. As the figure shows, climate impact savings on the order of 35-75% are possible by flying slower and lower than the present-day fleet. These low climate impact designs have higher operating costs due largely to longer mission times. By reducing altitude by about 12,000 ft to levels where both NO<sub>x</sub> and cloud impacts are less severe, ATR<sub>r=0</sub> and ATR<sub>r=3</sub> decrease by about 10% and 30%, respectively, for a 1% increase in total operating costs.



(a) Optimized  $ATR_{r=0}$ ; evaluated  $ATR_{r=3}$  also shown. (b) Optimized  $ATR_{r=3}$ ; evaluated  $ATR_{r=0}$  also shown.

Figure 6.1: Baseline designs optimized for minimum total operating costs and ATR with two devaluation rates,  $r = 0$  and  $r = 3\%$ . Black points indicate designs with listed cruise altitudes and Mach numbers.

Figure 6.1 includes results for two climate objective functions. Designs with optimal  $ATR_{r=0}$  are discussed first, and later compared with optimal  $ATR_{r=3}$  configurations. The lowest cost section of the pareto front in Figure 6.1(a) has a kink around which the slope of the curve changes sharply. Beginning at the minimum cost point, designs fly successively slower to improve aerodynamic efficiency and reduce thrust required for climb. After reducing fuel burn by up to approximately 5% by cruising slower, climate impacts can be reduced more drastically by flying at much lower altitudes. The point that separates these high and low altitude designs is indicated on Figure 6.1(a) by the second lowest cost black point. This design cruises between 39,000 and 40,000 ft at Mach 0.77 and has smaller engines and a lighter airframe than lower cost designs. Pareto optimal designs with lower  $ATR_{r=0}$  cruise at altitudes of at most 34,000 ft. At lower altitudes, reductions in  $NO_x$  and AIC forcing factors more than offset the increase in fuel burn from flying in denser air. Additionally, more thrust is available at lower altitudes, allowing the engines to be throttled back, which reduces internal combustor temperatures, and consequently, cruise  $NO_x$  emissions indices. From this kink point, further reductions in climate impacts are achieved by

flying at even lower altitudes and speeds.  $ATR_{r=0}$  is minimized at a cruise altitude near 22,000 ft.

Figure 6.1(b) indicates similar findings for designs optimized with the climate objective function  $ATR_{r=3}$ . This metric devaluation applies a lower weighting to long-lived CO<sub>2</sub> impacts. Thus, the pareto front more quickly shifts to low altitude, higher fuel burn designs, resulting in configurations with lower  $ATR_{r=3}$  but higher  $ATR_{r=0}$ . Optimal  $ATR_{r=3}$  designs cruise at slightly faster speeds than optimal  $ATR_{r=0}$  designs, trading lower mission times for greater fuel burn. Results with these two objective functions are otherwise similar; because of this, for the remainder of this chapter, only results for the climate objective function  $ATR_{r=0}$  are presented.

## 6.4 Results with Climate Mitigation Technologies

Design optimization results for the baseline technology scenario illustrate the strong dependence of climate impacts, as measured by ATR, on design cruise altitude and speed. Through application of climate impact reduction technologies, significant decreases in climate impacts may be possible with smaller penalties to total operating costs. A number of previous studies have reviewed climate mitigation technologies and operational strategies (e.g., Refs. [24, 25, 26, 22]). This section explores the potential benefits of several green technologies: propfan engines, natural laminar flow, alternative fuels, low NO<sub>x</sub> combustors, and contrail avoidance. The list of mitigation strategies investigated is not intended to be comprehensive, but instead explores the benefits of a few key technologies that could be applied to aircraft in the next 10-20 years. The effects of climate change policy options are not assessed in this research.

### 6.4.1 CO<sub>2</sub> Impact Reduction

CO<sub>2</sub> emissions affect global climate on timescales much longer than other aircraft emissions, causing residual temperature change for many hundreds of years after release into the atmosphere. CO<sub>2</sub> emissions are directly proportional to fuel consumption, leading to two methods to mitigate impacts: reducing fuel burn or using a

fuel with lower CO<sub>2</sub> intensity. The potential for fuel savings by designing aircraft for slower cruise speeds is discussed in the previous section. Technologies such as open rotor engines and laminar flow also provide fuel savings, particularly when applied to aircraft with reduced cruise speeds relative to present-day commercial transports. In addition to low fuel burn technologies, the substitution of biofuels for traditional petroleum-based fuels could reduce or even eliminate the climate impacts of aviation CO<sub>2</sub> emissions.

### Propfan Engines

Propfan engines, also known as open rotors, are unducted, very high bypass ratio engines. Unlike traditional turboprop engines, propfans feature highly swept blades, allowing for efficient performance at speeds of up to Mach 0.8.[82] These engines achieve high propulsive efficiency without the weight and drag penalties associated with large fan nacelles of comparable bypass ratio turbofans. Both single and dual rotor propfans could be considered for application on future commercial aircraft, with counter-rotating propfans being more efficient but noisier. Performance, weight, and drag models for propfan engines are described in detail in Chapter 4. Following Goldsmith, a fuselage weight penalty of 500 pounds is applied to propfan configurations for cabin interior noise insulation.[126] To account for the fewer number of seats with engine noise exposure on configuration with aft fuselage mounted engines, this weight penalty is reduced by 25%. Figure 6.2 compares the economic and climate performance of configurations with turbofan and dual and single rotor propfan engines. Because of the high uncertainty in estimating weight and performance of future propfan engines, the effects of a 5% increase in specific fuel consumption and a 20% increase in weight on dual rotor propfans are also shown in Figure 6.2.

A number of technical challenges exist in the development of propfan engines, including community noise concerns. The lack of fan casing makes acoustic treatment more difficult. A recent workshop of academia and industry concluded that advanced open rotors are likely to “comfortably” meet current Chapter 4 noise certification standards, particularly if operational procedures are designed to minimize

noise exposure.[104, 105] However, it should be noted that even if engines meet certification levels, the public may object to propfans' more tonal noise.[127] In this study, all aircraft are required to meet current ICAO Chapter 4 noise standards. A conservative estimate for counter-rotating propfan noise is assumed based on 1990 scale model tests by Hoff et al.[106] Figure 6.2 also shows results for a dual rotor propfan that is 1.5dB quieter at each certification point, reflecting modern acoustic design improvements.

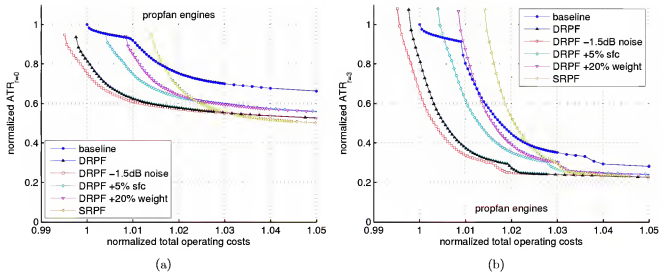


Figure 6.2: Designs optimized for minimum total operating costs and  $ATR_{r=0}$ , applying propfan engines with varying assumptions.

Dual rotor propfan configurations save on the order of 15-20% fuel burn relative to turbofan designs, enabling lower total operating costs and climate impacts. Propfan aircraft performance is hindered by high thrust lapse, meaning that the engine has less available thrust at cruise than a lower bypass ratio engine with equal sea level static thrust. As a result, the minimum cost propfan configuration optimally cruises at a slower Mach 0.77, with a lower sweep, higher aspect ratio wing to reduce required thrust from its heavy engines. Similar to baseline designs, propfan aircraft cruise at lower altitudes and speeds to reduce ATR, trading increased fuel burn and longer flight times for lower AIC and  $NO_x$  impacts. These propfan designs are constrained

by Chapter 4 noise limits, causing designs to takeoff over a shorter distance to reduce takeoff noise and have a larger wing and lower thrust engines than would be otherwise optimal. The cost of this design constraint is illustrated by comparing results with quieter dual rotor propfans, which meet noise constraints with a margin. Also shown are results for dual rotor propfan configurations with less efficient and heavier engines, which burn 2-5% more fuel burn than reference propfan designs. These fuel burn penalties eliminate the operating cost savings of propfan engines. Finally, single rotor propfan configurations are penalized in the simple swirl loss model applied here, causing optimized configurations to cruise at slower speeds. As a result, single rotor propfan configurations have higher operating costs than baseline designs despite having very low specific fuel consumption.

### Natural Laminar Flow

Aircraft fuel consumption can be improved through reductions in profile drag, with skin friction accounting for about half of conventional aircraft drag at cruise.[26] By designing surfaces to maintain laminar boundary layers over greater portions of the wing and tail, significant drag and fuel savings can be achieved.[26, 24, 20] Natural laminar flow surfaces are designed with favorable pressure gradients and very low sweep to passively stabilize boundary layers without requiring cooling or suction.

The effects of natural laminar flow are modeled by assuming that transition occurs at 60% chord on the upper wing surface and 5% chord on the lower surface, and transition on the tail upper and lower surfaces occurs at 60% chord. By designing for turbulent flow on the lower wing surface, wings are compatible with use of Kreuger flaps for high-lift and less susceptible to loss of laminar flow from bugs and debris. Skin friction coefficients are computed based on the specified transition locations and Reynolds number with adjustments for thickness and lift coefficient.[75] These assumptions are based on more refined analyses that compute surface pressure distributions directly and account for changes in compressibility drag (e.g., Ref. [20]).

A natural laminar flow configuration designed by Allison et al. is shown in Figure 6.3. This design was estimated to burn 6% less fuel than a fully turbulent design at the same Mach number.[20] Following this study, wing sweep is limited to no more

than seven degrees due to crossflow and attachment line instabilities, and additional fuel must be carried in reserves so that the aircraft meets range requirements (at reduced speed) if laminar flow is lost at the beginning of the mission.[20] Engines are mounted on the aft fuselage, resulting in a 1500 pound structural weight penalty for propfan configurations based on the study by Goldsmith.[126] Placement of heavy, high bypass ratio engines on the aft fuselage leads to large variation in center of gravity location and the requirement of an oversized tail. A ballast tank is used at low payload conditions to reduce tail size. Maintenance costs for turbulent and natural laminar flow aircraft are assumed to be similar, although laminar configurations may experience higher maintenance costs.



Figure 6.3: A natural laminar flow narrowbody aircraft design from Ref. [20].

Design optimization results for natural laminar flow configurations are shown in Figure 6.4. Also shown are results for natural laminar flow with a more conservative target of 40% upper surface laminar flow and a more ambitious goal of 60% upper and lower surface laminar flow. The minimum cost configuration with 60% upper surface natural laminar flow burns approximately 12% less fuel than the minimum cost reference aircraft. This laminar flow design cruises at a slower Mach 0.72, resulting

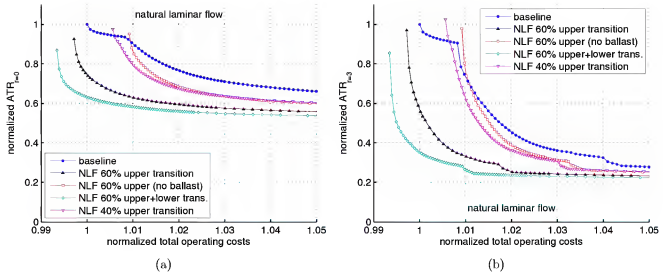


Figure 6.4: Designs optimized for minimum total operating costs and  $ATR_{r=0}$ , applying natural laminar flow with varying assumptions.

in 0.3% lower total operating costs. Laminar flow designs also fly at a lower optimal lift coefficient and, thus, cruise at slightly lower altitudes than turbulent reference aircraft. Therefore, natural laminar flow allows aircraft to efficiently reduce climate impacts from  $NO_x$  emissions and AIC by flying at altitudes where impacts are less severe. Because minimum cost laminar flow aircraft already cruise below peak contrail formation altitudes, these pareto fronts lack the kink observed in baseline technology optimization results. By designing for upper and lower surface laminar flow, an additional 1-3% fuel burn reduction is realized, improving economic performance but also leading to more difficult challenges in wing maintenance and high-lift design. Reducing the fraction of upper surface laminar flow to 40% leads to the loss of 4% of fuel burn savings. A similar erosion of fuel burn benefits is observed for laminar flow designs that do not use ballast. In these configurations, a very large tail is required for stability at aft center of gravity conditions, resulting in large weight and drag penalties.

### Alternative Fuels

Another mitigation strategy for reducing the impacts of aircraft CO<sub>2</sub> emissions involves the substitution of alternative fuels. This research focuses on drop-in alternative fuels, which require little or no modification to infrastructure and engine design. (Other non-kerosene alternative fuels including liquid hydrogen could also enable reduced emissions, e.g. Ref. [68].) Drop-in alternative fuels created from biomaterial have the potential for reduced life cycle long-lived greenhouse gas (LLGHG) emissions relative to conventional fuels because feedstocks used to produce these fuels absorb CO<sub>2</sub> from the atmosphere during their growth. The total quantity of life cycle LLGHG emissions savings varies significantly with the type of feedstock, production methods, and location.[5] Estimates of life cycle greenhouse gas emissions per pound of burned fuel for a variety of renewable fuel sources normalized by conventional fuel emissions are listed in Table 6.4.[5] Potential life cycle emissions savings are greatest for second generation biofuels produced from sources including jatropha, camelina, algae, and halophytes.[128, 5, 129]

| Fuel Pathway  | Normalized Life Cycle LLGHG Emissions |
|---|---------------------------------------|
| Crude oil to conventional jet fuel                  | 1.00                                  |
| Rapeseed oil to hydroprocessed renewable jet fuel   | 0.63 or 1.11                          |
| Jatropha oil to hydroprocessed renewable jet fuel   | 0.45                                  |
| Algae oil to hydroprocessed renewable jet fuel      | 0.58                                  |
| Salicornia oil to hydroprocessed renewable jet fuel | 0.06 or 0.55                          |

Table 6.4: Normalized baseline life cycle greenhouse gas emissions for various fuel pathways from Ref. [5]. Multiple values indicate varying land use change assumptions.

Second generation biojet fuel penetration of 30% has been projected for 2030 by some sectors of the industry,[24, 129] and the same ratio is included in 2050 sustainable growth scenarios by the International Energy Agency (IEA).[130] Greener by Design forecasts 20% biofuel use by 2030, and the UK government advisory Committee on Climate Change views 10% biojet penetration by 2050 as likely.[131, 132] Life cycle LLGHG intensity reductions of 50% are possible with second generation fuels, but

these savings could be curtailed by increased greenhouse gas emissions from land use change.[132, 5]

Prices for second generation biojet fuels are likely to exceed present conventional fuel prices. One study estimates the price of advanced production algae-based biojet at approximately \$110 per barrel in 2005 dollars.[133] The IEA projects a crude oil price in 2030 of \$130 per barrel based on current policies, which translates into a refined jet fuel price of about \$86 per barrel in 2005 dollars.[134] Applying a 30% biojet blend rate, this yields an 8% increase in fuel price. This estimate is consistent with the conclusions of E4tech, predicting that second generation biofuels will break even in costs with conventional fuels in the 2030 timeframe.[135] Projections of prices of petroleum-based and biojet blend fuels in the future are highly uncertain, and these estimates are included to illustrate the possible tradeoff between fuel carbon intensity and price.

Figure 6.5 shows the tradeoff between operating costs and ATR, applying biojet blend fuels with varying assumptions. In all cases, it is assumed that there is no difference in non-CO<sub>2</sub> emissions between biojet blend and conventional fuels, although this is the subject of ongoing research in the FAA research consortium PARTNER.[136] (In particular, biofuel use may cause greater concentrations of soot and aldehydes and lower concentrations of aromatics.[137]) The nominal scenario assumes an 8% increase in fuel price and a 15% reduction in CO<sub>2</sub> based on 30% use of biofuels with 50% lower greenhouse gas intensity. Other scenarios include one with a 15% reduction in CO<sub>2</sub> and no fuel price change and one with a 5% reduction in CO<sub>2</sub>.

Use of alternative fuels with lower greenhouse gas intensity directly reduces impacts from CO<sub>2</sub> emissions, as shown in Figure 6.5. By replacing 30% of conventional fuel with second generation biojet, more than 10% savings in ATR<sub>r=0</sub> and 4% savings in ATR<sub>r=3</sub> are gained. Greater savings are measured with ATR<sub>r=0</sub> because this metric assigns heavier weighting to long-lived CO<sub>2</sub> impacts. Minimum cost alternative fuel configurations are nearly identical in layout to minimum cost conventional fuel designs. Additional climate impact savings are achieved by flying at lower altitudes, similarly to designs shown in Figure 6.1. If alternative fuels are more expensive than

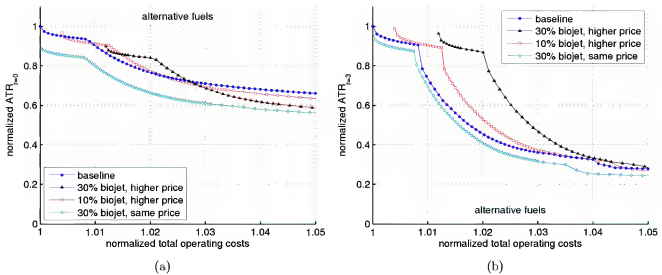


Figure 6.5: Designs optimized for minimum total operating costs and  $ATR_{r=0}$ , applying biojet fuels with varying assumptions.

conventional fuel, total operating costs increase by more than 1%. This price scenario is speculative, but illustrates the potential increase in fuel costs for sustainable, second generation biofuel.

#### 6.4.2 NO<sub>x</sub> Impact Reduction

The combined warming and cooling effects of NO<sub>x</sub> emissions account for between 20% and 40% of a conventional, modern aircraft's ATR, as indicated in Table 6.3. Because NO<sub>x</sub> radiative efficiency increases with cruise altitude, flying at lower altitudes reduces climate impact for a given quantity of emissions. This strategy is exploited by designs shown in Figure 6.1. Impacts can also be reduced by decreasing the amount of NO<sub>x</sub> released into the atmosphere. NO<sub>x</sub> emissions indices vary between engine configurations based on combustor design and maximum core temperatures, with higher temperatures yielding improved fuel efficiency but also greater NO<sub>x</sub> emission rates. The drive toward higher engine thermal efficiency has made the challenge of low NO<sub>x</sub> combustor design more difficult. One option to reduce NO<sub>x</sub> emissions indices is to design future engines with lower overall pressure ratios, effectively trading increased

fuel burn and CO<sub>2</sub> emissions for reduced NO<sub>x</sub>.[24] Instead, this research considers application of advanced combustors for future engines with very high thermal efficiency.

Most ultra low, high performance combustor concepts fall into the categories of lean burn or rich burn, quick quench, lean burn (RQL) designs.[45] A number of technology programs are exploring these design concepts (e.g., Refs. [138, 139, 140, 112, 141]). The climate benefits of low NO<sub>x</sub> combustors are assessed in this work by modeling their performance based on industry goals. Emissions performance goals for future combustors are often posed relative to NO<sub>x</sub> landing and takeoff regulations, the current standard being CAEP6.[23] ICAO set a long-term technology goal of achieving landing and takeoff emissions below CAEP6-60% limits by 2026, and progress toward this goal has already been made.[142] The EU Advisory Council for Aeronautics Research in Europe (ACARE) seeks to reduce 2020 NO<sub>x</sub> emissions by 80% relative to 2000 levels, commensurate with a 50% reduction in CO<sub>2</sub>.[143] NASA research goals for 10 years and beyond include a more than 80% reduction in certification emissions relative to CAEP2 limits.[22] Based on these goals, a future advanced combustor with CAEP6-60% emissions levels is modeled, noting that recently certified engines already perform at 5-20% below CAEP6 standards.[45] Following the performance of conventional combustors, an equal percentage reduction in NO<sub>x</sub> emissions index is applied during landing, takeoff, and cruise; however, for future lean burn direct injection combustors, this relationship is not automatic and cruise performance must be optimized separately.[45] Finally, in the past, low NO<sub>x</sub> combustor design has generally not penalized fuel economy, an assumption that is applied here. Despite this, advanced lean burn direct injection combustors could increase engine weight by up to 100 kilograms.[45]

Figure 6.6 shows the tradeoff between operating costs and ATR for three combustor scenarios: CAEP6-60% with no weight penalty, CAEP6-75% with no weight penalty, and CAEP6-60% with a 100 kg combustor weight penalty. In each case, the emissions indices of all engines are scaled by the same factor, such that the minimum cost configuration (with a bypass ratio 8.4, SLS overall pressure ratio 41 engine) meets the specified emissions target. For reference, the baseline technology combustor performs with a 25% margin below CAEP6 limits. More efficient, higher bypass ratio

engines exceed emissions reduction targets because of the dependence of certification emissions on fuel consumption.

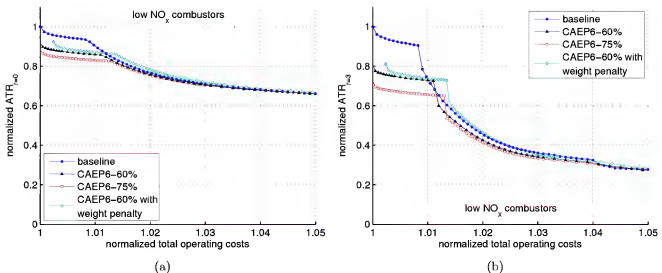


Figure 6.6: Designs optimized for minimum total operating costs and  $ATR_{r=0}$ , applying low  $NO_x$  combustor technology with varying assumptions.

Reduced  $NO_x$  emissions with a CAEP6-60% combustor translate into 9% and 20% savings in  $ATR_{r=0}$  and  $ATR_{r=3}$ , respectively, for minimum cost designs. Greater environmental savings are possible with an ultra low emissions, CAEP6-75% combustor. When no combustor weight penalty is assumed, these climate impact savings are achieved without an increase in total operating costs. If the low  $NO_x$  combustor is assumed to weigh 100 kg more, operating costs are penalized by approximately 0.2%, still producing lower net climate impacts than a range of baseline configurations with equal operating costs. CAEP6-60% combustor designs emit half as much  $NO_x$  as baseline designs, allowing low cost designs to cruise at 38,000 to 40,000 ft where  $CO_2$  impacts are minimized and above contrail formation altitudes. Shown in Figure 6.1, baseline technology designs quickly shift from this altitude range because  $NO_x$  emissions efficiently produce the greenhouse gas ozone in this region. Configurations with operating costs about 1.3% higher than the reference design cruise at altitudes below about 31,000 ft, beneath contrail formation altitudes and where  $NO_x$

sensitivity is reduced. At these altitudes, the benefits of low NO<sub>x</sub> combustors are virtually eliminated. Configuration design variables for low NO<sub>x</sub> designs are similar to those of baseline designs.

### 6.4.3 AIC Impact Reduction

The effects of aviation induced cloudiness constitute a significant portion of commercial aviation's climate footprint. For the conventional, minimum cost aircraft described in section 6.3, the fraction of ATR attributed to AIC varies between 15% and 35%, depending on the metric devaluation rate. Several technical and operational AIC mitigation methods have been proposed and are described in reviews by Gierens et al., Noppel and Singh, and Lee et al.[144, 145, 22] This research focuses on the potential environmental savings of an operational contrail avoidance strategy.

AIC impact magnitude varies considerably with an aircraft's cruise altitude. Average contrail radiative forcing per distance flown is highest at a cruise altitude of approximately 33,000 ft, and this forcing is halved by flying either above 39,000 ft or below 29,000 ft, as shown in Figure 5.2.[15] Studies by Williams et al. and Fichter et al. have suggested shifting the current fleet's cruise altitudes down several thousand feet to reduce AIC impacts.[146, 122] Results from the previous section support the conclusion that flying at altitudes below 30,000 ft could substantially reduce an aircraft's net climate impacts. However, it may be possible to decrease contrail formation frequency while continuing to fly at conventional cruise altitudes through an operational strategy suggested by Mannstein et al.[147] Analysis of atmospheric data has indicated that ice-supersaturated and sufficiently cold layers (where persistent contrails can form) are usually thin in height with mean thicknesses of approximately 500-1000 meters (about 1500-3000 ft).[148, 149, 150] Moreover, usually at most one contrailing ice-supersaturated layer (CISSL) exists at a single location and time. Thus, when a CISSL is predicted or detected, an aircraft could shift altitudes up or down 2000-4000 ft to avoid forming a persistent contrail. It is expected that shifts of 2000-4000 ft would be sufficient to avoid contrail formation between 50% and 80% of the time.[147, 150] This flexible contrail avoidance strategy could be designed

to prioritize avoiding formation of winter and nighttime contrails, which have potent radiative effects.[35] However, this type of strategy would lead to increased congestion and air traffic management workload. Furthermore, implementation of such a system requires improved humidity sensors, weather forecasting, and flight planning systems.[147, 124]

The effects of this real-time contrail avoidance strategy are simulated, and the resulting tradeoff between cost and climate impacts is shown in Figure 6.7. It is assumed that a contrail avoidance mission includes a single 2000-4000 ft shifted cruise segment spanning 20% of the cruise distance, leading to an average fuel burn penalty of 0.5% based on mission analysis of current aircraft.[124] This fuel burn penalty assumes that the aircraft maintains its speed during the shifted altitude segment so that flight time is unchanged, but it may be desirable to adjust speed to improve fuel economy. This is a notional flight scenario following the 10-20% frequency in which current aircraft encounter contrail formation conditions.[15] However, the horizontal scope of CISSLs is poorly understood, and it is likely that on individual flights an aircraft may require fewer or more, and shorter or longer, shifted cruise segments. Radiative forcing from AIC is assumed to be reduced by 50% through this strategy. It should be noted that AIC includes not only persistent contrails and aged contrail-cirrus, but also soot cirrus. While this contrail avoidance strategy can be expected to reduce impacts from persistent and aged contrails, its impacts on soot cirrus are highly uncertain. Because of the uncertainty, results are also shown for AIC reduction assumptions of 100% and 17%, the latter based on eliminating half of linear contrails and leaving other cirrus effects unchanged. Finally, the 0.5% fuel burn penalty applied here is based on fuel loading with foreknowledge of the airspace to be avoided. If CISSLs are detected in flight, rather than predicted, then the fuel penalty is necessarily greater because the extent of airspace to be avoided is unknown. This scenario is modeled by assuming that fuel is loaded as though the entire mission intersects a CISSL, requiring 2.5% extra fuel based on simple scaling. As before, only 20% of the mission intersects a CISSL, consuming 0.5% of the extra fuel and leaving the 2% additional fuel as a reserve penalty.

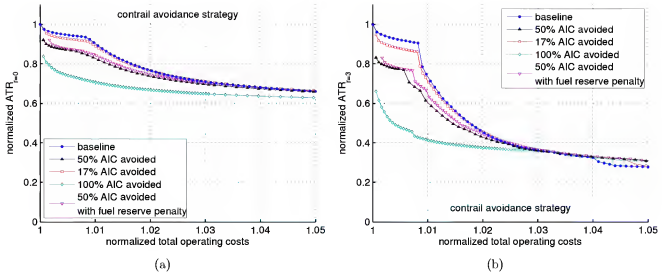


Figure 6.7: Designs optimized for minimum total operating costs and  $ATR_{r=0}$ , applying a contrail avoidance strategy with varying assumptions.

Contrail avoidance with a 50% reduction in AIC impacts produces net ATR savings of 7-15% for low cost designs with almost no effect on total operating costs, as shown in Figure 6.7. Benefits from reduced cloud impacts easily outweigh the negative climate impacts from increased fuel burn, and hence  $CO_2$  and  $NO_x$  emissions. Contrail avoidance designs have effectively lower weighting on AIC impacts, allowing aircraft to cruise nearer to fuel-optimal altitudes and offsetting the operational strategy 0.5% fuel burn penalty. This effect is particularly strong when 100% of AIC impacts are assumed to be avoided, lessening the sensitivity of aircraft climate impacts on design cruise altitude. If only 17% AIC impact savings are achieved,  $ATR_{r=0}$  and  $ATR_{r=3}$  savings are reduced to 2-5%. Lastly, Figure 6.7 also includes results for a detected contrail avoidance strategy, instead of a predictive system. In this case, fuel reserve penalties lead to operating cost increases of 0.1% and an erosion of ATR benefits of less than 1%.

#### 6.4.4 Comparison of Individual Technologies

All of these technologies improve climate performance by reducing fuel burn and/or lowering impacts from CO<sub>2</sub> and NO<sub>x</sub> emissions and cloud formation. Figure 6.8 compares the cost and climate performance of aircraft adopting these individual technologies. The previous section compared results for technologies with varying modeling assumptions; this figure depicts performance with the reference technology assumptions, indicated by black curves on Figures 6.2 through 6.7.

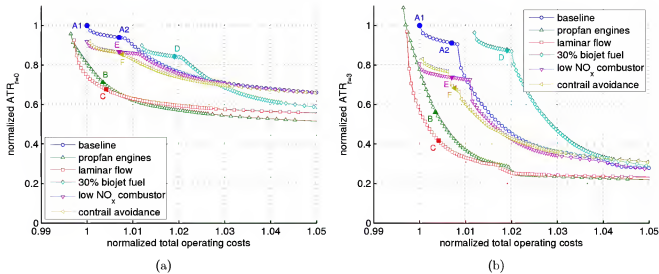


Figure 6.8: Pareto front of normalized total operating cost and ATR with separate low contrails, NO<sub>x</sub>, and fuel burn technologies (each applied individually).

Table 6.5 lists design variables and relative performance for the minimum cost baseline design (A1) in addition to configurations with 0.7% increased operating costs for each technology (A2, B, C, D, E, and F). Designs A2, B, C, D, E, and F have similar design characteristics. Each design employs a swept wing and moderate bypass ratio turbofan engines. These aircraft cruise near Mach 0.77 at altitudes of 39,000 to 40,000 ft, except design F which cruises at 25,000 to 38,000 ft. However, designs D, E, and F have lower climate impacts than design A2, owing to biojet, low NO<sub>x</sub> combustors, and contrail avoidance technologies, respectively. Fuel burn and operating costs are



|   | A1<br>baseline<br>technology | A2<br>baseline<br>technology | B<br>propfan<br>engines | C<br>laminar<br>flow | D<br>biojet<br>fuels | E<br>low NO <sub>x</sub><br>combustor | F<br>contrail<br>avoidance |
|---|------------------------------|------------------------------|-------------------------|----------------------|----------------------|---------------------------------------|----------------------------|
| Maximum TOW [lbs]   | 161,600                      | 159,400                      | 151,100                 | 151,700              | 159,500              | 160,000                               | 157,500                    |
| Typical mission TOW [lbs]   | 140,600                      | 139,600                      | 136,200                 | 135,700              | 139,600              | 140,100                               | 138,000                    |
| Wing area [ft <sup>2</sup> ]  | 1520                         | 1490                         | 1430                    | 1380                 | 1500                 | 1490                                  | 1360                       |
| Wing aspect ratio   | 8.9                          | 9.9                          | 13.6                    | 14.4                 | 9.9                  | 9.9                                   | 10.3                       |
| Wing sweep [degrees]  | 34.0                         | 32.0                         | 21.2                    | 7.0                  | 32.0                 | 31.9                                  | 31.6                       |
| Cruise Mach number  | 0.835                        | 0.772                        | 0.694                   | 0.671                | 0.770                | 0.779                                 | 0.768                      |
| Initial cruise altitude [ft]  | 38,600                       | 39,100                       | 24,300                  | 21,500               | 39,100               | 39,300                                | 25,400                     |
| Final cruise altitude [ft]  | 39,800                       | 40,200                       | 30,000                  | 28,400               | 40,200               | 40,400                                | 37,900                     |
| SLS thrust [lbs]  | 23,200                       | 22,700                       | 26,000                  | 18,400               | 22,800               | 23,100                                | 22,900                     |
| Engine bypass ratio   | 8.4                          | 8.6                          | 60                      | 10.4                 | 8.6                  | 8.6                                   | 9.9                        |
| Avg. cruise velocity [kts]  | 478                          | 442                          | 413                     | 403                  | 441                  | 446                                   | 450                        |
| Normalized TOC  | 1.0000                       | 1.0070                       | 1.0035                  | 1.0042               | 1.0190               | 1.0070                                | 1.0076                     |
| Normalized W <sub>fuel</sub>  | 1.000                        | 0.961                        | 0.848                   | 0.908                | 0.961                | 0.965                                 | 1.005                      |
| Normalized E <sub>NO<sub>x</sub></sub>  | 1.000                        | 0.881                        | 0.893                   | 0.805                | 0.878                | 0.471                                 | 0.966                      |
| Cruise EI <sub>NO<sub>x</sub></sub> [g/kg]                                    | 19.8                         | 17.7                         | 20.9                    | 17.0                 | 17.6                 | 9.4                                   | 18.7                       |
| O <sub>3</sub> forcing factor   | 1.48                         | 1.47                         | 0.76                    | 0.68                 | 1.47                 | 1.48                                  | 0.98                       |
| CH <sub>4</sub> forcing factor  | 1.13                         | 1.12                         | 0.93                    | 0.94                 | 1.12                 | 1.12                                  | 0.98                       |
| AIC forcing factor  | 0.80                         | 0.73                         | 0.57                    | 0.30                 | 0.72                 | 0.71                                  | 1.08                       |
| Normalized ATR <sub>r=0</sub>   | 1.000                        | 0.939                        | 0.712                   | 0.676                | 0.843                | 0.867                                 | 0.854                      |
| Fraction of ATR <sub>r=0</sub> from CO <sub>2</sub> /NO <sub>x</sub> /AIC [%] | 65/17/17                     | 67/16/16                     | 78/5/17                 | 88/2/9               | 63/18/18             | 73/10/17                              | 77/9/13                    |
| Normalized ATR <sub>r=3</sub>   | 1.000                        | 0.911                        | 0.562                   | 0.417                | 0.874                | 0.738                                 | 0.684                      |
| Fraction of ATR <sub>r=3</sub> from CO <sub>2</sub> /NO <sub>x</sub> /AIC [%] | 24/41/34                     | 25/39/35                     | 36/19/44                | 51/16/31             | 22/41/36             | 31/26/41                              | 35/30/34                   |

Table 6.5: Description of aircraft designed for minimum total operating costs and ATR<sub>r=0</sub> with individual climate impact reduction technologies.

also similar between these designs with the exception of design D, which is penalized by higher biojet fuel prices.

Configurations B and C have considerably lower fuel consumption than baseline technology designs. More efficient, dual rotor propfan engines allow design B to consume 11% less fuel than design A2 and 15% less than A1. The propfan design also

cruises at a slower Mach 0.69, the net effect being a 0.4% increase in total operating costs relative to A1. In addition to fuel and CO<sub>2</sub> emissions savings, design B cruises at less sensitive altitudes between 24,000 and 30,000 ft, yielding ATR reductions of 29-44% relative to the reference design. Design C employs natural laminar flow to save more than 5% in fuel consumption relative to design A2, while flying at altitudes between 22,000 and 28,000 ft. Fuel burn savings translate directly into CO<sub>2</sub> impact reductions, and lower altitude flight enables NO<sub>x</sub> and AIC impact savings. Configuration C achieves the lowest ATRs of the aircraft described in Table 6.5.

#### 6.4.5 Combination of Technologies

The previous section assessed the climate benefits and economic impacts of separate technologies. However, these technologies are compatible and may be employed simultaneously. Figure 6.9 shows the cumulative effects of climate impact reduction technologies on the cost-climate impact tradeoff. As before, each point on the figure represents an individual design, optimized to minimize a balance of total operating costs and ATR<sub>r=0</sub> with different applications of technology. The combination of prop-fan engines and natural laminar flow enables large reductions in fuel consumption that translate into total operating cost reductions of more than 1%. Additionally, savings in ATR<sub>r=0</sub> and ATR<sub>r=3</sub> of 20-40% and 10-50% are attained, depending primarily on design cruise altitude. The addition of a contrail avoidance strategy buys another 20-30% reduction in climate impacts for lowest cost designs at almost no penalty to operating costs. Application of low NO<sub>x</sub> combustors reduces ATR a further 3-7%, shown as the black curve on Figure 6.9. Because of reductions in NO<sub>x</sub> and AIC impacts from technology and altitude changes, climate impacts from designs on the black curves are dominated by CO<sub>2</sub> emissions. To achieve even greater climate impact reductions, low carbon intensity alternative fuels can be utilized, shown on the figure by the gray curve. These second generation biofuels can be used by the entire aircraft fleet to offset impacts from CO<sub>2</sub> emissions, but they may cost more to produce than conventional fuels. As previously mentioned, fuel with an 8% higher price and 15% lower life cycle carbon intensity is applied. Higher fuel prices cancel out much of

the operating cost benefits of efficient propfan engines and laminar flow, but lead to further ATR reductions of 2-7%.

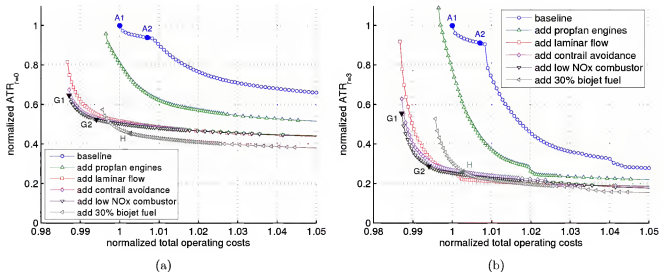


Figure 6.9: Pareto front of normalized total operating cost and ATR with combinations of low contrails,  $\text{NO}_x$ , and fuel burn technologies.

The relative climate benefits of each technology depend on the order in which technologies are applied. This sensitivity is most apparent for low  $\text{NO}_x$  combustors, whose climate benefits are significant when applied in isolation and modest when applied on an aircraft with propfan engines and natural laminar flow wings, as shown in Figures 6.8 and 6.9. Similarly, the individual climate impact reductions enabled by biofuels and fuel efficiency technologies are greatest when added before other  $\text{CO}_2$  mitigation technologies. Nonetheless, each technology offers significant potential for reducing aircraft climate impacts whether applied individually or in combination with other mitigation strategies.

Design variables and performance data for two reference baseline technology and three combined technology designs are listed in Table 6.6. Each combined technology design utilizes a high aspect ratio wing with very low sweep, limited by natural laminar flow constraints. Drag savings create a lower thrust requirement, enabling moderately sized propfan engines to be mounted on the aft fuselage more efficiently.

The lowest cost design, G1, cruises at conventional altitudes of 30,000-35,000 ft while still realizing 35% lower  $ATR_{r=0}$  and 45% lower  $ATR_{r=3}$  than the reference aircraft. Fuel burn savings of nearly 30% offset the increase costs from cruising at a 16% slower speed, enabling a net operating cost reduction of 1.3%. Design G2 flies at lower altitudes and speeds, eliminating about three-quarters of remaining AIC impacts and one-third of  $NO_x$  impacts. Flight at lower altitudes leads to 1% higher fuel burn and 0.7% higher operating costs for G2 compared with G1. Configurations G2 and H have similar layouts, but reductions in  $CO_2$  impacts via biofuels result in total  $ATR_{r=0}$  and  $ATR_{r=3}$  savings for design H of 55% and 74%, respectively.

Substantial reductions in climate impacts on the order of 40% to 75% are possible for future aircraft relative to conventional designs with simultaneous improvements in economic performance. These environmental savings result from the application of climate impact reduction technology and design for flight in regions of the atmosphere that are less radiatively sensitive to aircraft emissions. Moderate reductions in speed and altitude bolster climate benefits by lowering emissions rates and by decreasing the magnitude of temperature change per unit emissions. Flight at lower cruise speeds is particularly compatible with fuel efficient propfan engines and natural laminar flow wing design, allowing for operating cost reductions of more than 1% at a fuel price of \$2.25 per gallon. Remaining impacts from  $CO_2$ ,  $NO_x$ , and AIC are targeted by low emissions combustor design, contrail avoidance, and alternative fuel use. Moreover, the use of biofuels and operational contrail avoidance strategies do not require redesign of aircraft and may be applied to existing aircraft to reduce overall fleet climate impacts.

#### 6.4.6 Assessment of Climate Impact Uncertainty

Considerable uncertainty exists in estimating climate impacts from aircraft emissions and other sources. Climate impact uncertainty is quantified by performing Monte Carlo analysis, which relies on a large number of trials of calculating ATR with random values from each climate model parameter's probability distribution (listed in

|  | A1<br>baseline<br>technology | G1<br>combined<br>technologies | G2<br>combined<br>technologies | H<br>added biojet<br>fuels |
|--|------------------------------|--------------------------------|--------------------------------|----------------------------|
| Maximum TOW [lbs]  | 161,600                      | 151,000                        | 146,100                        | 146,100                    |
| Typical mission TOW [lbs]  | 140,600                      | 137,500                        | 134,400                        | 134,400                    |
| Wing area [ft <sup>2</sup> ]   | 1520                         | 1610                           | 1520                           | 1520                       |
| Wing aspect ratio  | 8.9                          | 14.9                           | 16.9                           | 16.8                       |
| Wing sweep [degrees]   | 34.0                         | 7.0                            | 7.0                            | 7.0                        |
| Cruise Mach number   | 0.835                        | 0.690                          | 0.632                          | 0.633                      |
| Initial cruise altitude [ft]   | 38,600                       | 30,000                         | 21,300                         | 21,300                     |
| Final cruise altitude [ft]   | 39,800                       | 34,900                         | 29,200                         | 29,100                     |
| SLS thrust [lbs]   | 23,200                       | 22,300                         | 20,900                         | 21,000                     |
| Engine bypass ratio  | 8.4                          | 60                             | 60                             | 60                         |
| <hr/>  |                              |                                |                                |                            |
| Avg. cruise velocity [kts]   | 478                          | 402                            | 379                            | 380                        |
| Normalized TOC   | 1.0000                       | 0.9871                         | 0.9941                         | 1.0027                     |
| Normalized W <sub>fuel</sub>   | 1.000                        | 0.714                          | 0.726                          | 0.728                      |
| Normalized E <sub>NO<sub>x</sub></sub>   | 1.000                        | 0.375                          | 0.380                          | 0.383                      |
| Cruise EI <sub>NO<sub>x</sub></sub> [g/kg]   | 19.8                         | 10.4                           | 10.3                           | 10.3                       |
| O <sub>3</sub> forcing factor  | 1.48                         | 0.99                           | 0.71                           | 0.70                       |
| CH <sub>4</sub> forcing factor   | 1.13                         | 0.96                           | 0.94                           | 0.94                       |
| AIC forcing factor   | 0.80                         | 1.37                           | 0.34                           | 0.33                       |
| Normalized ATR <sub>r=0</sub>  | 1.000                        | 0.646                          | 0.524                          | 0.453                      |
| Fraction of ATR <sub>r=0</sub> from<br>CO <sub>2</sub> /NO <sub>x</sub> /AIC [%]   | 65/17/17                     | 72/5/22                        | 91/2/7                         | 89/2/8                     |
| Normalized ATR <sub>r=3</sub>  | 1.000                        | 0.555                          | 0.287                          | 0.261                      |
| Fraction of ATR <sub>r=3</sub> from<br>CO <sub>2</sub> / NO <sub>x</sub> / AIC [%] | 24/41/34                     | 30/15/53                       | 59/12/25                       | 56/13/28                   |

Table 6.6: Description of aircraft designed for minimum total operating costs and ATR<sub>r=0</sub> with multiple climate impact reduction technologies.

Chapter 5). A sufficient number of trials are computed so that the output distributions converge. All model parameters and forcing factor functions are assumed to be uncertain except the climate sensitivity parameter  $S$ , applied in equation (5.15). This parameter is simply a scaling factor that is applied to all calculations of ATR and its uncertainty is not relevant for comparing relative impacts of different designs. For

each Monte Carlo trial, ATR is calculated for all designs using the same set of random model parameter values. From the Monte Carlo analysis, the probability distribution of the *reduction* in average temperature response,  $ATR_{ref} - ATR$ , is examined. By quantifying the uncertainty in the ATR reduction of each design as opposed to the uncertainty in the absolute ATR of each design, only the uncertainty relevant to the differences between the designs is captured. Uncertainty in ATR reduction is more appropriate for comparative study. For example, if two aircraft have identical fuel burn and fly at identical altitudes but have different  $NO_x$  emissions indices, the uncertainty in ATR reduction between the two designs solely depends on uncertainty in components of the climate model related to  $NO_x$  impacts. If, on the other hand, the uncertainty in absolute ATR is examined, uncertainty in all components of the climate model ( $CO_2$ , AIC, etc.) is included; a large portion of this uncertainty affects both designs equally and is extraneous in a comparative study.

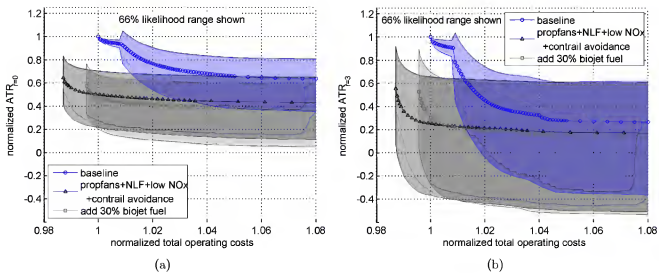


Figure 6.10: Pareto front of normalized total operating cost and ATR, showing 66% confidence intervals for reduction in ATR relative to the reference design.

Figure 6.10 shows 66% likelihood ranges for reductions in ATR relative to the reference aircraft, design A1. The pareto curves shown on this figure are identical to those shown in Figure 6.9. Uncertainty ranges for each design reflect scientific

uncertainty in evaluating climate impacts and do not include uncertainty in estimating aircraft performance. These 66% likelihood ranges are not symmetric about the best estimate values. Instead, very large ATR reductions are more probable than very small reductions. This is the case because the most significant differences between the reference and low climate impact configurations lie in NO<sub>x</sub> and AIC impacts; the radiative forcing parameters for both of these effects are lognormally distributed, which leads to higher probability of large savings for lower altitude flight.

Beginning with the baseline technology scenario, ATR reduction uncertainty is small for lowest cost designs because these configurations are fundamentally similar to the reference aircraft. For baseline designs flying at lower altitudes, ATR reduction uncertainty increases substantially since low altitude configurations achieve ATR savings by reducing impacts from NO<sub>x</sub> and AIC effects, which are highly uncertain. Since ATR<sub>r=3</sub> applies heavier weighting to less certain, short-lived impacts, uncertainty is greater for ATR<sub>r=3</sub> than ATR<sub>r=0</sub>. Nonetheless, the baseline technology shaded region for nearly all designs remains below the unity ATR line, indicating that there is at least an 83% confidence that these aircraft perform with lower ATR than the reference aircraft. Uncertainty ranges for configurations using reduced climate impact technologies are slightly wider. However, because these designs have lower best estimate ATRs, there is greater confidence that they achieve significant climate impact reductions relative to the reference aircraft. Figure 6.10 demonstrates that scientific uncertainty is not too large to make conclusions about the relative climate performance of competing designs.

Probability distributions for most climate model parameters are based on analyses and expert opinions from climate modeling literature. For parameters where this information is not available, probability distributions are inferred from the results of multiple global climate model studies. Changes in the assumed distributions of individual parameters would alter probability distributions in ATR reductions. For example, beta or normal distributions could be assumed for each parameter. Beta and uniform probability distributions are each bounded on both sides, unlike the normal and lognormal distributions applied here, which are bounded on zero and one side, respectively. If beta distributions were applied, moderately narrower uncertainty

ranges in ATR reductions would be expected due to the additional domain bounding. Similarly, significantly wider uncertainty ranges for climate model outputs would be expected using uniform distributions (unless restrictive bounds are applied). It should be noted, however, that with current scientific understanding, climate model parameters are most appropriately described by normal and lognormal distributions because of their unboundedness and because higher probabilities are assigned to parameter values close to best estimates.

Next, the effect of the background CO<sub>2</sub> scenario uncertainty is considered. As noted before, the CO<sub>2</sub> radiative forcing model used here assumes constant background CO<sub>2</sub> concentrations of 378 ppmv. However, it is likely that concentrations will vary and exceed this value in the near-term. To assess this uncertainty, results from the CO<sub>2</sub> forcing models applied herein and in Ref. [53] are compared for aircraft climate impacts assessed in Ref. [73]. For the alternative model, background CO<sub>2</sub> concentrations are taken from Table VIII of Ref. [53] for the years 2000 to 2100, with stable concentrations after 2100 of 685 ppmv. With a devaluation rate of 3%, relative ATR estimates from the constant and varying CO<sub>2</sub> concentration models are nearly identical. Differences of less than 0.3% are observed in relative ATR and fractional CO<sub>2</sub> contributions. Results differ more significantly with a devaluation rate of zero. The relative ATRs of low climate impact designs are 4-10% lower when calculated with varying background CO<sub>2</sub> concentrations. The fractional contributions of CO<sub>2</sub> are also lower with this alternative model. There are two observations worth noting about these results. First, the assumed scenario for background CO<sub>2</sub> concentrations is much more important for zero devaluation rates because all CO<sub>2</sub> far future impacts are included. Secondly, the assumption of varying background concentrations diminishes the impacts of future aircraft CO<sub>2</sub> emissions (only in the case of  $r = 0$ ) because as background concentrations increase, each unit of CO<sub>2</sub> emissions causes a smaller fractional increase in atmospheric CO<sub>2</sub>.

## 6.5 Alternative Metrics

Thus far, climate performance has been measured by the average temperature response metric, developed for use in aircraft design studies. However, many other climate metrics have been suggested for use in studies of impacts from aviation and other sectors. This section addresses the extent to which choice of metric affects conclusions about low climate impact aircraft design.

### 6.5.1 Comparison to Results with CO<sub>2</sub>-Based Metric

Some proposed metrics rely exclusively on CO<sub>2</sub> emissions and are similar to fuel consumption metrics. For example, ICAO's Committee on Aviation Environmental Protection is pursuing a CO<sub>2</sub> emissions standard for future aircraft.[23] With CO<sub>2</sub>-based metrics, the impacts of NO<sub>x</sub> emissions and AIC effects are either excluded or modeled through a simple CO<sub>2</sub> emissions scaling factor. One hundred year pulse global temperature potential-based metrics are effectively similar to CO<sub>2</sub>-based metrics because only the impacts of CO<sub>2</sub> emissions are experienced long after emissions cease, as demonstrated in Ref. [123].

Figure 6.11 shows optimization results for aircraft designed to minimize CO<sub>2</sub> emissions and operating costs with varying technologies. These designs' climate impacts as measured by ATR<sub>r=0</sub> and ATR<sub>r=3</sub> are also plotted. Propfan, laminar flow, and biofuel technologies are applied to these designs to reduce CO<sub>2</sub> impacts. Strictly speaking, low NO<sub>x</sub> combustor application would not be encouraged by CO<sub>2</sub>-based climate standards; however, it is possible that future improvements in emissions performance will be mandated by more stringent landing and takeoff emissions standards, so the effects of ultra low NO<sub>x</sub> combustors are also included. Burning extra fuel to operationally avoid contrail formation would be disincentivized within a CO<sub>2</sub> metric framework, so this strategy is not included. For the baseline technology scenario, reductions in CO<sub>2</sub> emissions of up to 12% are achieved, translating into 2-5% lower ATR<sub>r=0</sub> and 2-5% higher ATR<sub>r=3</sub>, similar to the minimum fuel burn design described in Table 6.3. Fuel burn savings do not directly scale with ATR savings because of the sensitivity of NO<sub>x</sub> and AIC impacts to changes in cruise altitude. By applying propfan engines,

laminar flow, low emissions combustors, and biojet fuel, CO<sub>2</sub> emissions savings of up to nearly 50% are possible. Measuring climate impacts instead with ATR, savings drop to 20-30%, depending on the metric devaluation rate. These aircraft cruise at altitudes of 30,000-36,000 ft where CO<sub>2</sub> impacts are minimized, but NO<sub>x</sub> impacts are high and AIC impacts are maximized. To compare, aircraft designed to minimize ATR perform with 40-60% lower ATR<sub>r=0</sub> and 50-85% lower ATR<sub>r=3</sub> relative to the same reference aircraft. These greater ATR savings are achieved through moderate changes to design cruise altitude and application of a contrail avoidance strategy.

These results demonstrate the disparity in climate impact performance between aircraft designed to minimize CO<sub>2</sub> emissions and those designed for minimal temperature change from all emissions. It is possible that if aircraft are designed exclusively to reduce CO<sub>2</sub> emissions, temperature change from NO<sub>x</sub> emissions and aviation induced cloudiness may increase, offsetting some of the benefits of reduced carbon. Significantly lower lifetime average temperature change can be achieved by considering impacts from non-CO<sub>2</sub> emissions during the design and operation of an aircraft. However, it should be noted that these temperature change impacts occur over very different timescales, with a fraction of CO<sub>2</sub>-induced temperature change remaining in the atmosphere for hundreds of years and NO<sub>x</sub>-induced and AIC-induced temperature change decaying decades after emissions end.

### 6.5.2 Comparison to Results with Other Metrics

Average temperature response is proposed as a climate metric for the application of aircraft design. However, other metrics could be developed to serve the same purpose, as discussed in Chapter 3. Such alternative metrics include average radiative forcing response (analogous to average temperature response) and 30 year sustained temperature change. Each of these metrics quantifies the overall lifetime impacts from all emissions released during the operation of a particular aircraft. Varying the metric or the weighting function effectively adjusts the relative importance of long-lived CO<sub>2</sub> emissions versus shorter-lived effects. Furthermore, metrics that are less appropriate for aircraft design studies could also be considered: examples include radiative forcing,

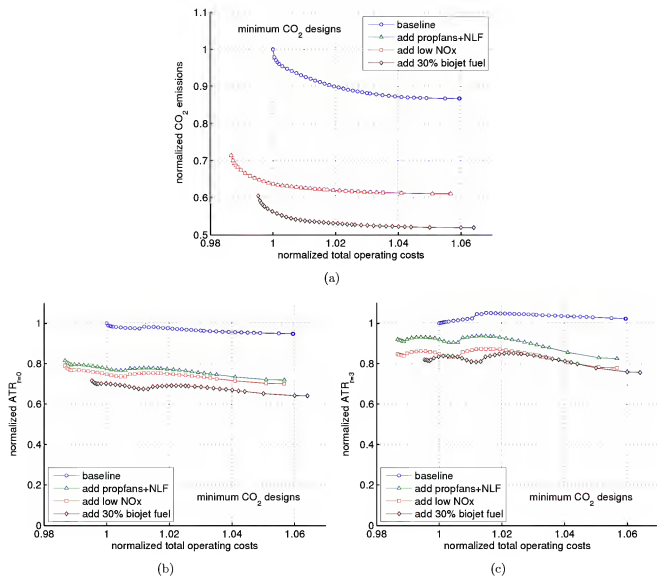


Figure 6.11: Pareto front of normalized total operating cost and  $\text{CO}_2$  emissions with climate impact reduction technologies. Evaluations of  $\text{ATR}_{r=0}$  and  $\text{ATR}_{r=3}$  are also shown.

temperature change, or damage metrics based on past aviation impacts (e.g., scaling RF in 2005 based on new emissions rates) or future emissions scenarios that poorly represent the likely operation of a new aircraft (e.g., 100 year sustained global warming or temperature potentials). Varying the choice of metric and its weighting function causes changes in the magnitude of potential climate impact reductions. However, the conclusions about strategies and design methods to reduce climate impacts remain the same, except near the limiting case of metrics that exclude non-CO<sub>2</sub> impacts or model these effects by scaling CO<sub>2</sub> emissions (e.g., CO<sub>2</sub> metrics and long period pulse global warming or temperature potentials), as explored in section 6.5.1. These findings are demonstrated in Ref. [73] and illustrated by the similarities in Figures 6.1(a) and 6.1(b).

## 6.6 Additional Studies

The effects of climate model uncertainty are addressed in section 6.4.6. However, other assumptions also impact aircraft performance predictions, and in particular total operating cost estimates. This section explores the effect of fuel price and mission range assumptions on the design tradeoff between operating costs and climate impacts.

### 6.6.1 Effect of Varying Fuel Prices

Fuel prices are extremely volatile, so predictions of future prices are speculative. Additionally, operating costs are sensitive to fuel price, affecting the balance between requirements for short flight times and low fuel consumption for cost effective aircraft. As fuel prices increase, technologies and strategies aimed at reducing fuel burn become more economical. Thus, fuel price affects the economic competitiveness of reduced climate impact aircraft. The tradeoffs between operating costs and climate impacts are evaluated under two alternative fuel price scenarios: \$1.50 per gallon and \$3.50 per gallon, representative of the lowest and highest quarterly average aviation fuel prices since 2005.[151] Optimization results are shown in Figure 6.12.

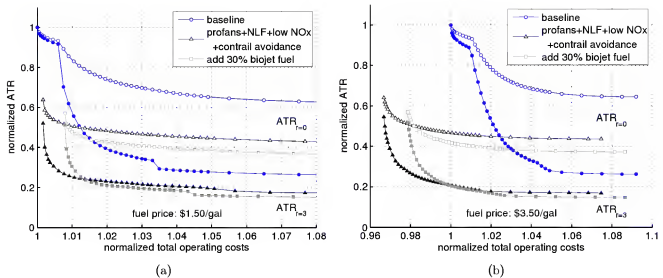


Figure 6.12: Pareto front of normalized total operating cost and ATR with mitigation technologies and lower (left) and higher (right) fuel prices.

Variation in fuel price causes advanced technology, pareto optimal designs to shift in total operating costs relative to baseline technology. For fuel prices as low as \$1.50 per gallon, the economic benefits of reduced fuel burn from propfan engine and laminar flow technology are eliminated. Increased costs from slower flight times outweigh savings from lower fuel costs. Even with these low fuel prices, climate impact reductions on the order of 45-65% can be realized with 0.3% higher total operating costs. For fuel prices of \$3.50 per gallon, the benefits of propfans and laminar flow are enhanced, enabling total operating cost reductions of more than 3%. Based on this analysis, it can be concluded that ultra low climate impact aircraft configurations also achieve total operating cost savings for a wide range of future fuel prices.

### 6.6.2 Effect of Varying Mission Range

For each of the previous studies, aircraft are optimized over a 1000 nmi, typical mission. However, these aircraft are sized to carry the design payload over a range of 3000 nmi. The effects of changes to speed and fuel consumption on costs vary between short and long range missions. Figure 6.13 contains results for aircraft optimized on a

longer range, 2800 nmi mission. Improvements in fuel efficiency from propfan engines and laminar flow enable similar operating cost reductions for short and longer range missions. However, operating costs are more sensitive to changes in design cruise altitude on longer range missions, indicated by the difference in pareto curve slope for low cost designs. As a result, aircraft flying at very low altitudes have worse economic performance during longer range missions. Nonetheless, with advanced technology and moderate altitude changes,  $ATR_{r=0}$  and  $ATR_{r=3}$  reductions of 50% and 70% are possible with 1% lower operating costs than the reference, baseline aircraft for short and medium range missions.

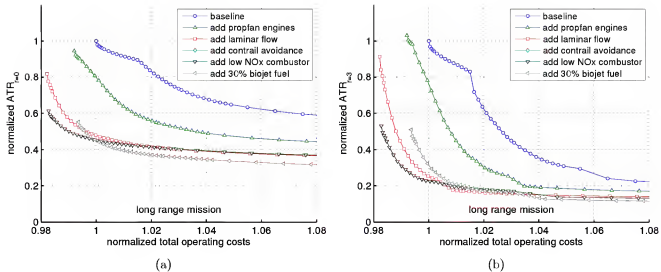


Figure 6.13: Pareto front of normalized total operating cost and ATR with designs optimized over a long range mission.

## 6.7 Mitigation Strategies for Existing Aircraft

This chapter focuses on methods to reduce climate impacts of future aircraft. But because commercial aircraft have long operating lifetimes, many aircraft flying today will still be operating in 20 years.[3] To substantially improve climate performance of the entire fleet, mitigation strategies for both new and existing aircraft are necessary.

Several of the strategies investigated for future aircraft are also applicable to existing aircraft, including cruise altitude adjustments, operational contrail avoidance, and use of biojet fuels. Relative performance impacts of mitigation strategies are estimated by assessing the cost-climate impact tradeoff for a fixed geometry, conventional aircraft. In the optimization, only cruise speed, altitudes, and typical mission takeoff weight are allowed to vary, and the configuration layout is based on the reference, minimum cost design A1. Figure 6.14 shows optimization results for cumulative application of these strategies, noting that each point on a fixed design curve represents configuration A1, operated at a different speed and altitude. For clarity, the baseline pareto curve of new designs is also shown where each point represents a different configuration with unique design parameters.

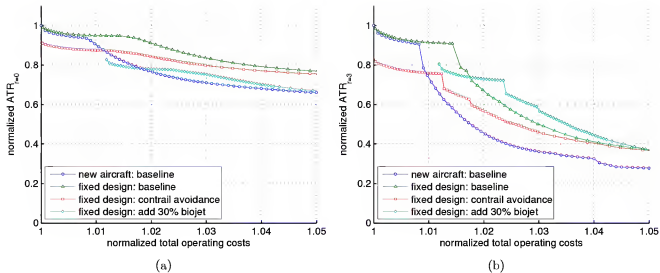


Figure 6.14: Pareto front of normalized total operating cost and ATR for designs with fixed configuration parameters representing conventional aircraft in the current fleet.

Nearly equal climate benefits from reduced speed and altitude can be achieved by conventional, existing aircraft compared with newly designed aircraft. However, such climate savings for existing aircraft are associated with larger fuel and operating cost penalties. An aircraft designed for lower speed flight can use a wing with lower sweep and higher aspect ratio, but a fixed geometry aircraft flying at slower speeds

cannot benefit from these weight and drag savings. Additionally, the fixed geometry conventional aircraft has a very large wing, leading to low, less aerodynamically efficient lift coefficients at reduced altitudes, unlike aircraft designed for low altitude flight that employ smaller wings. It should also be noted that operating an existing aircraft away from intended cruise altitudes increases fuel burn, thereby decreasing maximum range. For instance, operating design A1 at Mach 0.80 and altitudes of 24,000-31,000 ft limits maximum range to 2600 nmi (while at the same time reducing typical mission  $ATR_{r=0}$  and  $ATR_{r=3}$  by 10% and 33%, respectively). The adoption of operational contrail avoidance and biofuels enables large reductions of at least 20% in  $ATR_{r=0}$  and  $ATR_{r=3}$  at conventional cruise altitudes, similar to the benefits realized by newly designed aircraft. In total, the combination of these strategies allows for significant improvements in climate performance of existing aircraft, but the associated cost penalties are approximately twice as high as those for new aircraft with comparable technology adoption.

# Chapter 7

## Conclusions and Future Work

### 7.1 Conclusions

The objective of this research was to develop a framework for assessing the comparative climate impacts of different aircraft during conceptual design studies. Aircraft emit numerous radiatively active species, each affecting the atmosphere over different timescales. A linear climate model encompassing each of these effects and appropriate for initial aircraft design studies was presented. This model accounted for the variation in magnitudes of  $\text{NO}_x$  and aviation induced cloudiness radiative forcings as functions of emissions altitude. Design cruise altitude additionally affects aircraft fuel consumption and  $\text{NO}_x$  emission rates, and these dependencies were modeled simultaneously by integrating the climate model into an aircraft design and performance estimation tool. The average temperature response metric was developed to meaningfully quantify an aircraft's lifetime operating climate change impacts. Lastly, the uncertainty of individual model parameters was assessed to determine the level of confidence in estimates of relative climate performance between competing aircraft configurations.

Applying this framework, aircraft climate impact mitigation strategies were investigated. The powerful effect of design cruise altitude on climate impacts was demonstrated, showcasing the potential for net climate impact reductions of 10-35% by designing aircraft to fly at Mach 0.77 and 25,000-31,000 ft altitude (with 1% higher

operating costs) when compared with more conventional designs that cruise at Mach 0.84, 39,000-40,000 ft altitude. The performance effects of climate impact reduction technologies were modeled, including adoption of propfan engines, design for natural laminar flow, replacement of conventional fuels with biofuels, use of low NO<sub>x</sub> combustors, and development of an operational contrail avoidance strategy. Aircraft flying below fuel-optimal altitudes incurred a fuel burn penalty, but propfan and laminar flow technologies were applied to offset these penalties and produce large fuel savings. Combining the effects of all technologies, climate impact savings on the order of 45% in ATR<sub>r=0</sub> and 70% in ATR<sub>r=3</sub> were predicted along with total operating cost savings of 0.6% relative to a conventional, baseline technology, minimum cost aircraft. Greater ATR reductions of 55% and 74% were predicted by applying biofuels, but these designs were penalized by higher fuel prices.

Large uncertainties exist in estimating the climate impacts of aircraft. An uncertainty quantification study was performed, which revealed that this scientific uncertainty is not too great to make conclusions about the relative climate performance of competing designs. Two-thirds likelihood ranges for ultra low climate impact designs estimated ATR<sub>r=0</sub> reductions of 28-75% (best estimate 46%) and ATR<sub>r=3</sub> reductions of 31-131% (best estimate 68%) relative to the reference aircraft. A separate source of uncertainty in this study related to fuel prices. The economic benefits of low fuel burn technologies, including propfan engines and natural laminar flow, were sensitive to variation in fuel prices. However, the financial benefits of these technologies were shown to be robust to these sensitivities: low climate impact configurations with multiple technologies achieved lower operating costs than a conventional, minimum cost aircraft with baseline technology for fuel price scenarios of approximately \$1.60 per gallon and higher.

In this study, climate impacts were measured by the average temperature response metric, developed for the application of comparative aircraft design studies. This metric assessed the integrated, total temperature change produced by operation of a particular aircraft. If instead, aircraft were designed to minimize CO<sub>2</sub> emissions, CO<sub>2</sub> reductions of up to 45% are possible. However, because the effects of NO<sub>x</sub> and

AIC were excluded from design consideration, maximum  $ATR_{r=0}$  and  $ATR_{r=3}$  reductions were limited to 30% and 20%, respectively. Comparable technology low ATR designs achieved reductions of 50% and 75%, respectively, through design consideration of non-CO<sub>2</sub> impacts and application of operational contrail avoidance. These results illustrated the importance of including non-CO<sub>2</sub> emissions in an aircraft climate metric.

Finally, this research focused on the design of new aircraft. However, since commercial aircraft have long operating lifetimes on the order of 30 years, reductions in climate impacts from existing aircraft were necessary to improve fleetwide climate performance. By flying existing aircraft at cruise altitudes that were less radiatively sensitive and applying operational contrail avoidance and alternative fuels,  $ATR_{r=0}$  and  $ATR_{r=3}$  reductions of up to 20-30% and 40-60% were realized, with associated operating cost increases of 2-5%. Thus, while significant climate impact reductions were possible with existing aircraft, the economic penalties were much greater than those for new reduced climate impact designs.

## 7.2 Future Work

This research established a framework for assessing the climate impacts of future aircraft and quantified the climate benefits and economic impacts of various mitigation strategies. A number of research opportunities exist to continue this work.

One area with potential for research advancement involves linear climate model development. Further studies of aircraft climate impacts, most notably aviation induced cloudiness, are needed to improve the accuracy of conceptual design climate models. The AIC radiative forcing parameterization can be updated to include sensitivities to engine exhaust temperature and water content. Furthermore, forcing factors developed for this research were based on results from a single global climate model study. Additional global climate model studies are necessary to improve understanding of the variation in NO<sub>x</sub> and AIC radiative forcings with altitude, and additionally, latitude. Similarly, the diurnal and seasonal variation in AIC forcing factors could be

quantified. With these model advancements, climate assessments can be performed over more realistic time-dependent and three-dimensional flight routings.

This research revealed an opportunity for significant aircraft climate impact reductions via design cruise altitude changes. However, it is likely that aircraft flying at lower altitudes will encounter more turbulence, affecting cruise wing loading, airframe maintenance, and passenger comfort. Operating many aircraft in the 25,000-30,000 altitude band may also lead to increased airspace congestion. More research is needed to investigate the effects of operating both existing and future aircraft at moderately lower cruise altitudes compared with conventional commercial fleet routing.

A mitigation strategy assessed here was operational contrail avoidance, first proposed by Mannstein et al.[147] For this strategy to be viable, advancements in humidity sensors, weather forecasting, and flight planning are necessary. Further investigation of the horizontal extent of contrailing ice-supersaturated layers is needed to determine the feasibility of this operational strategy. In particular, if individual CISSLs are too small in horizontal scope or if the height of a typical CISSL meanders horizontally, meaning that its average altitude varies by thousands of feet within its horizontal extent, then the model of contrail avoidance through a single  $\pm 2000$ -4000 ft shift may not be sufficient to reduce AIC impacts. Additionally, future research should consider how this type of strategy can be integrated into air traffic management systems without exceeding realistic traffic congestion and controller workload limits.

The benefits of low  $\text{NO}_x$  combustors were estimated in this research based on simple technology factors. Future advanced technology combustor design will likely involve tradeoffs between emission rates of  $\text{NO}_x$  and other species, combustion efficiency, and configuration weight. Higher fidelity, physics-based models are needed to answer questions about combustor design for minimal operating costs and climate impacts.

Estimates of operating costs in this research were based on current, typical airline operating expenses. However, it is likely that in the next decade, taxes and regulations could be introduced with the goal of limiting future aircraft climate change. As demonstrated in Chapter 6, studies of aircraft designed to minimize  $\text{CO}_2$  emissions

versus average temperature response yielded different climate performance levels and solution strategies. Future studies could consider the impacts of proposed policy changes on the conclusions of aircraft design studies.

Aircraft design studies in this research were limited to conventional fuels and tube-wing configurations. Applying climate impact reduction technologies to blended-wing-body aircraft could enable further emissions and climate impact savings. These configurations also provide community noise benefits through airframe shielding and may be well-suited for propfan engine application. The conceptual design methods applied here were derived for traditional configurations; assessment of unconventional aircraft technologies requires the development of appropriate conceptual design and performance methods.

## Appendix A

# Turbofan and Propfan Performance Model

Performance of turbofan and propfan engines, including fuel consumption and available thrust, is estimated with a cycle analysis. In this analysis, the thermodynamic properties of the flow are computed at each station in the engine based on energy relationships. The same cycle analysis is applied for both turbofan and propfan engines, and differences between these configurations are modeled through engine design parameters and efficiencies. Fan efficiencies are predicted using simple propeller theory.

The cycle analysis described herein is based on the methods presented in Refs. [21, 90]. Key assumptions for this engine model are as follows:

- The flow is one-dimensional at each axial station.
- The flow is steady on average.
- The fluid behaves as a perfect gas with constant molecular weights and specific heats both upstream and downstream of the burner.
- High pressure bleed air and engine cooling air are removed after the fluid exits the high pressure compressor, but before the fluid enters the burner.
- Diffusers and nozzles are adiabatic.

- Fan, compressor, and turbine component performance are described by constant polytropic efficiencies.
- Exhaust streams from the core and bypass ducts exit the engine through separate convergent nozzles.
- There is no booster on the low pressure spool.
- Installation penalties are modeled as a constant fractional loss in thrust at all operating conditions.

This cycle analysis models specific fuel consumption and available specific thrust at all flight conditions and throttle settings for an engine with user-specified design variables and component efficiencies. The result is a “rubber engine” whose thrust can be adjusted by scaling mass flow rates.

### Cycle Notation and Component Assumptions

Before describing the model equations, notation and engine station numbering are established. Figure A.1 shows standard station numbering and mass flows for a two-spool, separate exhaust engine. A low pressure spool connects the fan and low pressure turbine, and a high pressure spool connects the high pressure compressor and turbine. Station properties  $\dot{m}$ ,  $M$ ,  $T$ , and  $P$  refer to mass flow, Mach number, temperature, and pressure, respectively. The subscript  $T$  denotes a station stagnation property. The variables  $\tau$  and  $\gamma$  indicate temperature and pressure ratios. Gas properties take on constant but different values upstream and downstream of the burner. For all stations upstream of station 3, the gas constant, specific heat, and ratio of specific heats are denoted  $R_c$ ,  $C_{pc}$ , and  $\gamma_c$ . Corresponding properties downstream of station 4 are given by  $R_t$ ,  $C_{pt}$ , and  $\gamma_t$ . Key parameter relationships at each station are described in the following sections.

*Station 0: Far upstream of the engine entrance* (not shown in the figure). The total mass flow through the engine fan is  $\dot{m}_0$ . Ratios of stagnation to static properties

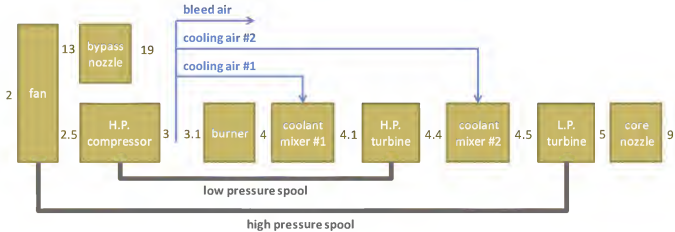


Figure A.1: Diagram of engine station numbering, adapted from Ref. [21].

are given by  $\tau_r$  and  $\pi_r$ .

$$\tau_r = \frac{T_{T0}}{T_0} = 1 + \frac{\gamma_c - 1}{2} M_0^2 \quad \text{and} \quad \pi_r = \frac{P_{T0}}{P_0} = \tau_r^{\frac{\gamma_c}{\gamma_c - 1}} \quad (\text{A.1})$$

*Station 2b and 2c: Fan face.* The bypass ratio,  $\alpha$ , describes the fractions of total mass flow entering the bypass and core streams. Prior to reaching the fan face, the flow may pass through a diffuser. The diffuser is assumed to be adiabatic but not isentropic due to wall friction. In some engines including the propfan, the diffusers for the bypass and core streams may perform differently, so separate parameters are necessary.

$$\dot{m}_{2b} = \frac{\alpha}{\alpha + 1} \dot{m}_0 \quad \text{and} \quad \dot{m}_{2c} = \frac{1}{\alpha + 1} \dot{m}_0 \quad (\text{A.2})$$

$$\pi_{db} = \frac{P_{T2b}}{P_{T0}} \quad \text{and} \quad \pi_{dc} = \frac{P_{T2c}}{P_{T0}} \quad (\text{A.3})$$

*Stations 13 and 2.5: Bypass and core stream fan exit.* The stagnation pressure ratio across the fan is an important design parameter for the engine. The stagnation

temperature ratio is related to fan pressure ratio through fan polytropic efficiency,  $e_f$ , which prescribes the required power input from the low pressure spool to run the fan. Because there are no booster stages on the low pressure spool, the fan pressure ratio for the bypass and core streams are identical. Mass flow rates entering and exiting the fan are equal,  $\dot{m}_{13} = \dot{m}_{2b}$  and  $\dot{m}_{2.5} = \dot{m}_{2c}$ .

$$\pi_f = \frac{P_{T13}}{P_{T2b}} = \frac{P_{T2.5}}{P_{T2c}} \quad \text{and} \quad \tau_f = \frac{T_{T13}}{T_{T2}} = \frac{T_{T2.5}}{T_{T2}} = \pi_f^{\frac{\gamma_c-1}{\gamma_c e_f}} \quad (\text{A.4})$$

*Station 3: High pressure compressor exit.* The stagnation pressure ratio across the high pressure compressor is another key engine design parameter. Similarly to the fan, the performance of the high pressure compressor is described by the compressor polytropic efficiency,  $e_{ch}$ . Mass flow rates at the high pressure compressor entrance and exit are identical,  $\dot{m}_3 = \dot{m}_{2c}$ .

$$\pi_{ch} = \frac{P_{T3}}{P_{T2.5}} \quad \text{and} \quad \tau_{ch} = \frac{T_{T3}}{T_{T2.5}} = \pi_{ch}^{\frac{\gamma_c-1}{\gamma_c e_{ch}}} \quad (\text{A.5})$$

*Station 3.1: Burner entrance.* Between the high pressure compressor exit and the burner entrance, bleed and turbine cooling air are removed.  $\delta_1$  and  $\delta_2$  give cooling air fractions,  $\dot{m}_{ci} = \delta_i \dot{m}_{2c}$ , and  $\beta$  represents the bleed air fraction. Thermodynamic properties are unchanged.

$$\dot{m}_{3.1} = (1 - \beta - \delta_1 - \delta_2) \dot{m}_{2c} \quad (\text{A.6})$$

*Station 4: Burner exit.* The stagnation temperature at the burner exit,  $T_{T4}$ , is a key design variable for an aircraft engine. Increases in  $T_{T4}$  improve overall efficiency, but this parameter is limited by material properties. Across the burner, stagnation pressure drops due to viscous losses and heat addition. The fuel mass added to the flow,  $\dot{m}_f$  is defined by the variable  $f$ .

$$f = \frac{\dot{m}_f}{\dot{m}_{3.1}} \quad \text{and} \quad \dot{m}_4 = (1 - \beta - \delta_1 - \delta_2) (1 + f) \dot{m}_{2c} \quad (\text{A.7})$$

$$\pi_b = \frac{P_{T4}}{P_{T3.1}} \quad (\text{A.8})$$

*Station 4.1: First coolant mixer exit.* Because burner exit temperatures often approach or exceed the melting point of turbine blade materials, cooling flows are necessary. In this coolant mixer, cooler air diverted upstream of the burner is mixed with air exiting the combustor. The pressure change in this mixing process is not modeled, and high pressure turbine polytropic efficiency is penalized to account for the effects of cooling.[21]

$$\dot{m}_{4.1} = [(1 - \beta - \delta_1 - \delta_2)(1 + f) + \delta_1] \dot{m}_{2c} \quad (\text{A.9})$$

*Station 4.4: High pressure turbine exit.* In the high pressure turbine, power is extracted from the flow to drive the high pressure compressor. The efficiency of this process is described by the high pressure turbine polytropic efficiency,  $e_{th}$ , which relates the stagnation temperature and pressure ratios across the turbine. Mass flows at the turbine entrance and exit are equal,  $\dot{m}_{4.4} = \dot{m}_{4.1}$ .

$$\tau_{th} = \frac{T_{T4.4}}{T_{T4.1}} \quad \text{and} \quad \pi_{th} = \frac{P_{T4.4}}{P_{T4.1}} = \tau_{th}^{\frac{\gamma_t}{(\gamma_t - 1)e_{th}}} \quad (\text{A.10})$$

*Station 4.5: Second coolant mixer exit.* The first and second coolant mixers are modeled similarly.

$$\dot{m}_{4.5} = [(1 - \beta - \delta_1 - \delta_2)(1 + f) + \delta_1 + \delta_2] \dot{m}_{2c} \quad (\text{A.11})$$

*Station 5: Low pressure turbine exit.* The low pressure turbine extracts power from the flow to drive the fan. Again, the temperature and pressure ratios through the turbine are related through the low pressure turbine polytropic efficiency,  $e_{tl}$ . Mass flow rates at the turbine entrance and exit are equal,  $\dot{m}_5 = \dot{m}_{4.5}$ .

$$\tau_{tl} = \frac{T_{T5}}{T_{T4.5}} \quad \text{and} \quad \pi_{tl} = \frac{P_{T5}}{P_{T4.5}} = \tau_{tl}^{\frac{\gamma_t}{(\gamma_t - 1)e_{tl}}} \quad (\text{A.12})$$

*Stations 19 and 9: Core and bypass stream nozzle exit.* Both nozzles are assumed to be adiabatic but not isentropic due to wall friction. Nozzle performance is defined by the stagnation pressure ratio. Core exhaust mass flow rate equals the turbine

exit flow,  $\dot{m}_9 = \dot{m}_{4.5}$ , and fan exhaust flow rate is the same as the fan face value,  $\dot{m}_{19} = \dot{m}_{2c}$ .

$$\pi_{nb} = \frac{P_{T19}}{P_{T13}} \quad \text{and} \quad \pi_{nc} = \frac{P_{T9}}{P_{T5}} \quad (\text{A.13})$$

### Cycle Analysis

To perform the cycle analysis and solve for properties at each station, additional equations are introduced that describe how components function together. Five power balance equations relate stagnation temperatures at different stations. These equations represent power balance across the burner (A.14), the high pressure spool (A.15), the low pressure spool (A.16), and the two coolant mixers (A.17 and A.18). Mechanical shaft efficiencies for the high pressure and low pressure spools,  $\eta_{mh}$  and  $\eta_{ml}$ , represent the ratios of power entering the shaft from the turbine to the power leaving the shaft to the compressor. Burner efficiency,  $\eta_b$ , denotes the ratio of thermal energy increase in the flow compared with the ideal energy change based on the fuel heating value,  $h_{fuel}$ .

$$\dot{m}_{3.1} C_{pc} T_{T3} + \dot{m}_f h_{fuel} \eta_b = \dot{m}_4 C_{pt} T_{T4} \quad (\text{A.14})$$

$$\dot{m}_{4.1} C_{pt} (T_{T4.1} - T_{T4.4}) \eta_{mh} = \dot{m}_{2.5} C_{pc} (T_{T3} - T_{T2.5}) \quad (\text{A.15})$$

$$\dot{m}_{4.5} C_{pt} (T_{T4.5} - T_{T5}) \eta_{ml} = \dot{m}_0 C_{pc} (T_{T2.5} - T_{T2}) \quad (\text{A.16})$$

$$\dot{m}_{c1} C_{pc} T_{T3} + \dot{m}_4 C_{pt} T_{T4} = \dot{m}_{4.1} C_{pt} T_{T4.1} \quad (\text{A.17})$$

$$\dot{m}_{c2} C_{pc} T_{T3} + \dot{m}_{4.4} C_{pt} T_{T4.4} = \dot{m}_{4.5} C_{pt} T_{T4.5} \quad (\text{A.18})$$

After solving this system of equations, all station stagnation properties are known. However, static conditions at the engine exhaust plane must also be found to determine thrust. Because both the core and fan bypass streams exit the engine through convergent nozzles, flows at the exit planes may be choked. Exhaust plane conditions are solved via equations (A.19) and (A.20), which enable calculation of  $M_{19}$  and  $M_9$  and hence  $V_{19}$  and  $V_9$ .

$$\frac{P_{T19}}{P_{19}} = \min \left[ \pi_r \pi_{df} \pi_f \pi_{nf}, \frac{\gamma_c + 1}{2}^{\frac{\gamma_c}{\gamma_c - 1}} \right]; \quad (\text{A.19})$$

$$\frac{P_{T9}}{P_9} = \min \left[ \pi_r \pi_{dc} \pi_f \pi_{ch} \pi_b \pi_{th} \pi_{tl} \pi_{nc}, \frac{\gamma_t + 1}{2}^{\frac{\gamma_t}{\gamma_t - 1}} \right]; \quad (A.20)$$

Then, uninstalled thrust,  $F$ , is computed from a momentum balance. Because this analysis describes a rubberized engine, specific thrust,  $\frac{F}{\dot{m}_0}$ , is a useful performance variable.

$$F = \dot{m}_{19} V_{19} + \dot{m}_9 V_9 - \dot{m}_0 V_0 + A_{19} (P_{19} - P_0) + A_9 (P_9 - P_0) \quad (A.21)$$

$$\frac{F}{\dot{m}_0} = \frac{\dot{m}_{19}}{\dot{m}_0} V_{19} + \frac{\dot{m}_9}{\dot{m}_0} V_9 - V_0 + \frac{\dot{m}_{19}}{\dot{m}_0} \frac{R_e T_{19}}{V_{19}} \left(1 - \frac{P_0}{P_{19}}\right) + \frac{\dot{m}_9}{\dot{m}_0} \frac{R_e T_9}{V_9} \left(1 - \frac{P_0}{P_9}\right) \quad (A.22)$$

Installation losses are assumed to cause a constant fractional penalty on available thrust, indicated by the parameter  $\eta_{inst}$ . Installed thrust,  $T$ , is computed from  $F$  via equation (A.23).

$$T = \eta_{inst} F \quad (A.23)$$

Finally, installed thrust specific fuel consumption is found as the ratio of fuel mass flow to installed thrust. Overall efficiency ( $\eta_o$ ), a related quantity, is also computed.

$$sfc = \frac{\dot{m}_f}{T} \quad \text{and} \quad \eta_o = \frac{T V_0}{\dot{m}_f h_{fuel}} \quad (A.24)$$

### Design Point

The engine is designed by performing the cycle analysis at a single operating condition. To compute performance at the design point, several parameters must be specified. These parameters are listed in Table A.1. Key design variables include fan pressure ratio, high pressure compressor pressure ratio, bypass ratio, and burner exit temperature. Each of these variables strongly affects the performance of the engine and can vary significantly between different aircraft engine configurations and technology levels. The design point operating Mach number and altitude,  $M_0$  and  $h_0$ , must also be specified. Typically either sea level static or top of climb conditions are used. Ambient temperature and pressure are computed using the U.S. Standard Atmosphere model. Additional technology parameters include the following: compressor and turbine polytropic efficiencies, burner and shaft efficiencies, component

pressure ratios, and bleed and cooling air fractions. Finally, specification of gas and fuel properties is also required.

| Parameter category      | Variables  |
|-------------------------|--|
| Design variables        | $\pi_f, \pi_{ch}, \alpha, T_{T4}$  |
| Design point conditions | $M_0, h_0$   |
| Technology parameters   | $e_f, e_{ch}, e_{th}, e_{tl},$<br>$\eta_b, \eta_{ml}, \eta_{mh},$<br>$\pi_{db}, \pi_{dc}, \pi_b, \pi_{nb}, \pi_{nc},$<br>$\beta, \delta_1, \delta_2$ |
| Physical parameters     | $h_{fuel}, R_c, C_{pc}, \gamma_c,$<br>$R_t, C_{pt}, \gamma_t$  |

Table A.1: Engine design parameters.

Both bypass ratio and fan pressure ratio are related to the relative mass flow through the fan bypass stream. Instead of specifying both variables, one variable can be determined via optimization. In this model, bypass ratio is specified and fan pressure ratio is optimized to minimize specific fuel consumption.

By solving the equations from the previous section at the design condition, all station properties are known. This information is necessary to compute performance at off design conditions.

### Off Design

Off design analysis enables quantification of both maximum available thrust at different altitudes and flight speeds and specific fuel consumption at varying operating conditions and throttle settings. As before, the off design cycle analysis presented is based on the models in Refs. [21, 90]. This analysis requires the following additional assumptions:

- Turbine and compressor isentropic efficiencies are equal to their design point values. All other technology parameters (except compressor and turbine polytropic efficiencies) equal their design point values.

- The flow is choked at the entrances to both the high pressure and low pressure turbines (stations 4.1 and 4.5).
- Maximum thrust at any operating condition is limited such that neither  $T_{T4}$  nor  $\pi_{ch}$  exceed their design point values.

To apply the first assumption, compressor and turbine polytropic efficiencies,  $e_i$ , must be converted into isentropic efficiencies,  $\eta_i$ , at the design point. The second assumption introduces additional relationships between thermodynamic conditions and design and off design conditions. These equations are described in Refs. [21, 90]. The resulting system of equations is nonlinear and must be solved numerically.

The third assumption establishes a simple engine control system that limits maximum thrust. In this model, high pressure compressor pressure ratio and burner exit temperature are limited to not exceed their design point values. In a real engine, other parameters such as shaft rotational speed, burner entry temperature, and burner pressure are also controlled; however,  $\pi_{ch}$  and  $T_{T4}$  have the most dominant effect in limiting thrust.[90] Burner temperature can be scheduled to allow for different maximum temperatures depending on operating conditions, but a single limit is used for this simple model. Additionally, thrust for unducted engines is limited by maximum blade loading, effectively reducing available thrust at takeoff conditions. The effect of engine throttling at a given flight altitude and speed is modeled by reducing the burner exit temperature below its maximum value (which is limited by either design  $T_{T4}$  or  $\pi_{ch}$ ). Then, specific fuel consumption and thrust may be calculated for partial throttle operation.

### Fan Polytropic Efficiency

Engines with different bypass ratios can be driven by similar engine cores, with the same core component efficiencies. However, the low pressure compressor system efficiencies of a moderate bypass ratio turbofan and a very high bypass ratio propfan can differ significantly. In particular, low pressure spool mechanical efficiency, fan diffuser and nozzle pressure ratios, and fan polytropic efficiency all vary depending

on the fan configuration. This section describes methods to quantify the variation in fan polytropic efficiency with bypass ratio and fan layout.

Fan polytropic efficiency and propulsive efficiency,  $e_f$  and  $\eta_{prop}$ , measure separate quantities. Fan polytropic efficiency describes the entropy rise during compression; propulsive efficiency, on the other hand, is the ratio of useful thrust power to input shaft power. Propulsive efficiency includes axial induced momentum losses while fan polytropic efficiency does not. The approximate relationship between these two efficiencies is given by equation (A.25) as derived in Ref. [152]. The efficiency parameter used in cycle analysis is  $e_f$ , but  $\eta_{prop}$  is used more often in propfan design. In this section, both efficiencies are computed.

$$\eta_{prop} \approx \frac{2V_0}{V_0 + V_{19}} e_f \quad (A.25)$$

Based on one-dimensional cycle analysis, fan specific thrust and power (excluding the core) are related through fan pressure ratio and polytropic efficiency. This analysis is intended to isolate efficiency losses in the fan, and no other losses are modeled. Assuming a fully expanded exhaust and no pressure change in the nozzle and diffuser, specific thrust and power are given by equations (A.26) and (A.27).

$$\frac{F_{fan}}{\dot{m}_{fan}} = \sqrt{\frac{2}{\gamma_c - 1} \left( \pi_f^{\frac{\gamma_c - 1}{\gamma_c}} - 1 \right)} \sqrt{\gamma_c R_c T_0 \pi_f^{\frac{\gamma_c - 1}{\gamma_c} \left( \frac{1}{e_f} - 1 \right)}} - V_0 \quad (A.26)$$

$$\frac{P_{fan}}{\dot{m}_{fan}} = C_{pc} T_0 \tau_r \left( \pi_f^{\frac{\gamma_c - 1}{\gamma_c e_f}} - 1 \right) \quad (A.27)$$

These one-dimensional equations can be combined with propeller analysis methods to determine the polytropic efficiency of a fan with specified thrust based on losses from drag and energy left in the wake. Separate propeller models are presented for single rotation propellers, dual rotation propellers, and rotor-stator configurations. The propeller analysis methods presented are very simple but capture the relative differences in performance between fan designs.

**Single Rotor** The simplest fan configuration for a propfan engine is a single propeller. Single propeller performance can be estimated with a combination of momentum, blade element and vortex theory as described by Glauert.[79] This classical theory is developed for low disk loadings, but is also sufficient for preliminary performance estimates in highly loaded propellers.[153] The related method presented in Ref. [154] is applied for this analysis. This model designs an optimally loaded propeller and computes thrust and efficiency, including losses from swirl, tip effects, and viscous blade drag. With a single row of propeller blades, the swirl losses, or rotational momentum left in the wake, can cause efficiency losses greater than 25%. Because of this, single propeller configurations are only appropriate for relatively low advance ratios. Depending on where the engines are installed on the aircraft, swirl losses can be recovered through simultaneous propeller and wing design.[84, 92]

A diagram of velocities is given in Figure A.2. The propeller induces axial and tangential velocities at the propeller face that are characterized by the dimensionless quantities  $a = \frac{u_a}{V_0}$  and  $a' = \frac{u_t}{\Omega r}$ . Circulation is denoted  $\Gamma$ , the number of blades  $B$ , and the section drag-to-lift ratio  $\epsilon$ . The net resultant force is resolved into thrust in the axial direction and torque in the tangential direction. Thrust and torque per unit radius,  $F'$  and  $Q'$ , are described by equations (A.28), (A.29), (A.30), and (A.31) based on momentum and vortex models.

$$F' = 4\pi r \rho V_0^2 a (1+a) \kappa - B \epsilon \rho \Gamma V_0 (1+a) \quad (\text{A.28})$$

$$F' = B \rho \Gamma \Omega r (1-a') - B \epsilon \rho \Gamma V_0 (1+a) \quad (\text{A.29})$$

$$Q' = B \rho \Gamma V_0 r (1+a) + B \epsilon \rho \Gamma \Omega r^2 (1-a') \quad (\text{A.30})$$

$$Q' = 4\pi r^2 \rho V_0 \Omega r (1+a) a' \kappa + B \epsilon \rho \Gamma \Omega r^2 (1-a') \quad (\text{A.31})$$

In these equations,  $\kappa$  represents the Prandtl loss function, which accounts for momentum loss due to radial flow near the tips.[79] This function is defined in equation (A.32).

$$\kappa = \frac{2}{\pi} \cos^{-1} \left( \exp \left[ \frac{-B (1 - \frac{r}{R})}{2 \sin \phi_{r=R}} \right] \right) \quad \text{where} \quad \tan \phi = \frac{V_0 (1+a)}{\Omega r (1-a')} \quad (\text{A.32})$$

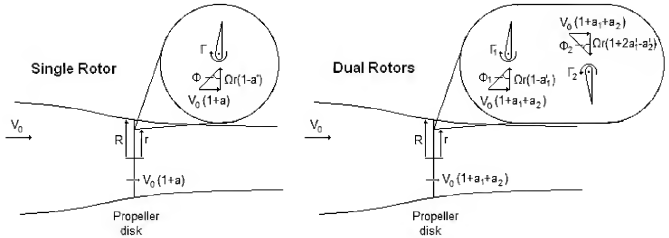


Figure A.2: Flow velocities through single and dual rotation propellers.

Total thrust and power are found by integrating  $F'$  and  $Q'$  with respect to radius. Propeller dimensions are given by the maximum radius,  $R$ , and hub-to-tip ratio,  $\xi$ . By assuming density at the propeller disk is constant, but not necessarily equal to its freestream value, specific thrust and power can be computed with equations (A.33) and (A.34).

$$\frac{F}{\dot{m}} = \frac{\int_{\xi R}^R \frac{F'}{\rho} dr}{\int_{\xi R}^R 2\pi r V_0 (1+a) dr} \quad (A.33)$$

$$\frac{P}{\dot{m}} = \frac{\int_{\xi R}^R \frac{Q'}{\rho} dr}{\int_{\xi R}^R 2\pi r V_0 (1+a) dr} \quad (A.34)$$

It can be shown that the loading of a propeller with minimum induced losses meets the condition given by equation (A.35), where  $C$  is a constant, independent of radius.[79, 154]

$$C = r \frac{V_0 (1+a) + \epsilon \Omega r (1-a')}{\Omega r (1-a') - \epsilon V_0 (1+a)} \quad (A.35)$$

For a set of propeller design parameters ( $B$ ,  $\Omega$ ,  $\epsilon$ ), there is a value of  $C$  which

corresponds to a given specific thrust requirement. The power consumed by the propeller can also be computed, and fan polytropic efficiency is determined by combining equations (A.27) and (A.34).

**Dual Rotor** Because swirl losses can be detrimental for heavily loaded propellers, dual rotation propellers are sometimes desirable for open rotor configurations. In a dual rotation propeller, or a counter-rotating propeller, two propellers rotate in opposite directions around the same axis and are designed to reduce swirl losses. Counter-rotating configurations also benefit from the partial cancellation of reaction torques produced by the engines, reducing structural loading.[155]

The single propeller analysis is adapted for dual rotation propellers by applying Lock's assumptions about the induced velocities of counter-rotating propellers.[156] These assumptions are repeated below.

- The interference velocities at any blade element may be calculated by considering the velocity fields of the two airscrews independently and adding the effects.
- Either airscrew produces its own interference velocity field which so far as it affects the airscrew itself is exactly the same as if the other airscrew were absent and includes the usual tip loss correction.
- Added to this is the velocity field of the other airscrew. Since the two are rotating in opposite directions, the effect will be periodic and its time average value may be taken to be equal to the average value round a circle having a radius of the blade element.

Each rotor induces axial and tangential velocities, again denoted  $a_i = \frac{u_{a,i}}{V_0}$  and  $a'_i = \frac{u_{t,i}}{D_1 r}$ , where subscripts 1 and 2 refer to the front and rear rotors, respectively. This model further assumes that the rotors lie in the same plane, and the axial flow velocities through the two propellers are identical and equal to  $V_0(1 + a_1 + a_2)$ . Each rotor induces a dimensionless tangential velocity  $a'_i$  on itself and  $a'_j$  on the opposite disk. Following Theodorsen, the tangential velocity behind the disk is twice its value at the disk plane, and no tangential flow is induced ahead of the disk.[157]. Induced

tangential velocities at each disk are given by equation (A.36). Axial and tangential velocities through each rotor are shown in Figure A.2.

$$\begin{aligned} i = 1 & \quad \begin{cases} a'_i = a'_1 \\ a'_j = 0 \end{cases} \\ i = 2 & \quad \begin{cases} a'_i = a'_2 \\ a'_j = -2a'_1 \end{cases} \end{aligned} \quad (A.36)$$

Applying the above assumptions to the combined vortex, blade element, and momentum theory for single propellers, equations (A.37)-(A.40) for thrust and torque per unit radius on each rotor  $i$  are developed. Each rotor contains  $B$  blades.

$$F'_i = 4\pi r \rho V_0^2 a_i (1 + a_1 + a_2) \kappa_i - B \epsilon_i \rho \Gamma_i V_0 (1 + a_1 + a_2) \quad (A.37)$$

$$F'_i = B \rho \Gamma_i \Omega_1 r \left( \frac{\Omega_i}{\Omega_1} - a'_i - a'_j \right) - B \epsilon_i \rho \Gamma_i V_0 (1 + a_1 + a_2) \quad (A.38)$$

$$Q'_i = B \rho \Gamma_i V_0 r (1 + a_1 + a_2) + B \epsilon_i \rho \Gamma_i \Omega_1 r^2 \left( \frac{\Omega_i}{\Omega_1} - a'_i - a'_j \right) \quad (A.39)$$

$$Q'_i = 4\pi r^2 \rho V_0 \Omega_1 r (1 + a_1 + a_2) a'_i \kappa_i + B \epsilon_i \rho \Gamma_i \Omega_1 r^2 \left( \frac{\Omega_i}{\Omega_1} - a'_i - a'_j \right) \quad (A.40)$$

Momentum loss factors  $\kappa_1$  and  $\kappa_2$  are defined similarly to  $\kappa$  in the single propeller case, where  $\phi_i$  refers to the local flow angle at each rotor. Again assuming that the density at each rotor disk is constant, the total thrust and power may be found by integrating and summing thrust and torque per unit radius.

$$\frac{F}{\dot{m}} = \frac{\int_{\xi R}^R \left( \frac{F'_1 + F'_2}{\rho} \right) dr}{\int_{\xi R}^R 2\pi r V_0 (1 + a_1 + a_2) dr} \quad (A.41)$$

$$\frac{\dot{P}}{\dot{m}} = \frac{\int_{\xi R}^R \left( \frac{\Omega_1 Q'_1 + \Omega_2 Q'_2}{\rho} \right) dr}{\int_{\xi R}^R 2\pi r V_0 (1 + a_1 + a_2) dr} \quad (A.42)$$

Designing each rotor to have minimum torque for fixed thrust yields the following conditions, similar to equation (A.35).  $C_1$  and  $C_2$  are constants, independent of radius.

$$C_i = r \frac{V_0 (1 + a_1 + a_2) + \epsilon_i \Omega_1 r \left( \frac{\Omega_i}{\Omega_1} - a'_i - a'_j \right)}{\Omega_1 r \left( \frac{\Omega_i}{\Omega_1} - a'_i - a'_j \right) - \epsilon_i V_0 (1 + a_1 + a_2)} \quad (A.43)$$

In the dual rotation propeller case, an additional degree of freedom is introduced by the variable  $C_2$ . As with the single propeller case, values of  $C_1$  and  $C_2$  can be chosen to match the desired specific thrust. Physically, the additional degree of freedom represents the varying fractional thrust load carried by each rotor. In this model,  $C_1$  and  $C_2$  are selected to match the desired specific thrust and minimize input power. With  $C_1$  and  $C_2$  fixed, specific power is computed with equation (A.42), and fan polytropic efficiency with equation (A.27). The relationship between fan pressure ratio and fan polytropic efficiency for a dual rotor is shown in Figure A.3 for the parameter values listed in Table A.2.

**Rotor-Stator** Rotor-stator fan configurations are commonly used in turbofans, and like dual rotation propellers, rotor-stator configurations reduce swirl losses. A rotor-stator fan is the special case of the dual rotation propeller with  $\Omega_2 = 0$ . Assumptions and analysis for the rotor-stator configuration are identical to the dual rotor case with two exceptions. First, because the stator does not rotate, it does not consume power, and therefore does not need to be designed for minimum torque. Thus equation (A.43) for  $i = 2$  is not applied. Instead, circulation on the stator is chosen to completely remove exhaust swirl,  $a'_2 = a'_1$ . Secondly, rotor-stator configurations are generally ducted, which eliminates efficiency losses due to radial flow near the tips (gap losses are not modeled); therefore,  $\kappa_1 = \kappa_2 = 1$ . The presence of a duct or shroud is not modeled directly, noting that the duct has a very small impact on performance at cruise conditions.<sup>[158]</sup> An unducted rotor-stator fan, as described in Ref. [159], could

be modeled by computing  $\kappa_i$  with equation (A.32). Finally, there is a single value of  $C_1$  which corresponds to the desired specific thrust, and fan polytropic efficiency may be found as in the dual rotation propeller case.

**Fan Configuration Comparison** Figure A.3 shows the variation in fan polytropic and propulsive efficiencies for dual rotor and rotor-stator fan configurations. Both fan polytropic and propulsive efficiencies include viscous and swirl losses, and fan propulsive efficiency additionally includes axial momentum losses. Parameter values for this analysis are given in Table A.2. Following NASA's Advanced Turboprop Project, fans are designed to operate at Mach 0.80 and an altitude of 35,000 ft, and each fan has a hub-to-tip ratio of 0.25.

Differences between unducted and ducted fans are modeled in several ways. Single and dual rotor configurations are unducted and subject to tip losses, while the rotor-stator configuration is assumed to be ducted, with no tip losses. The maximum tip speed for unducted rotors is limited by compressibility drag and noise penalties to 240 m/sec; ducted fan tip speed is set to 300 m/sec, a moderate value for large, quiet turbofans.[84, 159, 11, 160] Additionally, different blade counts are considered for ducted and unducted fans. Eight blades per rotor is representative of typical propfan configurations and twenty blades per rotor is representative of modern turbofans. Individual section drag-to-lift ratios of rotor blades are set to 0.023 based on a United Technologies single rotation high speed propeller design.[161] Stator blades can be designed for a lower drag divergence Mach number, and hence lower drag. The stator section drag-to-lift ratio is taken to be 25% lower than that of the rotor blades based on a NACA 16 series stator design.[161, 12] Finally, because dimensionless parameters are considered, fan radius affects performance only indirectly through Reynolds number drag variation. For this analysis, each fan has a radius of one meter.

The ducted rotor-stator fan performs with the highest efficiency for most fan pressure ratios because the shroud allows for higher tip speeds and eliminates radial flow losses. Dual rotor configurations are nearly as efficient but are more mechanically complex. It is assumed in this model that unducted fans employ a variable pitch mechanism, while ducted fans do not. However, very high bypass ratio ducted fans

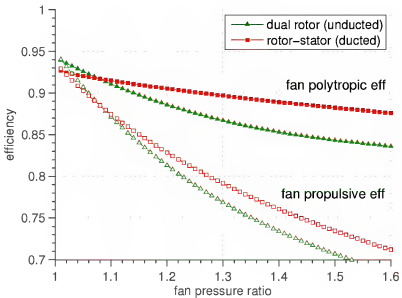


Figure A.3: Fan polytropic and propulsive efficiencies as functions of fan pressure ratio for dual rotor and rotor-stator fan configurations.

| Parameter          | Dual Rotor | Rotor-Stator |
|--------------------|------------|--------------|
| $B$                | 8          | 20           |
| $R$                | 1          | 1            |
| $\xi$              | 0.25       | 0.25         |
| $\Omega_1$ [rad/s] | 240        | 300          |
| $\Omega_2$ [rad/s] | 240        | 0            |
| $\epsilon_1$       | 0.023      | 0.023        |
| $\epsilon_2$       | 0.025      | 0.0173       |

Table A.2: Fan configuration parameters.

may require a variable geometry fan or nozzle to maintain stability during cruise,[80] and the associated penalty to mechanical complexity and weight is not modeled directly. Swirl losses cause lower polytropic and propulsive efficiencies for single rotor propfans at a given fan pressure ratio.

Results shown in Figure A.3 compare well with NASA study data. A fan propulsive efficiency of 89% is given for a dual rotor with a disc loading of 37.5 hp/ft<sup>2</sup>, which corresponds to a fan pressure ratio of approximately 1.06.[107] These analyses

also match NASA estimates for swirl and tip losses.[11] Estimates of polytropic efficiency for ducted rotor-stator fans approximately follow values for typical modern turbofans.[21, 90]

### Component Performance Assumptions

Cycle and propeller analyses are combined to estimate the overall performance of several engines with comparable levels of technology in Chapter 4. Turbofans and propfans with different bypass ratios are examined in Figures 4.6 and 4.7. Each engine is driven by the same core with fixed high pressure compressor, burner, and turbine efficiencies based on 2010 technology levels; associated efficiencies are listed in Table A.3.[21] The main engine design parameters of turbine entry temperature and overall pressure ratio (the product of fan and high pressure compressor pressure ratios) are also equal for all designs.

Low pressure spool design parameters differ for propfans and turbofans. First, because turbofans are ducted, the bypass stream flow experiences a total pressure drop through the diffuser and nozzle due to wall friction. There is no duct frictional loss for bypass flow in a propfan. Secondly, fan polytropic efficiency varies as described in the previous section. Thirdly, because propfans generally use very low pressure ratios, a gearbox is required to enable efficient fan and low pressure turbine performance. This leads to a low pressure spool efficiency penalty of approximately 1%. [162] Lastly, installation penalties for propfan engines are generally greater than those of turbofans. This performance loss depends on engine placement, but for wing mounted engines, aerodynamic interactions between the wing and engines lead to an increase in drag of approximately 3%. [84, 163]

| Parameter          | Single or Dual Rotor Propfan | Turbofan |
|--------------------|------------------------------|----------|
| $\alpha$           | varies                       | varies   |
| $\pi_{ch} * \pi_f$ | 50                           | 50       |
| $T_{T4}$ [K]       | 1700                         | 1700     |
| $\pi_{df}$         | 1.0                          | 0.995    |
| $\pi_{dc}$         | 0.995                        | 0.995    |
| $\pi_b$            | 0.96                         | 0.96     |
| $\pi_{nf}$         | 1.0                          | 0.995    |
| $\pi_{nc}$         | 0.995                        | 0.995    |
| $e_f$              | see Figure A.3               |          |
| $e_{ch}$           | 0.91                         | 0.91     |
| $e_{tl}$           | 0.915                        | 0.915    |
| $e_{th}$           | 0.905                        | 0.905    |
| $\eta_b$           | 0.995                        | 0.995    |
| $\eta_{ml}$        | 0.985                        | 0.997    |
| $\eta_{mh}$        | 0.997                        | 0.997    |
| $\eta_{inst}$      | 0.96                         | 0.99     |
| $\beta$            | 0.0                          | 0.0      |
| $\delta_1$         | 0.03                         | 0.03     |
| $\delta_2$         | 0.02                         | 0.02     |

Table A.3: Propfan and turbofan engine parameters.

# Bibliography

- [1] David S. Lee, David W. Fahey, Piers M. Forster, Peter J. Newton, Ron C.N. Wit, Ling L. Lim, Bethan Owan, and Robert Sausen. Aviation and global climate change in the 21st century. *Atmospheric Environment*, 43:3520–3537, 2009.
- [2] J.T. Wilkerson, M.Z. Jacobson, A. Malwitz, S. Balasubramanian, R. Wayson, G. Fleming, A.D. Naiman, and S.K. Lele. Analysis of emission data from global commercial aviation: 2004 and 2006. *Atmospheric Chemistry and Physics*, 10:6391–6408, 2010.
- [3] Intergovernmental Panel on Climate Change (IPCC). *Aviation and the Global Atmosphere*. Cambridge University Press, Cambridge, 1999.
- [4] Intergovernmental Panel on Climate Change (IPCC). *Climate Change 2007: The Physical Science Basis, Contribution of Working Group I to the Fourth Assessment Report of the Intergovernmental Panel on Climate Change*. Cambridge University Press, Cambridge, 2007.
- [5] Russell W. Stratton, Hsin Min Wong, and James I. Hileman. Life cycle greenhouse gas emissions from alternative jet fuels. Technical Report Project 28 Report, PARTNER, 2010.
- [6] Intergovernmental Panel on Climate Change (IPCC). *Climate Change 2007: Synthesis Report*. Cambridge University Press, Cambridge, 2007.
- [7] Nicolas Antoine. *Aircraft optimization for minimal environmental impact*. PhD thesis, Stanford University, 2004.

- [8] P.D. Norman, D.H. Lister, M. Lecht, P. Madden, K. Park, O. Penanhoat, C. Plaisance, and K. Renger. Development of the technical basis for a new emissions parameter covering the whole aircraft operation: NEPAIR, final technical report. Technical Report Contract Number G4RD-CT-2000-00182, European Community, 2003.
- [9] D. Wuebbles, M. Gupta, and M. Ko. Evaluating the impacts of aviation on climate change. *Eos, Transactions, American Geophysical Union*, 88(14), 2007.
- [10] David L. Daggett, Stephen T. Brown, and Ron T. Kawai. Ultra-efficient engine diameter study. Technical Report CR 2003-212309, National Aeronautics and Space Administration, 2003.
- [11] Daniel C. Mikkelsen, Bernard J. Blaha, Glenn A. Mitchell, and Joseph E. Wikete. Design and performance of energy efficient propellers for Mach 0.8 cruise. Technical Report TM 73612, National Aeronautics and Space Administration, Lewis Research Center, 1977.
- [12] Carl Rohrbach. A report on the aerodynamic design and wind tunnel test of a propfan model. *AIAA/SAE 12th Propulsion Conference*, (AIAA 76-667), 1976.
- [13] Mark D. Guynn, Jeffrey J. Berton, Kenneth L. Fisher, William J. Haller, Michael T. Tong, and Douglas R. Thurman. Engine concept study for an advanced single-aisle transport. Technical Report TM 215784, National Aeronautics and Space Administration, 2009.
- [14] Marcus O. Kohler, Gaby Radel, Olivier Dessens, Keith P. Shine, Helen L. Rogers, Oliver Wild, and John A. Pyle. Impact of perturbations to nitrogen oxide emissions from global aviation. *Journal of Geophysical Research*, 113, 2008.
- [15] Gaby Radel and Keith P. Shine. Radiative forcing by persistent contrails and its dependence on cruise altitudes. *Journal of Geophysical Research*, 113, 2008.

- [16] Klaus Hasselmann, Robert Sausen, Ernst Maier-Reimer, and Reinhard Voss. On the cold start problem in transient simulations with coupled atmosphere-ocean models. *Climate Dynamics*, 9:53–61, 1993.
- [17] Fortunat Joos, I. Colin Prentice, Stephen Sitch, Robert Meyer, Georg Hooss, Gian-Kasper Plattner, Stefan Gerber, and Klaus Hasselmann. Global warming feedbacks on terrestrial carbon uptake under the Intergovernmental Panel on Climate Change (IPCC) emission scenarios. *Global Biogeochemical Cycles*, 15(4):891–907, 2001.
- [18] Keith P. Shine, Jan S. Fuglestvedt, Kinfe Hailemariam, and Nicola Stuber. Alternatives to the global warming potential for comparing climate impacts of emissions of greenhouse gases. *Climatic Change*, 68(4):281–302, 2005.
- [19] O. Boucher and M.S. Reddy. Climate trade-off between black carbon and carbon dioxide emissions. *Energy Policy*, 36:193–200, 2008.
- [20] Eric Allison, Ilan Kroo, Peter Sturdza, Yoshifumi Suzuki, and Herve Martins-Rivas. Aircraft conceptual design with natural laminar flow. In *27th International Congress of the Aeronautical Sciences*, 2010.
- [21] Jack D. Mattingly, William H. Heiser, and David T. Pratt. *Aircraft Engine Design, Second Edition*. American Institute of Aeronautics and Astronautics Education Series, Reston, Virginia, 2002.
- [22] D.S. Lee, G. Pitari, V. Grewe, K. Gierens, J.E. Penner, A. Petzold, M.J. Prather, U. Schumann, A. Bais, T. Bernsten, D. Iachetti, L.L. Lim, and R. Sausen. Transport impacts on atmosphere and climate: Aviation. *Atmospheric Environment*, 44:4678–4734, December 2010.
- [23] International Civil Aviation Organization (ICAO). ICAO Environment Branch. 2010. url: <http://www.icao.int/icao/en/env2010/Index.html>.
- [24] J.E. Green. The potential for reducing the impact of aviation on climate. *Technology Analysis and Strategic Management*, 21(1):39–59, January 2009.

- [25] Alexander Koch, Bjorn Nagel, Volker Gollnick, Katrin Dahlmann, Volker Grewe, Bernd Karchner, and Ulrich Schumann. Integrated analysis and design environment for a climate compatible air transport system. In *9th AIAA Aviation Technology, Integration, and Operations Conference (ATIO)*. American Institute of Aeronautics and Astronautics, September 2009.
- [26] Stephan Lehner and William Crossley. Combinatorial optimization to include greener technologies in a short-to-medium range commercial aircraft. In *26th Congress of International Council of the Aeronautical Sciences (ICAS)*. American Institute of Aeronautics and Astronautics, September 2008.
- [27] G.P. Brasseur, R.A. Cox, D. Hauglustaine, I. Isaksen, J. Lelieveld, D.H. Lister, R. Sausen, U. Schumann, A. Wahner, and P. Wiesen. European scientific assessment of the atmospheric effects of aircraft emissions. *Atmospheric Environment*, 32(13):2329–2418, 1998.
- [28] Intergovernmental Panel on Climate Change (IPCC). *Expert Meeting on the Science of Alternative Metrics*. Cambridge University Press, Cambridge, 2009.
- [29] Robert Sausen, Ivar Isaksen, Volker Grewe, Didier Hauglustaine, David S. Lee, Gunnar Myhre, Marcus O. Kohler, Giovanni Pitari, Ulrich Shumann, Frode Stordal, and Christos Zerefos. Aviation radiative forcing in 2000: An update on IPCC (1999). *Meteorologische Zeitschrift*, 14(4):555–561, 2005.
- [30] Arthur H. Lefebvre. *Gas Turbine Combustion*. Taylor and Francis, Philadelphia, 1999.
- [31] Mark Z. Jacobson. Global direct radiative forcing due to multicomponent anthropogenic and natural aerosols. *Journal of Geophysical Research*, 106(D2):1551–1568, 2001.
- [32] J.S. Fuglestvedt, K.P. Shine, T. Bernsten, J. Cook, D.S. Lee, A. Stenke, R.B. Skeie, G.J.M. Velders, and I.A. Waitz. Transport impacts on atmosphere and climate: Metrics. *Atmospheric Environment*, 44:4648–4677, 2010.

- [33] A. Doppelheuer and M. Lecht. Influence of engine performance on emission characteristics. In *RTO AVT Symposium on Gas Turbine Engine Combustion, Emissions, and Alternative Fuels*, 1998.
- [34] M.Z. Jacobson, J.T. Wilkerson, A.D. Naiman, and S.K. Lele. The effects of aircraft on climate and pollution. Part II: Short-term impacts of exhaust from all commercial aircraft worldwide treated at the subgrid scale. *Journal of Geophysical Research - Atmospheres*, in review, 2010.
- [35] Nicola Stuber, Piers Forster, Gaby Radel, and Keith Shine. The importance of the diurnal an annual cycle of air traffic for contrail radiative forcing. *Nature*, 441:864–867, 2006.
- [36] Ulrich Schumann. Formation, properties and climatic effects of contrails. *C. R. Physique*, 6:549–565, 2005.
- [37] International Civil Aviation Organization (ICAO). ICAO engine emissions data bank. April 2008.
- [38] John B. Heywood and Thomas Mikus. Parameters controlling nitric oxide emissions from gas turbine combustors. In *41st Meeting on Atmospheric Pollution by Aircraft Engines, London, UK*, 1973.
- [39] Douglas L. Allaire. A physics-based emissions model for aircraft gas turbine combustors. Master's thesis, Massachusetts Institute of Technology, 2006.
- [40] A.H. Lefebvre. Fuel effects on gas turbine combustion - liner temperature, pattern factor and pollutant emissions. In *AIAA/SAE/ASME 20th Joint Propulsion Conference, Cincinnati, Ohio*, number 84-1491, 1984.
- [41] F. Deidewig, A. Doppelheuer, and M. Lecht. Methods to assess aircraft engine emissions in flight. *Proceedings of the 20th International Council of Aeronautical Sciences Congress, Sorrento, Italy*, 1996.
- [42] Doug DuBois and Gerald C. Paynter. Fuel flow Method 2 for estimating aircraft emissions. In *SAE Technical Paper Series*, number 2006-01-1987, 2006.

- [43] Steven L. Baugheum, Terrance G. Tritz, Stephen C. Henderson, and David C. Pickett. Scheduled civil aircraft emissions inventories for 1992: Database development and analysis. Technical Report CR 4700, National Aeronautics and Space Administration, Langley Research Center, April 1996.
- [44] C.J. Eyers, P. Normal, J. Middel, M. Plohr, S. Michot, K. Atkinson, and R.A. Christou. AERO2k global aviation emissions inventories for 2002 and 2025. Technical report, QinetiQ, December 2004.
- [45] Jasper Faber, Dan Greenwood, David Lee, Michael Mann, Pablo Mendes de Leon, Dagmar Nelissen, Bethan Owen, Malcolm Ralph, John Tilston, Andre van Velzen, and Gerdien van de Vreede. Lower NO<sub>x</sub> at higher altitudes: Policies to reduce the climate impact of aviation NO<sub>x</sub> emissions. Technical report, CE Delft, 2008.
- [46] Jorge de Luis. *A process for the quantification of aircraft noise and emissions interdependencies*. PhD thesis, Georgia Institute of Technology, 2008.
- [47] L. Lim, D.S. Lee, R. Sausen, and M. Ponater. Quantifying the effects of aviation on radiative forcing and temperature with a climate response model. In *Proceedings of an International Conference on Transport, Atmosphere and Climate (TAC)*, pages 202–207, 2006.
- [48] Don Wuebbles, Piers Forster, Helen Rogers, and Redine Herman. Issues and uncertainties affecting metrics for aviation impacts on climate. *Bulletin of the American Meteorological Society*, April 2010.
- [49] Intergovernmental Panel on Climate Change (IPCC). *Climate Change 2007: Impacts, Adaption and Vulnerability, Contribution of Working Group II to the Fourth Assessment Report of the Intergovernmental Panel on Climate Change*. Cambridge University Press, Cambridge, 2007.
- [50] United States Government, Interagency Working Group on Social Cost of Carbon. Social cost of carbon for regulatory impact analysis. Technical report, USG Executive Order 12866, 2010.

- [51] Donald J. Wuebbles, Huiguang Yang, and Redina Herman. Climate metrics and aviation: Analysis of current understanding and uncertainties. Technical Report Theme 8, FAA Aviation Climate Change Research Initiative (ACCRI), 2009.
- [52] Piers Forster and Helen Rogers. Metrics for comparison of climate impacts from well mixed greenhouse gases and inhomogeneous forcing such as those from UT/LS ozone, contrails and contrail-cirrus. Technical Report Theme 7, FAA Aviation Climate Change Research Initiative (ACCRI), 2009.
- [53] Robert Sausen and Ulrich Schumann. Estimates of the climate response to aircraft CO<sub>2</sub> and NO<sub>x</sub> emissions scenarios. *Climatic Change*, 44:27–58, 2000.
- [54] K. Hasselmann, S. Hasselmann, R. Giering, V. Oacana, and H.V. Storch. Sensitivity study of optimal CO<sub>2</sub> emission paths using a simplified structural integrated assessment model. *Climatic Change*, 37:345–386, 1997.
- [55] Karen Marais, Stephen P. Lukachko, Mina Jun, Anuja Mahashabde, and Ian A. Waitz. Assessing the impact of aviation on climate. *Meteorologische Zeitschrift*, 2008.
- [56] V. Grewe and A. Stenke. AirClim: An efficient tool for climate evaluation of aircraft technology. *Atmospheric Chemistry and Physics*, 8:4621–4639, 2008.
- [57] Mark Z. Jacobson. Control of fossil-fuel particulate black carbon and organic matter, possibly the most effective method of slowing global warming. *Journal of Geophysical Research*, 107(D19), 2002.
- [58] William D. Nordhaus and Joseph Boyer. *Warming the world: Economic models of global warming*. MIT Press, Cambridge, Massachusetts, 2000.
- [59] Richard S.J. Tol. Estimates of the damage costs of climate change. *Environmental and Resource Economics*, 21, 2002.
- [60] Milind Kandlikar. Indices for comparing greenhouse gas emissions: Integrating science and economics. *Energy Economics*, 18, 1996.

- [61] Jan Fuglestvedt, Terje K. Bernsten, Odd Godal, Robert Sausen, Keith P. Shine, and Tora Skodvin. Metrics of climate change: Assessing radiative forcing and emissions indices. *Climatic Change*, 58:267–331, 2003.
- [62] Keith P. Shine, Terje K. Bernsten, Jan S. Fuglestvedt, Ragnhild Bieltvedt Skeie, and Nicola Stuber. Comparing the climate effect of emissions of short- and long-lived climate agents. *Philosophical Transactions of The Royal Society A*, 365:1903–1914, 2007.
- [63] Richard S.J. Tol, Terje K. Bernsten, Brian C. O'Neill, Jan S. Fuglestvedt, Keith P. Shine, Yves Balkanski, and Laszlo Makra. Metrics for aggregating the climate effect of different emissions: A unifying framework. *ESRI Working Paper No. 257*, 2008.
- [64] William D. Nordhaus. *A question of balance: Weighing the options on global warming policies*. Yale University Press, New Haven, Connecticut, 2008.
- [65] W.D. Nordhaus. Discounting in economics and climate change: An editorial comment. *Climatic Change*, 37:315–328, 1997.
- [66] James K. Hammitt, Atul K. Jain, John L. Adams, and Donald J. Wuebbles. A welfare-based index for assessing environmental effects of greenhouse-gas emissions. *Nature*, 381, 1996.
- [67] Committee on Aviation Environmental Protection (CAEP) - United States. CAEP/8 NO<sub>x</sub> stringency cost-benefit analysis demonstration using APMT-IMPACTS. Technical report, CAEP Eighth Meeting, February 2010.
- [68] Michael Ponater, Susanne Pechtl, Robert Sausen, Ulrich Schumann, and Gerhard Huttig. Potential of the cryoplane technology to reduce aircraft climate impact: A state-of-the-art assessment. *Atmospheric Environment*, 40:6928–6944, 2006.
- [69] United States Environmental Protection Agency. Guidelines for preparing economic analyses. Technical report, EPA 240-R-00-003, September 2000.

- [70] Intergovernmental Panel on Climate Change (IPCC). *Climate Change 2007: Mitigation, Contribution of Working Group III to the Fourth Assessment Report of the Intergovernmental Panel on Climate Change*. Cambridge University Press, Cambridge, 2007.
- [71] John P. Weyant. A critique of the Stern Review's mitigation cost analyses and integrated assessment. *Review of Environmental Economics and Policy*, 2(1), 2008.
- [72] David Archer. Fate of fossil fuel CO<sub>2</sub> in geologic time. *Journal of Geophysical Research*, 110, 2005.
- [73] Emily Schwartz Dallara, Ilan M. Kroo, and Ian A. Waitz. Metric for comparing lifetime average climate impact of aircraft. *AIAA Journal*, 2011. Accepted for publication.
- [74] Ilan Kroo. An interactive system for aircraft design and optimization. *AIAA Aerospace Design Conference*, 1992. AIAA 92-1190.
- [75] Ilan Kroo. AA 241 Aircraft Design: Synthesis and Analysis, August 2010. url: <http://adg.stanford.edu/aa241/>.
- [76] Air Transport Association of America. Standard method for estimating comparative direct operating costs of turbine powered transport airplanes. Technical report, Air Transport Association, 1967.
- [77] GEnx engine development and component testing in full swing for Boeing 7E7, July 2010. url: [http://www.geae.com/aboutgeae/presscenter/genx/genx\\_20040719.html](http://www.geae.com/aboutgeae/presscenter/genx/genx_20040719.html).
- [78] Trent 1000: Optimised for the Boeing 787 Dreamliner family, July 2010. url: [http://www.rolls-royce.com/Images/brochure\\_Trent1000\\_tcm92-11344.pdf](http://www.rolls-royce.com/Images/brochure_Trent1000_tcm92-11344.pdf).
- [79] H. Glauert. *Airplane Propellers*, volume IV of *Aerodynamic Theory*. Julius Springer, Berlin, 1935. Edited by W.F. Durand.

- [80] R.A. Zimbrick and J.L. Colehour. Investigation of very high bypass ratio engines for subsonic transports. *Journal of Propulsion*, 6(4), July-August 1990.
- [81] Richard S. Shevell. *Fundamentals of Flight*. Prentice Hall, Upper Saddle River, New Jersey, 1989.
- [82] Joseph A. Ziemianski and John B. Whitlow. NASA/Industry Advanced Turbo-prop Technology Program. Technical Report TM 100929, National Aeronautics and Space Administration, Lewis Research Center, 1988.
- [83] C.L. DeGeorge. Large scale advanced propfan (LAP) final report. Technical Report CR 182112, National Aeronautics and Space Administration, Lewis Research Center, 1988.
- [84] James F. Dugan, Brent A. Miller, Edwin J. Graber, and David A. Sagerser. The NASA high-speed turboprop program. Technical Report TM 81561, National Aeronautics and Space Administration, Lewis Research Center, 1980.
- [85] B.S. Gatzén and W.M. Adamson. Propfan technical progress leading to technology readiness. *International Air Transportation Conference*, (AIAA 81-810), 1981.
- [86] Roy H. Lange. A review of advanced turboprop transport aircraft. *Progress in Aerospace Sciences*, 23, 1986.
- [87] F.C. Newton, R.H. Liebeck, G.H. Mitchell, A. Mooiweer, M.M. Platte, T.L. Toogood, and R.A. Wright. Multiple application propfan study (MAPS) advanced tactical transport. Technical Report CR 175003, National Aeronautics and Space Administration, Lewis Research Center, 1989.
- [88] F.B. Metzger and C. Rohrbach. Aeroacoustic design of the propfan. *AIAA 5th Aeroacoustics Conference*, (AIAA 79-610), 1979.
- [89] Geoffrey Thomas. Rolls-Royce Pursues Open Rotor. *Air Transport World*, November 2009. url: <http://atwonline.com/ aircraftenginescomponents/article/rolls-royce-pursues-open-rotor-0309>.

- [90] Jack D. Mattingly. *Elements of Propulsion: Gas Turbines and Rockets*. American Institute of Aeronautics and Astronautics Education Series, Reston, Virginia, 2006.
- [91] J.B. Whitlow and G.K. Sievers. Fuel savings potential of the NASA Advanced Turboprop Program. Technical Report TM 83736, National Aeronautics and Space Administration, Lewis Research Center, 1984.
- [92] Ilan Kroo. Propeller-wing integration for minimum induced loss. *Journal of Aircraft*, 23(7), 1986.
- [93] D.E. Gray. Study of unconventional aircraft engines designed for low energy consumption. Technical Report CR 137927, National Aeronautics and Space Administration, Lewis Research Center, 1976.
- [94] Daniel Crichton. *Fan design and operation for ultra low noise*. PhD thesis, Cambridge University, 2007.
- [95] Hamilton Standard, Division of United Technologies Corporation. Prop-fan data support study. Technical Report CR 152141, National Aeronautics and Space Administration, Ames Research Center, 1978.
- [96] Nathan Meier. Civil turbojet/turbofan specifications, July 2010. url: <http://www.jet-engine.net/civtfspec.html>.
- [97] European Aviation Safety Agency. Type certificate data sheet: Rolls Royce Trent 1000 series, August 2007.
- [98] Guy Norris. Boeing plans plain grey natural laminar flow nacelles for 787s in bid to reduce fuel burn. *Flight International*, November 2006. url: <http://www.flightglobal.com/articles/2006/07/11/207769/picture-boeing-plans-plain-grey-natural-laminar-flow-nacelles-for-787s-in-bid-to-reduce-fuel.html>.

- [99] D. Parzych and S. Cohen and A. Shenkman. Largescale advanced propfan (LAP) performance, acoustic, and weight estimation. Technical Report CR 174782, National Aeronautics and Space Administration, 1984.
- [100] The Boeing Company. Airport noise and emissions regulations, November 2010. url: [www.boeing.com/commercial/noise/charts\\_all.html](http://www.boeing.com/commercial/noise/charts_all.html).
- [101] Chris Hughes. NASA partnerships and collaborative research on ultra high bypass cycle propulsion concepts, September 2008. NASA Fall Acoustics Technical Working Group Meeting.
- [102] W.N. Dalton. Ultra high bypass ratio low noise engine study. Technical Report CR 212523, National Aeronautics and Space Administration, 2003.
- [103] ICAO. NoisedB: Noise certification database, November 2010. url: <http://noisedb.stac.aviation-civile.gouv.fr/>.
- [104] M. Kingan and R.H. Self. Advanced open rotor noise modelling tool and comparison study technical dissemination workshop. Technical report, Omega: Aviation in a Sustainable World, 2008.
- [105] Jack Lawrence, Mike Kingan, and Rod Self. Integrated study of advanced open rotor powered aircraft. Technical Report Omega Study Number 8, Omega: Aviation in a Sustainable World, 2009.
- [106] G.E. Hoff. Experimental performance and acoustic investigation of modern, counterrotating blade concepts. Technical Report CR 185158, National Aeronautics and Space Administration, Lewis Research Center, 1990.
- [107] W.C. Strack, G. Knip, A.L. Weisbrich, J. Godston, and E. Bradley. Technology and benefits of counter rotation propellers. Technical Report TM 82983, National Aeronautics and Space Administration, 1992.
- [108] Bernard Magliozzi, Paul Brown, and David Parzych. Acoustic test and analysis of a counterrotating prop-fan model. Technical Report CR 179590, National Aeronautics and Space Administration, Lewis Research Center, 1987.

- [109] Joseph L. Anderson. A parametric determination of transport aircraft price. In *34th Annual Conference, Seattle, Washington, May 5-7*. Society of Allied Weight Engineers, Inc., May 1975.
- [110] Detroit Diesel Allison. Study of turboprop systems: Reliability and maintenance costs. Technical Report CR 135192, National Aeronautics and Space Administration, Lewis Research Center, 1978.
- [111] Stephen P. Lukachko and Ian A. Waitz. Engine aging on aircraft NO<sub>x</sub> emissions. In *International Gas Turbine and Aeroengine Congress and Exhibition*, Orlando, Florida, 1997.
- [112] Kathleen M. Tacina, Chi-Ming Lee, and Changlie Wey. NASA Glenn high pressure low NO<sub>x</sub> emissions. Technical Report TM 2008-214974, National Aeronautics and Space Administration, 2008.
- [113] C.C. Gleason and D.W. Bahr. Experimental clean combustor program. Technical Report CR 135384, National Aeronautics and Space Administration, Lewis Research Center, 1979.
- [114] Christine Fichter, Michael Ponater, Robert Sausen, and Volker Grewe. Impact of flight altitudes on aviation induced climate change. Technical report, DLR, 2010.
- [115] David S. Stevenson, Ruth M. Doherty, Michael G. Sanderson, William J. Collins, Colin E. Johnson, and Richard G. Derwent. Radiative forcing from aircraft NO<sub>x</sub> emissions: Mechanisms and seasonal dependence. *Journal of Geophysical Research*, 109, 2004.
- [116] F. Stordal, G. Myhre, E.J.G. Stordal, W.B. Rossow, D.S. Lee, D.W. Arlander, and T. Svendby. Is there a trend in cirrus cloud cover due to aircraft traffic? *Atmospheric Chemistry and Physics*, 5:2155–2162, 2005.
- [117] F. Stordal, M. Gauss, G. Myhre, E. Mancini, D.A. Hauglustaine, M.O. Kohler, T. Bernsten, E.J.G. Stordal, D. Iachetti, G. Pitari, and I.S.A. Isaksen. TRADE-OFFs in climate effects through aircraft routing: Forcing due to radiatively

active gases. *Atmospheric Chemistry and Physics Discussions*, **6**:10733–10771, 2006.

[118] Gaby Radel. Personal communication, 2009.

[119] Michael S. Eldred, Brian M. Adams, David M. Gay, Laura P. Swiler, Karen Haskell, William J. Bohnhoff, John P. Eddy, William E. Hart, and Jean-Paul Watson. *DAKOTA, A Multilevel Parallel Object-Oriented Framework for Design Optimization, Parameter Estimation, Uncertainty Quantification, and Sensitivity Analysis, Version 4.2 User's Manual*. Sandia National Laboratories, Livermore, CA, 2008.

[120] Emily Schwartz, Steven L Baughcum, and David L Daggett. Quantifying the fuel burn penalties for an operational contrail avoidance system. In *SAE Aerotech Conference, Seattle, WA*, 2009.

[121] M. Gauss, I. S. A. Isaksen, and D. S. Lee an O. A. Sovde. Impact of aircraft NO<sub>x</sub> emissions on the atmosphere – tradeoffs to reduce the impact. *Atmospheric Chemistry and Physics Discussions*, **5**:12255–12311, 2005.

[122] V. Williams, R.B. Noland, and R. Toumi. Reducing the climate change impacts of aviation by restricting cruise altitudes. *Transport Research Part D*, **7**(6):451–464, 2002.

[123] Keith P. Shine and Jolene Cook. Combining models of jet engine exhaust and climate impact to quantify the trade-offs of changes in engine design and aircraft operation. Technical Report Project JETCLIM final report – Part A, Omega, 2009.

[124] Emily Schwartz and Ilan Kroo. Aircraft design: Trading cost and climate impact. In *47th AIAA Aerospace Sciences Meeting, Orlando, Florida*, 2009.

[125] MIT global airline industry program: Airline data project, December 2008. url: <http://web.mit.edu/airlinedata/www>.

- [126] I.M. Goldsmith. A study to define the research and technology requirements for advanced turbo/propfan transport aircraft. Technical Report CR 166138, National Aeronautics and Space Administration, 1981.
- [127] Ieish Gamah and Rod Self. Advanced open rotors – balancing noise costs against reduced carbon emissions for future aircraft. Technical report, Omega: Aviation in a Sustainable World, 2009.
- [128] David L. Daggett, Robert C. Hendricks, Rainer Walther, and Edwin Corporan. Alternate fuels for use in commercial aviation. Technical Report TM 2008-214833, National Aeronautics and Space Administration, 2008.
- [129] Air Transport Action Group. Beginner's guide to aviation biofuels, May 2009.
- [130] International Energy Agency. Energy technology perspectives 2010: Scenarios and strategies to 2050. Technical report, IEA, 2010.
- [131] Greener by Design. Air Travel – Greener by Design, Annual Report 2009-2010. Technical report, Royal Aeronautical Society, 2010.
- [132] Committee on Climate Change. Meeting the UK aviation target - options for reducing emissions to 2050. Technical report, CCC, 2009. url: [www.theccc.org.uk](http://www.theccc.org.uk).
- [133] Maria Vera-Morales and Andreas Schafer. Fuel-cycle assessment of alternative aviation fuels. Technical Report Tranche 1 Study Ω1/010, Omega, 2009.
- [134] International Energy Agency. World energy outlook 2010. Technical report, IEA, 2010.
- [135] Ausillio Bauen, Jo Howes, Luca Bertuccioli, and Claire Chudziak. Biofuels in aviation. Technical report, E4tech, August 2009. url: [www.e4tech.com](http://www.e4tech.com).
- [136] James I. Hileman, David S. Ortiz, James T. Bartis, Hsin Min Wong, Pearl E. Donohoo, Malcolm A. Weiss, and Ian A. Waitz. Near-term feasibility of alternative jet fuels. Technical report, PARTNER, 2009.

- [137] Mark Z. Jacobson. Effects of ethanol (E85) versus gasoline vehicles on cancer and mortality in the United States. *Environmental Science and Technology*, 41:4150–4157, 2007.
- [138] Hukam C. Mongia. TAPS - a 4th generation propulsion combustor technology for low emissions. AIAA/ICAS International Air and Space Symposium and Exposition: The Next 100 Years, 14-17 July 2003, Dayton, Ohio, 2003.
- [139] Hukam C. Mongia. On continuous NO<sub>x</sub> reduction of aero-propulsion engines. 48th AIAA Aerospace Sciences Meeting, 4-7 January 2010, Orlando, Florida, 2010.
- [140] Robert Tacina and Changlie Wey. A low NO<sub>x</sub> lean-direct injection, multipoint integrated module combustor concept for advanced aircraft gas turbines. Technical Report TM 2002-211347, National Aeronautics and Space Administration, 2002.
- [141] Ric Parker. From blue skies to green skies: Engine technology to reduce the climate-change impacts of aviation. *Technology Analysis and Strategic Management*, 21(1):61–78, 2009.
- [142] ICAO Environmental Branch. ICAO Environmental Report 2010. 2010.
- [143] ACARE. ACARE 2020: The challenge of the environment. Technical report, Advisory Council for Aeronautics Research in Europe (ACARE), 2001.
- [144] Klaus Gierens, Ling Lim, and Kostas Eleftheratos. A review of various strategies for contrail avoidance. *The Open Atmospheric Science Journal*, 2:1–7, 2008.
- [145] F. Noppel and R. Singh. Overview on contrail and cirrus cloud avoidance technology. *Journal of Aircraft*, 44(5), 2007.
- [146] Christine Fichter, Susanne Marquart, Robert Sausen, and David S. Lee. The impact of cruise altitude on contrails and related radiative forcing. *Meteorologische Zeitschrift*, 14(4):563–572, 2005.

- [147] Hermann Mannstein, Peter Spichtinger, and Klaus Gierens. A note on how to avoid contrail cirrus. *Transportation Research Part D*, 10, 2005.
- [148] Peter Spichtinger, Klaus Gierens, Ulrich Leiterer, and Horst Dier. Ice supersaturation in the tropopause region over Lindenberg, Germany. *Meteorologische Zeitschrift*, 12(3):143–156, 2003.
- [149] G. Radel and K.P. Shine. Evaluation of the use of radiosonde humidity data to predict the occurrence of persistent contrails. *Quarterly Journal of the Royal Meteorological Society*, 133:1413–1423, 2007.
- [150] S.L. Baughcum, M.Y. Danilin, L.M. Miloshevich, and A.J. Heymsfield. Properties of ice-supersaturated layers based on radiosonde data analysis. In *TAC-2 Proceedings, June 22nd to 25th, 2009, Aachen and Maastricht*. Proceedings of the International Conference on Transport, Atmosphere, and Climate (TAC-2), 2009.
- [151] Air Transport Association of America. ATA quarterly cost index: U.S. passenger airlines, November 2010. url: <http://www.airlines.org/Economics/Data-Analysis/Pages/QuarterlyCostIndex.aspx>.
- [152] Brian J. Canwell. AA 283 Aircraft and Rocket Propulsion: Course Notes, January 2007. url: [http://www.stanford.edu/~cantwell/AA283\\_Course\\_Material/AA283\\_Course\\_Notes](http://www.stanford.edu/~cantwell/AA283_Course_Material/AA283_Course_Notes).
- [153] Charles N. Adkins and Robert H. Liebeck. Design of optimum propellers. *Journal of Propulsion and Power*, 10(5), Sept-Oct 1994.
- [154] Ilan Kroo. AA 200B Applied Aerodynamics II: Course Notes, July 2010. url: <http://adg.stanford.edu/aa200b/aa200b.html>.
- [155] Harry S. Wainauski and Carol M. Vaczy. Aerodynamic performance of a counter rotating propfan. *AIAA/ASME/SAE/ASEE 22nd Joint Propulsion Conference*, (AIAA 86-1550), 1986.

- [156] C.N.H. Lock. Interference velocity for a close pair of contra-rotating airscrews. Technical Report 2084, Aeronautical Research Council Reports and Memoranda, 1941.
- [157] Theodore Theodorsen. *Theory of Propellers*. McGraw-Hill Book Company, New York, 1948.
- [158] Donald M. Black, Harry S. Wainauski, and Carl Rohrbach. Shrouded propellers - a comprehensive performance study. *AIAA 5th Annual Meeting and Technical Display*, (AIAA 68-994), 1968.
- [159] John F. Groenweg and Lawrence J. Bober. NASA advanced propeller research. Technical report, National Aeronautics and Space Administration, 1988.
- [160] James H. Dittmar and Richard P. Woodward. An evaluation of some alternative approaches for reducing fan tone noise. Technical Report TM 105356, National Aeronautics and Space Administration, Lewis Research Center, 1992.
- [161] Harry S. Wainauski and Carol M. Vaczy. Airfoiled blade, July 1988. United States Patent Number 4,834,617.
- [162] C. Rohrbach and F. B. Metzger. The propfan - a new look in propellers. *AIAA/SAE 11th Propulsion Conference*, (AIAA 75-1208), 1975.
- [163] David F. Vernon, Harry S. Page, and Robert Welge. Propfan experimental data analysis. Technical Report CR 166582, National Aeronautics and Space Administration, Ames Research Center, 1984.